

ABSTRACT

Title of dissertation: H_α & NEUTRAL DENSITY SCALING IN
THE MARYLAND CENTRIFUGAL EXPERI-
MENT

M. Ryan Clary, Doctor of Philosophy, 2009

Dissertation directed by: Professor Richard Ellis
Department of Physics

The Maryland Centrifugal eXperiment (MCX) is a hydrogen plasma confinement experiment with a rotating mirror magnetic configuration. This experiment was designed to test the concepts of centrifugal confinement and velocity shear stabilization which may allow scaleability to a fusion reactor. These two concepts, however, rely on supersonic plasma fluid velocities, which, apart from possible plasma instabilities, could be greatly reduced by fluid drag with neutral hydrogen, leading to decreased confinement. Resonant charge exchange between a hydrogen ion and a hydrogen atom is believed to be the dominant drag mechanism on the rotating plasma. Neutral hydrogen emission lines (particularly the Balmer- α line, H_α) are therefore of primary interest in diagnosing how neutral hydrogen affects plasma confinement. For this purpose, a multi-chord H_α emission detector (multi-chord HED) was designed and constructed by the author in order to measure emissivity profiles. These profiles, together with an atomic collisional-radiative model, provide estimates of neutral hydrogen density and local charge-exchange times. Varied experimental parameters were applied to MCX discharges and the resulting variations in neutral density are compared to theoretical scaling laws. The charge-exchange times are compared to the measured momentum confinement time. We find that the inner and outer-most flux surfaces are not distinctly identified by the emissivity profile and the emissivity is

dominant at the vacuum chamber wall. We also find that, while the overall emissivity profile does not match theoretical prediction, neutral density scaling is approximately described by the models. In addition, charge-exchange times are found to be much smaller than the momentum confinement time as well as to scale differently than the momentum confinement time.

This dissertation includes a detailed description of the multi-chord HED system and its calibration, both spectrally and absolutely. We also present models based on neutral and plasma interaction which provide the scaling laws used to compare to experimental results.

H α & NEUTRAL DENSITY SCALING IN THE MARYLAND
CENTRIFUGAL EXPERIMENT

by

M. Ryan Clary

Dissertation submitted to the Faculty of the Graduate School of the
University of Maryland, College Park in partial fulfillment
of the requirements for the degree of
Doctor of Philosophy
2009

Advisory Committee:
Professor Richard Ellis, Chair/Advisor
Professor Adil Hassam, Co-Advisor
Professor Christopher Davis
Professor Alan DeSilva
Professor William Dorland
Professor Wendell Hill

© Copyright by
M. Ryan Clary
2009

DEDICATION

To my wife... without her I could not accomplish anything.

ACKNOWLEDGMENTS

I would like to thank my advisors, Rick Ellis and Adil Hassam, for putting up with me for the last five years and, of course, for their guidance and mentorship. I would also like to thank members of the MCX team, past and present, for their support and contributions to my experience. I thank Robert Lunsford for showing me the ropes early and helping me get up to speed with MCX operations. I am grateful to Ray Elton for his many instructional conversations regarding spectroscopy and radiative-collisional concepts. I thank Catalin Teodorescu for his unfailing operation of the interferometer on my behalf. Lastly, I thank Ilker Uzun-Kaymak for informing me that *everyone*, at some point, thinks their dissertation sucks.

TABLE OF CONTENTS

List of Tables	vi
List of Figures	vii
1 Introduction	1
1.1 Previous Studies of Neutral Hydrogen on MCX	2
1.2 Outline of this Dissertation	4
2 Neutral Modeling at MCX Mid-Plane	6
2.1 Basic MCX Theory	6
2.2 Neutral Processes	11
2.3 Neutral Density & H_α	14
2.4 MCX Neutral Models	17
2.4.1 Numerical Modified Goldston-Rutherford Model	18
2.4.2 Numerical Modified Goldston-Rutherford Centrifugal Model	20
2.4.3 H_α Emissivity Profiles	22
2.5 Conclusions	23
3 The H_α Emission Detector	25
3.1 H_α Emission Detector Characteristics	25
3.2 Vacuum Chamber Reflections	28
3.3 Viewport Transmission	33
3.4 H_α Emission Detector Calibration	36
3.4.1 H_α Emission Detector Spectral Calibration	36
3.4.2 H_α Emission Detector Absolute Calibration	39
3.5 Conclusions	44
4 Experimental Results & Discussion	45
4.1 Experiment Description	45
4.2 Radial Profiles in MCX Discharges	51
4.3 MCX Discharge Phenomenology	57
4.4 Neutral Density & Charge-Exchange Time Scaling	69
4.5 H_α Emissivity Temporal Analysis	75
4.6 Conclusions	78
5 Future Developments	81
5.1 Neutral Modeling Improvement	81
5.2 H_α Emission Detector Improvement	82
5.3 Future Experiments	84
A Neutral Model Derivations	86
B Optical Geometry of the HED View Chord	92

C	Abel Transform	101
C.1	The Continuous & Discrete Abel Transform	102
C.2	Inversion Validation & Error Estimates	106
D	Nominal MCX Parameters	112
	Bibliography	114

LIST OF TABLES

3.1	Typical HED Gains & Signal Bandwidths	29
3.2	HED Calibration Factors	43
4.1	HED Chord Locations.	49
4.2	Applied Experimental Conditions.	51
D.1	Nominal MCX Discharge Parameters	113
D.2	Nominal MCX Discharge Time Scales	113

LIST OF FIGURES

1.1	Centrifugal Confinement Concept of MCX	2
2.1	Neutral & Plasma Diffusion Schematic	13
2.2	Rate Coefficients	13
2.3	H $_{\alpha}$ Emissivity per Neutral	16
2.4	Sensitivity of Neutral Density Estimates	17
2.5	Plasma & Neutral Density Profiles without Centrifugal Effects	19
2.6	Plasma & Neutral Density Profiles with Centrifugal Effects	21
2.7	Nominal H $_{\alpha}$ Emissivity Profiles	23
3.1	H $_{\alpha}$ Emission Detector Schematic	26
3.2	Reflectance Bench Test Results	30
3.3	In-situ Flock Paper Results	32
3.4	In-situ Flock Paper Photographs	33
3.5	Viewport Transmittance Results	35
3.6	Interference Filter Spectral Transmittance	38
4.1	MCX Circuit Diagram	46
4.2	Typical MCX Discharge	47
4.3	MCX Cross-section with HED Locations	49
4.4	H $_{\alpha}$ Profile for Standard Conditions	54
4.5	HED & Spectrometer Profile Comparison	55
4.6	Neutral Density & τ_{cx} Radial Profiles	56
4.7	Neutral Density & Temperature Profiles	57
4.8	Relative Emissivity Profiles for Experiment Parameters	58
4.9	Results of Magnetic Field Variation	60
4.10	Results of Fill Pressure Variation	63
4.11	Results of Mirror Ratio Variation	65
4.12	Results of Capacitor Bank Voltage Variation	67
4.13	Neutral Density Adjusted for Varying T_e	69
4.14	Neutral Density Scaling	71
4.15	Charge-exchange Time Scaling	73
4.16	H $_{\alpha}$ Emissivity Profile vs. Time	76
B.1	Collection Optics Viewing Geometry	94
B.2	Solid-angle & Lens Intersection	95
B.3	Normalized Solid-angles Along the Optic Axis	97
B.4	Deviation of Effective Solid-angle along Optic Axis	98
B.5	Measured Effective Solid-angle	99
C.1	Abel Projection Illustration (Continuous)	102
C.2	Abel Projection Illustration (Discrete)	104
C.3	Abel Inversion Error from Random Noise	109
C.4	Abel Inversion Error from Systematic Mis-measurement	110

Chapter 1

Introduction

The Maryland Centrifugal eXperiment (MCX) is a plasma confinement experiment with mirror magnetic geometry. The central aim of this experiment is to explore the use of centrifugal forces and shear flows to enhance plasma confinement for fusion [1]. Enhanced confinement through centrifugal forces is expected to be achieved by rotating the plasma in a magnetic field of mirror geometry. This concept is illustrated in Fig. 1.1. As the plasma rotates in the azimuthal direction it experiences a centrifugal force in the rotating frame and the magnetic field supplies a force perpendicular to the field which constrains the plasma to the flux surface (frozen in MHD theory). These two forces result in a net force toward lower magnetic field intensity (mid-plane) and away from high field intensity (mirror throats). The azimuthal rotation is a drift motion produced by a radial electric field and the axial magnetic field ($u_\phi = \mathbf{E} \times \mathbf{B}/B^2$), and is maintained against drag forces by a radial current ($\mathbf{F} = \mathbf{j} \times \mathbf{B}$). This is described in more detail in Sec. 2.1. Enhanced confinement is also expected due to the presence of shear in the azimuthal rotation of the plasma [2–4]. Here, the radial shear is expected to suppress interchange instabilities, thus improving plasma confinement.

In this chapter, we begin with a description of the importance of characterizing neutral hydrogen behavior in this experiment, thus motivating the present research. Next, we give a brief summary of previous research done on this experiment with regard to neutral behavior. Finally, we give a brief outline of the remainder of this dissertation.

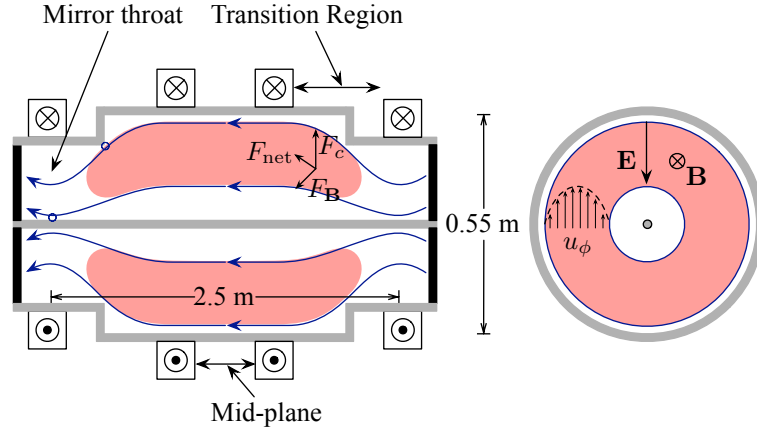


Figure 1.1: As plasma rotates in the $\hat{\phi}$ direction it experiences a centrifugal force which, when constrained to a magnetic flux surface, drives it toward the mid-plane.

1.1 Previous Studies of Neutral Hydrogen on MCX

Any plasma confinement device is necessarily finite in spatial extent and therefore contains a boundary between the confined plasma and the outside world. The properties of this boundary depends heavily on the type of device and, in particular, the magnetic configuration used for confinement. Nevertheless, one aspect all devices share is the intrinsic temperature difference and resulting difference in states of matter, i.e. hot ($> 10^5$ °K) plasma on one side of the boundary and room temperature solid or gaseous matter on the other. The physical distance between these two extremes and its effect on the confinement properties of the plasma is central to fusion research. It has been said that many problems in physics are determined by their boundary conditions [5]. Due to this large change in temperatures, plasma boundaries inevitably contain cold neutrals, the non-ionized state of the plasma species. These neutral particles at the plasma edge can have profound impacts on the general confinement properties of the plasma. For example, studies performed on the Alcator C-Mod tokamak suggest that edge neutral densities as low as 0.1% of the plasma core density are significant enough to affect plasma flows and may be important in H-mode (high confinement mode) physics [6]. Thus, much of fusion research is de-

voted to the study of plasma boundaries and the effect that neutral particles have on plasma temperature, density, and stability.

Neutral studies on MCX have been done previous to this work. Messer [7, 8] has made rough estimates of ionization fraction by assuming that the measured confinement time is equivalent to the charge exchange time, $\tau_M = \tau_{cx} = 1/N\alpha_{cx}$, and assuming a value for the charge exchange rate coefficient, α_{cx} . This estimate predicted neutral densities of less than 1% ($\lesssim 10^{12} \text{ cm}^{-3}$). This is a reasonable estimate, consistent with pre-fill gas pressures and measurements of electron densities made at the that time. Ghosh has performed extensive spectroscopic measurements on MCX, extracting estimates for electron density, electron temperature, ion temperature, and neutral density [9–11]. His estimate of neutral density is about 5% (95% ionization fraction) [10], which may be inconsistent with Messer’s estimates. However, Ghosh’s estimate was obtained via an absorption model for the hydrogen Lyman- α emission line and may be more heavily weighted by the edge regions of the plasma where the neutral density (and Ly α absorption) is larger.

The problem with global estimates of neutral density is that the density may change several orders of magnitude from the edge to the core, thus accurate determination of an effective charge-exchange time requires absolute measurement of the neutral density profile. Both the plasma core, where ion-neutral collisions are expected to be less frequent, and the plasma edge, where these collisions are expected to be more frequent, will contribute to an effective ion-neutral collision rate. However, the edge region may be most important in determining the effect of neutrals on general plasma confinement, as evidenced by theoretical studies on plasma-neutral interaction [12–14] and experimental efforts to measure neutral density at plasma boundaries [15–17]. Thus it is necessary to measure an absolute neutral density profile in order to characterize its effect on plasma confinement.

In order to further our understanding of the effects of neutral particles on MCX discharges a multi-chord H_α emission detector (multi-chord HED) has been developed and implemented by the author. The use of absolute emission from a particular atomic transition in an atom or ion to determine the density of the species is not new and different instruments have been employed on various types of fusion experiments in order to measure absolute transition line emission [15–22]. Each instrument, though, has common characteristics: light collection via optical lens(es); light detection via photo-diode, charge coupled device, or photomultiplier tube; and absolute calibration via calibrated emission source (usually accompanied by an integrating sphere for the purpose of homogenizing the output in solid-angle). The details of these characteristics depend heavily on the emission line of interest and the logistics surrounding optical access to the plasma region of interest. The HED developed for MCX is unique in that it is comprised entirely of standard, off-the-shelf optical components, rendering it inexpensive (\sim \\$1 k/channel), extensible, and highly versatile.

The critical ionization velocity (CIV) [23] effect is a significant phenomenon in plasma physics related to plasma-neutral interaction. Investigations of this effect in MCX discharges was initiated by Lunsford [24] and continued by Teodorescu [25]. These studies indicate that the plasma-neutral interaction resulting in observed CIV in MCX discharges may occur in the vicinity of the end insulators. The multi-chord HED system may be useful in studying CIV effects in MCX discharges in the future. However, under the current experiment configuration, optical access to the insulator region is inadequate for the HED system to be of much use, thus CIV effects are not addressed in this work.

1.2 Outline of this Dissertation

This dissertation will proceed as follows. Chapter 2 briefly describes the basic MHD theory behind MCX and the most current theoretical treatments of neutral particles

applied to MCX. Here we will show that plasma rotation is driven by applied current against loss of angular momentum through energy, momentum, and particle losses. We also show two 1D plasma-neutral fluid models, one without centrifugal considerations and one with centrifugal considerations. These assert scaling laws for neutral density profiles. Also described here will be the atomic cross-sections for processes of interest, in particular the emission of hydrogen Balmer- α radiation.

Chapter 3 gives an extensive description of the primary diagnostic for this work, the H_α emission detector multi-chord array. This includes a description of the components of the device itself, considerations for vacuum chamber reflections, and the absolute calibration procedure.

Chapter 4 provides the primary results of measurements made by the HED multi-chord array. This chapter contains four sections in which data is presented and interpreted: radial H_α emissivity profiles, general discharge and H_α emissivity phenomenological behavior, neutral density and charge-exchange time scaling, and temporal behavior of H_α emissivity.

Chapter 5 recommends future research endeavors, both theoretical and experimental, regarding H_α and neutral particles in MCX discharges.

Appendix A provides detailed derivations of both 1D neutral models discussed in Chapter 2. A detailed proof that the effective solid-angle of an HED viewing chord is uniform along the line of sight is given in Appendix B, supplementing Chapter 3. Appendix C details the Abel transform and its inversion technique as it is applied in this work.

Chapter 2

Neutral Modeling at MCX Mid-Plane

In this chapter we endeavor to describe the basic confinement paradigm of MCX discharges, namely centrifugal confinement, and the effect that a neutral fluid may have on this confinement. We begin with a set of MHD equations which include a neutral fluid and proceed to show that large rotation velocity is central to the centrifugal confinement concept. We also show that the presence of a neutral fluid represents a drag on the plasma rotation, which motivates the study of neutral particles in MCX discharges. Plasma-neutral collision processes are then discussed followed by a description of the recent plasma-neutral fluid models applied to MCX discharges. Finally, we discuss the relationship between neutral hydrogen and the hydrogen Balmer- α emission line (H_α line).

2.1 Basic MCX Theory

In this section we will derive the basic expression describing centrifugal confinement and indicate how the presence of a neutral fluid may impede the required plasma rotation. Let us begin with the following standard continuity and momentum equations for a single-fluid (MHD) plasma with a neutral fluid.

$$\frac{\partial n}{\partial t} + \nabla \cdot (n\mathbf{u}) = -n^2\alpha_r + nN\alpha_i \quad (2.1)$$

$$m\frac{\partial n\mathbf{u}}{\partial t} + m\nabla \cdot (n\mathbf{u}\mathbf{u}) + \nabla p = \frac{1}{c}\mathbf{j} \times \mathbf{B} - mn^2\alpha_r\mathbf{u} + mnN\alpha_i\mathbf{U} - mnN\alpha_{cx}(\mathbf{u} - \mathbf{U}) \quad (2.2)$$

$$\frac{\partial N}{\partial t} + \nabla \cdot (N\mathbf{U}) = n^2\alpha_r - nN\alpha_i \quad (2.3)$$

$$m\frac{\partial N\mathbf{U}}{\partial t} + m\nabla \cdot (N\mathbf{U}\mathbf{U}) + \nabla P = mn^2\alpha_r\mathbf{u} - mnN\alpha_i\mathbf{U} + mnN\alpha_{cx}(\mathbf{u} - \mathbf{U}) . \quad (2.4)$$

Here, α_{cx} is the charge-exchange rate coefficient, α_i is the ionization rate coefficient, and α_r is the recombination rate coefficient. Uppercase variables denote neutral fluid variables while lowercase denote plasma variables, except for m , which is the mass for both a hydrogen atom as well as a hydrogen ion. We have ignored viscosity, considering it of lower order.

Under equilibrium conditions, with the use of Eq. (2.1), Eq. (2.2) becomes

$$nm\mathbf{u} \cdot \nabla\mathbf{u} + \nabla p = \frac{1}{c}\mathbf{j} \times \mathbf{B} - mnN(\alpha_{cx} + \alpha_i)(\mathbf{u} - \mathbf{U}) . \quad (2.5)$$

We can obtain the basic expected behavior of MCX discharges from analyzing Eq. (2.5). We use a combination of magnetic coordinates (ψ, ϕ, b) and cylindrical coordinates (r, ϕ, z) . Here ψ is the flux coordinate, which corresponds to the r coordinate at the mid-plane ($z = 0$), ϕ is the usual angular coordinate about the z axis, and b is the coordinate along the magnetic field, which corresponds to z at the mid-plane. First, let us enumerate some preliminary assumptions.

1. The angular frequency of plasma rotation, $\Omega = u_\phi/r$, is assumed to be only a function of ψ , the magnetic flux coordinate. This means that flux surfaces rotate as rigid rotors and is consistent with MHD frozen-in theory.

2. The plasma is azimuthally symmetric. This means that the magnitudes of all variables involved are not functions of ϕ .
3. $u_\phi \gg u_{\psi,b}$. This is a good approximation as u_ϕ is typically twice the ion sound speed and under ideal equilibrium conditions $u_{\psi,b}$ will only arise through diffusive processes.
4. We assume that the plasma is isothermal.

To analyze MCX MHD equilibrium, we will construct the two independent equations which Eq. (2.5) implies (the $\hat{\phi}$ equation is superfluous due to the symmetry). First we will examine Eq. (2.5) away from the mid-plane. Here we are primarily concerned with showing the centrifugal effects. Using the above assumptions we can directly evaluate the first term on the left-hand side of Eq. (2.5) in cylindrical coordinates as follows.

$$\begin{aligned}
nm \mathbf{u} \cdot \nabla \mathbf{u} &= nm \frac{u_\phi}{r} \partial_\phi (u_\phi \hat{\phi} + u_r \hat{\mathbf{r}} + u_z \hat{\mathbf{z}}) \\
&= nm \frac{u_\phi}{r} (-u_\phi \hat{\mathbf{r}} + u_r \hat{\phi}) \\
&\approx -nm \frac{u_\phi^2}{r} \hat{\mathbf{r}} \\
&= -nm r \Omega^2 \hat{\mathbf{r}} = -\frac{1}{2} nm \Omega^2 \nabla r^2.
\end{aligned} \tag{2.6}$$

Thus the convective term is approximately in the radial direction only (having both $\hat{\psi}$ and $\hat{\mathbf{b}}$ components). The $\hat{\phi}$ components of Eq. (2.5) then give

$$\begin{aligned}
\hat{\phi} \cdot \left(\frac{1}{c} \mathbf{j} \times \mathbf{B} - \nabla p \right) &= \hat{\phi} \cdot [mnN (\alpha_{cx} + \alpha_i) (\mathbf{u} - \mathbf{U})] \\
j_r B_z &= mcnN (\alpha_{cx} + \alpha_i) (u_\phi - U_\phi),
\end{aligned} \tag{2.7}$$

indicating that the cross-field current must balance the rotational momentum losses, i.e the applied radial current is what drives the system against the drag imposed by

neutral particles. It is worthy of note here that the primary momentum loss mechanism is believed to be charge exchange. This will be discussed further in Secs. 2.2 and 2.4. It is also worthy of note that the recombination term originally present in the momentum equation has cancelled since it also appears as a particle sink in the continuity equation.

Taking the projection of Eq. (2.5) onto $\hat{\mathbf{b}}$ gives the components along the magnetic field; recall that u_b and U_b are lower order, so that the pressure term and the convective term balance.

$$\begin{aligned}
nm \hat{\mathbf{b}} \cdot (\mathbf{u} \cdot \nabla \mathbf{u}) &= -\hat{\mathbf{b}} \cdot \nabla p \\
nm \frac{1}{2} \Omega^2 \nabla_{\parallel} r^2 &\approx \nabla_{\parallel} p \\
nm \frac{1}{2} \nabla_{\parallel} (\Omega^2 r^2) &\approx \nabla_{\parallel} p \\
nm \frac{1}{2} \nabla_{\parallel} u_{\phi}^2 &\approx \nabla_{\parallel} p.
\end{aligned} \tag{2.8}$$

Here we have used Eq. (2.6) and the fact that $\Omega = \Omega(\psi)$ is independent of b . This shows that the centrifugal force balances the pressure gradient along the magnetic field, i.e. faster rotation enhances mirror confinement. Note that the convective term has a projection along the magnetic field only at locations away from the mid-plane (i.e. $z \neq 0$), where $\hat{\mathbf{r}}$ has a non-zero projection onto $\hat{\mathbf{b}}$.

Now, using the isothermal assumption, $\nabla_b p = T \nabla_b n$, and the plasma ion sound speed, $c_s^2 = T/m$, we may write the following.

$$\begin{aligned}
nm \frac{1}{2} \nabla_b u_{\phi}^2 &= m c_s^2 \nabla_{\parallel} n \\
\frac{1}{2} \nabla_{\parallel} \left(\frac{u_{\phi}}{c_s} \right)^2 &= \frac{1}{n} \nabla_{\parallel} n \\
\frac{1}{2} \nabla_{\parallel} M_s^2 &= \nabla_{\parallel} \ln \frac{n}{A} \\
n(\psi, b) &= A e^{M_s^2/2},
\end{aligned} \tag{2.9}$$

where M_s is the sonic Mach number. By evaluating n at the mid-plane we get an expression for A . At the mid-plane, we will take the convention that $\psi \leftrightarrow r$ and $b \leftrightarrow z = 0$. Here, we require the expression for $n(\psi, b)$ to reduce to the radial density profile, $n(r, z)|_{z=0} \equiv n_0(r)$. At the mid-plane, the Mach number becomes only a function of r , or equivalently ψ , and $M_s|_{z=0} = r\Omega(r)/c_s = M_{s,0}(\psi)$. These produce the final expression for $n(\psi, b)$.

$$\begin{aligned} n(\psi, b) &= n_0(\psi) \exp [(M_s^2 - M_{s,0}^2)/2] \\ &= n_0(\psi) \exp [\Omega^2(\psi) (r^2 - r_0^2) / 2c_s^2] , \end{aligned} \quad (2.10)$$

where r and r_0 have the same flux coordinate, ψ , i.e. they are on the same field line. We see from Eq. (2.10) that the density at a location away from the mid-plane is related exponentially in r to the density on the same field-line at the mid-plane. For MCX field geometry, field lines decrease in radius further from the mid-plane as they approach the mirror throats, thus plasma density should be much smaller away from the mid-plane. By considering magnetic flux conservation we may write $\pi r_0^2 B_0 = \pi r_{\text{mir}}^2 B_{\text{mir}} \rightarrow r_0^2 / r_{\text{mir}}^2 = B_{\text{mir}} / B_0 = \mathcal{R}$, where r_0 and r_{mir} are located at the mid-plane and mirror throat, respectively, and reside on the same flux surface, and \mathcal{R} is the mirror ratio. Then,

$$n(\psi, b_{\text{mir}}) = n_0(\psi) \exp [-M_{s,0}^2(\psi) (1 - 1/\mathcal{R}) / 2] , \quad (2.11)$$

indicating enhanced centrifugal confinement for larger mirror ratios and larger Mach numbers. This is the canonical result which motivates the centrifugal confinement scheme.

What we have endeavored to demonstrate is the basic MCX confinement paradigm and the importance of maintaining a high rotation velocity. We have shown that neutrals play a primary role as a drag on plasma rotational velocity, expressed in

Eq. (2.7), and that the effects of neutrals *along* the field should be of lower order compared to the centrifugal forces driving the plasma toward the mid-plane. We should note here, however, that this is merely a good starting point from which to analyze neutrals and may prove to be inaccurate. For example, the above theoretical approach has not attempted to address the possibility of Critical-Ionization-Velocity effects [23], nor has it addressed the increased relative effect of neutrals near the insulator or transition regions where plasma density is expected to be much smaller than at the mid-plane. These may have profound effects on the plasma rotation velocity.

2.2 Neutral Processes

Essential to studying the transport of neutrals and their effect on plasma confinement are the mechanisms for physical interaction between the neutrals and the plasma. The mechanisms by which plasma and neutral fluids interact are ionization, recombination, and charge-exchange.¹ A detailed understanding of all three processes is beyond the scope of this work, nevertheless it is appropriate to indicate some of their general characteristics as they apply to MCX discharges.

Ionization is the process by which a neutral particle loses its bound electron and becomes an ion. This can be considered an inelastic collision process in which collision energy is transferred to the bound electron of the neutral, ejecting the electron and ionizing the neutral. The collisional particle can be an existing free electron (electron-impact ionization), an existing ion (ion-impact ionization), another neutral particle, or even a photon (photo-ionization). However, due to the electron's much smaller mass and concomitant larger velocity, electron-impact ionization stands alone as the dominant process and we will only consider this type of ionization process.

¹CIV is also a plasma-neutral interaction, but the fundamental mechanism is not fully understood [23] and we do not address CIV phenomena in this work.

Recombination can occur as a two-body process (radiative-recombination) whereby a single electron becomes bound to an ion, forming a neutral particle with the electron at some excited state and then radiatively decaying to lower excited states, presumably until it reaches the ground state. Recombination can also occur even for energetic free electrons through a three-body collision process in which one electron loses a sufficient amount of energy to a second electron, allowing the first to be bound to the participating ion. Like radiative-recombination, this process can also produce a neutral in an excited state which radiatively decays. We do not consider three-body recombination in this work.

Charge-exchange is a process by which a neutral transfers its electron to a nearby ion. The original and final neutral particles can be in any excited state, however, the transfer from ground state to ground state is dominant due to a resonance effect [26]. Note that charge-exchange does not directly affect the local neutral or plasma density, as there is not a net increase or decrease of either neutrals, ions, or free electrons. However, charge-exchange can be a dominant transport mechanism since a high energy ion, presumably trapped by a magnetic field, can become a high energy neutral which is not trapped by a magnetic field, thus providing an efficient way to transport plasma energy out of the plasma.

Figure 2.1 illustrates the concept of neutral and plasma diffusion. Neutral density is expected to be high near the vessel wall since ions and electrons colliding with the wall will transfer most of their energy to the wall, allowing them to more easily recombine (effectively increasing the recombination rate). At the core of the plasma, it is expected that neutral density is very low (high ionization fraction). Where plasma and neutrals interact, ionization, recombination, and charge-exchange will transfer particles, energy, and momentum back and forth between the plasma and neutral fluids. In addition, both fluids diffuse against the gradient of their respective density.

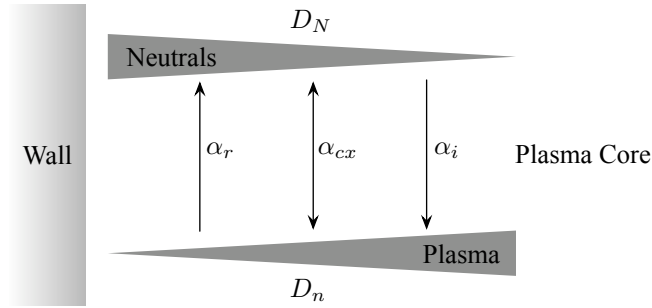


Figure 2.1: Plasma diffuses away from regions of high plasma density and toward the boundary (a wall or magnetic flux surface). Neutral gas diffuses away from high neutral density (a wall or magnetic flux surface) and into the plasma region. These fluids interact via recombination, α_r , charge-exchange, α_{cx} , and ionization, α_i . In equilibrium, these processes balance to create static plasma and neutral density profiles.

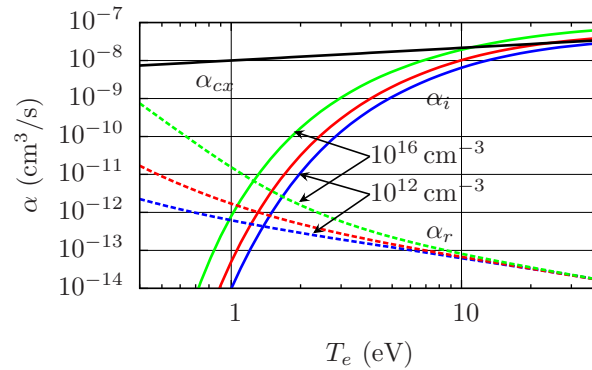


Figure 2.2: Charge-exchange, ionization, and recombination rate coefficients are shown as functions of electron temperature for different plasma densities. The charge-exchange rate coefficient is plotted versus ion temperature. Charge-exchange dominates, particularly for $T_e < 6$ eV. Recombination dominates ionization for $T_e \lesssim 1.2$ eV. Ionization and recombination data are obtained from Johnson & Hin-nov [27]; charge-exchange data is adapted from Hutchinson [26].

In Fig. 2.2 are shown ionization, recombination, and charge-exchange rate coefficients as a function of electron temperature (ion temperature for α_{cx}) and for various plasma densities. The ionization rate coefficient is a strong function of electron temperature and dominates recombination for $T_e \gtrsim 1.2$ eV. In contrast, the charge-exchange rate coefficient is a weak ($\sim T_i^{1/3}$) function of ion temperature and dominates both recombination and ionization for $T_e < 10$ eV. The ionization and recombination data are obtained from Johnson & Hinnov [27], and the charge-exchange data is adapted from Hutchinson [26]. Hutchinson indicates that the charge-exchange rate coefficient still exceeds that for ionization for $T_e > 10$ eV, contradicting Fig. 2.2. This may be explained by the fact that the data are obtained from two separate sources. This may be resolved by obtaining rate coefficient data from established scientific databases. It is appropriate to use data from Johnson & Hinnov here since we use their data for H_α interpretation as well. Nevertheless, this small discrepancy in relative magnitude between charge-exchange and ionization rate coefficients is of minor importance to the present work since both ion and electron temperatures are not accurately known.

2.3 Neutral Density & H_α

The hydrogen Balmer- α line (H_α , $\lambda = 656.285$ nm) is emitted when a bound electron spontaneously decays from the $n = 3$ principal quantum state to the $n = 2$ principal quantum state in a hydrogen atom. Thus, the emissivity (photons per unit volume per unit time) of H_α is a direct measurement of the density of the $n = 3$ quantum state, i.e. $\gamma_\alpha = A_{32}N_3$, where A_{32} is the Einstein coefficient for spontaneous emission.

In order to convert H_α intensity into information about neutral density, we require a radiative-collisional model which will determine the population of the appropriate excited state for a given set of relevant conditions, such as electron temperature, electron density, and ground state atomic hydrogen (neutral) density. The difficulty

lies in obtaining this relationship for values of these conditions which are inconsistent with thermal equilibrium for a local volume, or local-thermal-equilibrium (LTE). If we could satisfy LTE conditions, one could easily determine the population of any quantum state by calculating Boltzmann factors. However, in order to achieve LTE, the characteristic collision rates for producing excited atomic states (electron and proton impact excitations) must be much larger than the spontaneous (radiative) decay rates of the excited states (Einstein coefficients). Criterion for meeting LTE conditions has been studied in detail by Griem, the application of which indicate that, for estimated MCX discharge temperatures, electron densities are several orders of magnitude too low to satisfy LTE, and marginal for the $n = 3$ quantum state to be considered in LTE with free electrons and higher excited states [28], therefore an alternate treatment is required.

Atomic & molecular processes are currently a subject of much research in the context of fusion research [29], indeed there are several collisional-radiative codes which address “non local thermal equilibrium” or NLTE [30]. However, these sophisticated treatments are not necessary at this stage of neutral particle studies on MCX. Johnson & Hinnoy [27] have produced a seminal work which provides the foundational principles upon which the more developed treatments are based. Using appropriate effective rate coefficients, Johnson & Hinnoy solved a matrix of rate equations consisting of the collision rates (collisional excitation, collisional de-excitation, ionization, and recombination) as well as atomic processes, such as radiation and absorption. They used a coronal type model, which essentially assumes that free electrons are in thermal equilibrium and that bound electrons in a sufficiently high quantum state are part of the continuum of free electrons, i.e. the atom is effectively ionized for these states. The most current collisional-radiative codes are capable of considering not only higher quantum states than those included in the calculations of Johnson & Hinnoy, but also more complex processes such as molecular dissociation of hydrogen

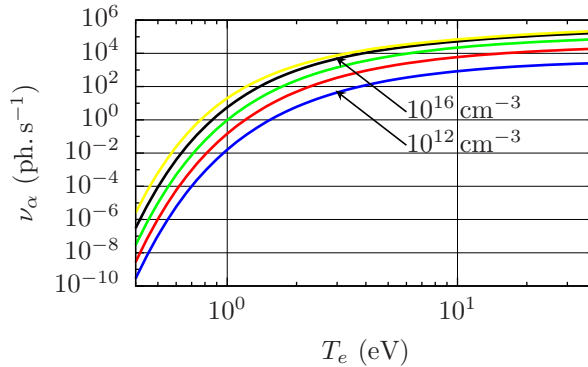


Figure 2.3: Shown is the emission rate of H_α as a function of electron temperature for various electron densities. Strong temperature dependence is seen for $T_e \lesssim 10$ eV.

as well as impurity species effects [30]. Nevertheless, under many circumstances, these represent higher order corrections to the Johnson & Hinnov results.

Since we are using the results of Johnson & Hinnov it is necessary to describe qualitatively the data which will be used to analyze the experimental data in this dissertation. Generally, the population of the quantum state $n = 3$ of hydrogen, and hence H_α emissivity, depends on electron temperature, electron density, and neutral density. We can describe this relationship with the following expression.

$$\gamma_\alpha(N, n_e, T_e) = N\nu_\alpha(n_e, T_e) \quad (2.12)$$

The emissivity of H_α is proportional to the neutral ground state density (N) and the emission rate (ν_α), which is a function of electron density and temperature. This expression can be obtained from Eqs. (12) & (15) in Johnson & Hinnov [27], where steady state is assumed and the ionization term in Eq. (12) is of higher order. Here, the emission rate, ν_α , is comprised of tabulated values found in Johnson & Hinnov.

Figure 2.3 shows the emission rate of H_α as a function of electron temperature from about 0.4 eV to 40 eV for various electron densities. Notice the strong temperature dependence for $T_e \lesssim 10$ eV. The density dependence is relatively weak in comparison.

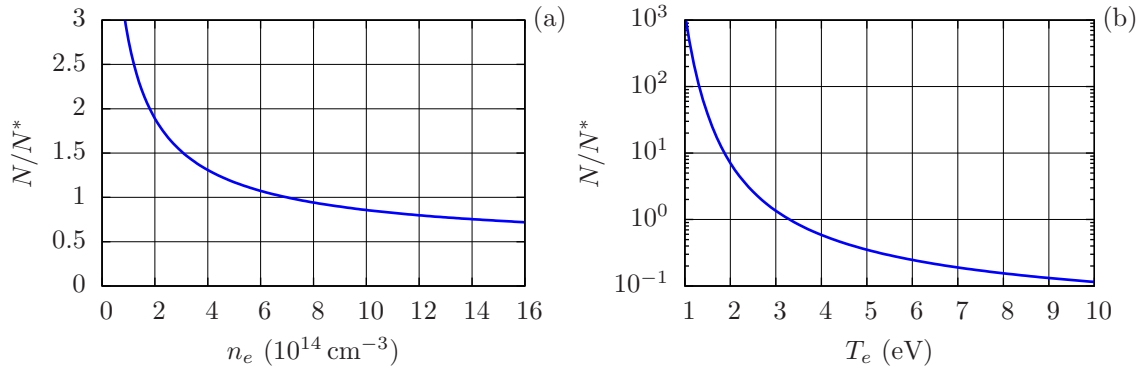


Figure 2.4: Shown is the sensitivity of neutral density estimates to electron density (a) and electron temperature (b). Nominal plasma conditions are chosen to be $n_e = 7 \times 10^{14} \text{ cm}^{-3}$ and $T_e = 3.3 \text{ eV}$. Here, the neutral density calculations are normalized to that resulting from these nominal conditions and a fixed emissivity. For each plot only the abscissa parameter is changed, while the other is fixed at the nominal value.

We will be assuming $T_e = 3.3 \text{ eV}$ [11] and constant electron densities for analysis presented in this work, therefore it is appropriate to show the sensitivity of neutral density estimates around $T_e = 3.3 \text{ eV}$ and a nominal $n_e = 7 \times 10^{14} \text{ cm}^{-3}$ for a fixed emissivity (Fig. 2.4). Because a given emissivity value is proportional to neutral density, the sensitivity of calculated neutral density to electron temperature and density is just $N/N^* = \nu_\alpha^*/\nu_\alpha$, where the superscript “*” indicates the nominal value, i.e. $\nu_\alpha^* = \nu_\alpha(7 \times 10^{14} \text{ cm}^{-3}, 3.3 \text{ eV}) \sim 5.5 \times 10^3 \text{ ph. s}^{-1}$. We see in Fig. 2.4(a) that for the ranges in density presented in this work the estimate of neutral density may be between about $0.7\times$ and $3\times$ the value estimated. Similarly, Fig. 2.4(b) indicates a possible range between about $0.1\times$ to $10^3\times$. Clearly the electron temperature dependence is the most significant, underscoring the need for improved temperature measurements.

2.4 MCX Neutral Models

The purpose of the H_α emission detector system is to understand the distribution of neutrals in MCX discharges. This, in turn, should give us insight into prevalent

neutral-catalyzed transport mechanisms. As such, we require some theoretical prediction of neutral behavior against which physical measurements can be compared, i.e. a neutral model. Furthermore, given the fact that H_α emissivity generally depend on electron temperature, electron density, and neutral density, it is desirable that we be able to vary these parameters in our model in order to make appropriate comparisons.

In this section, we present two models against which experimental data will be compared: one in which centrifugal effects are ignored and one in which centrifugal effects are included. Both are isothermal diffusion models with perfect recycling at the boundary and are based on work done by Goldston & Rutherford [31] and adaptations done by Ng [32]. The present models have been modified from Goldston & Rutherford's treatment in that density dependence of the diffusion coefficients is maintained and the set of equations is solved for moderate system sizes.

2.4.1 Numerical Modified Goldston-Rutherford Model

The first model, termed Numerical Modified Goldston-Rutherford (NMG), is a 1D slab model which ignores centrifugal effects and is identical to the 1D model presented by Ng [32]. NMG is derived in detail in Appendix A but here we describe the final result.

$$y'' = \frac{2}{3} (y^2 - c\sqrt{y}) \quad (2.13)$$

$$\hat{n} = \sqrt{y} \quad (2.14)$$

$$\hat{N} = \frac{1}{3} D (c - y^{3/2}) \quad (2.15)$$

Here, in application to MCX discharges, the spatial coordinate is the radius, r . Also, in the above equations, $\hat{n} = n/n_0$, $\hat{N} = N/n_0$, and lengths are normalized to l_0 ,

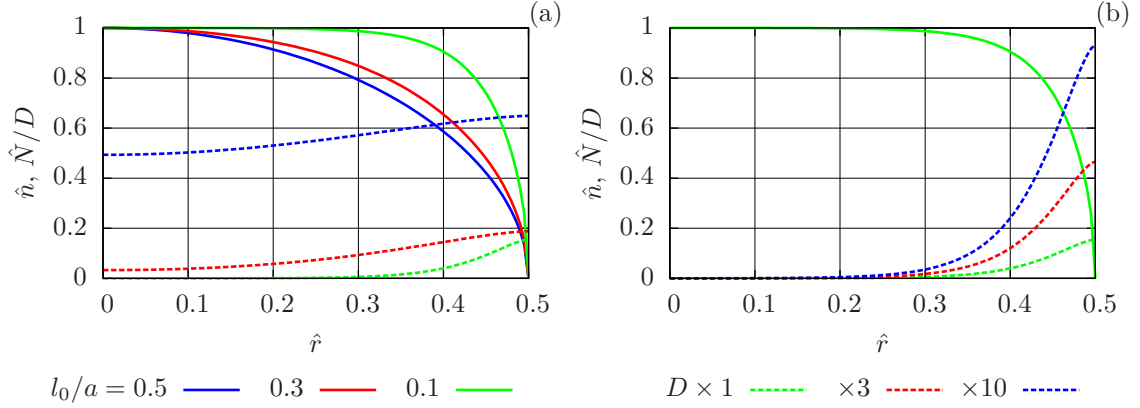


Figure 2.5: Shown are normalized plasma and neutral density profiles for the NMG model. Figure (a) shows the profiles for different neutral penetration depths, l_0 . The neutral density profiles are normalized by D (see Eq. 2.15) in order to be shown with the plasma density profile. Figure (b) shows the plasma density for $l_0/a = 0.1$ and the corresponding neutral density scaling for different D .

where n_0 is the maximum plasma density and we have the following definitions.

$$D \equiv \frac{mc^2 n_0^2}{B_0^2} \eta \alpha_{cx} \quad (2.16)$$

$$l_0 \equiv \sqrt{\frac{T}{mn_0^2 \alpha_i \alpha_{cx}}}, \quad (2.17)$$

where terms have their usual meanings. The interpretation of l_0 is the geometric mean of the ionization and charge-exchange mean-free-paths for a neutral particle at the location of maximum plasma density, i.e. $\sqrt{\lambda_i \lambda_{cx}}$.

We are now in a position to discuss the impact of the relevant parameters on the plasma and neutral densities. First, Eq. (2.13) is a differential equation of order unity which determines the shape of the density profiles and c is a constant of integration. This shape is only a function of the system size in units of the neutral penetration distance, l_0 ; thus, for a fixed system size the density profiles will be determined by the neutral penetration depth. It is seen from Eq. (2.14) that \hat{n} follows directly from the solution to Eq. (2.13). \hat{N} also follows directly from the solution of Eq. (2.13), but its amplitude is scaled by D .

Figure 2.5(a) shows how both \hat{n} and \hat{N} profiles change with l_0 , while holding D fixed. The plot abscissa is scaled to a fixed system size, $a = 1$, thus $-0.5 \leq \hat{r} \leq 0.5$ is the system domain where $\hat{r} = (r - r_0)/a$ and the center of the system is located at radius r_0 . Due to the symmetry of the solution, only half of the system domain is plotted. Notice that the neutral penetration relative to the system size (0.5, 0.3, and 0.1) changes the gradients of the density profiles and pushes the interaction region further toward the edge, as expected. Also notice, that as the neutral penetration distance increases, the neutral density increases relative to the plasma density. This effect can be understood by the dependence of l_0 on the ionization rate coefficient. If α_i is suppressed, then, for fixed D , fewer neutrals that arrive at the center will be ionized, thus increasing their population until the neutral loss balances the diffusion. Note that we cannot produce this result by changing either n_0 or α_{cx} since these also appear in Eq. (2.16).

Figure 2.5(b) shows different D scaling for fixed $l_0/a = 0.1$. Since the system size is fixed, the solution to Eq. (2.13), and hence \hat{n} , is unchanged (shown as the green curve). Clearly, \hat{N} scales linearly with D .

2.4.2 Numerical Modified Goldston-Rutherford Centrifugal Model

The second model, termed Numerical Modified Goldston-Rutherford Centrifugal (NMGC), is identical to NMG except that centrifugal effects have not been ignored. The inclusion of the centrifugal term is entirely the work of the author. This model is also

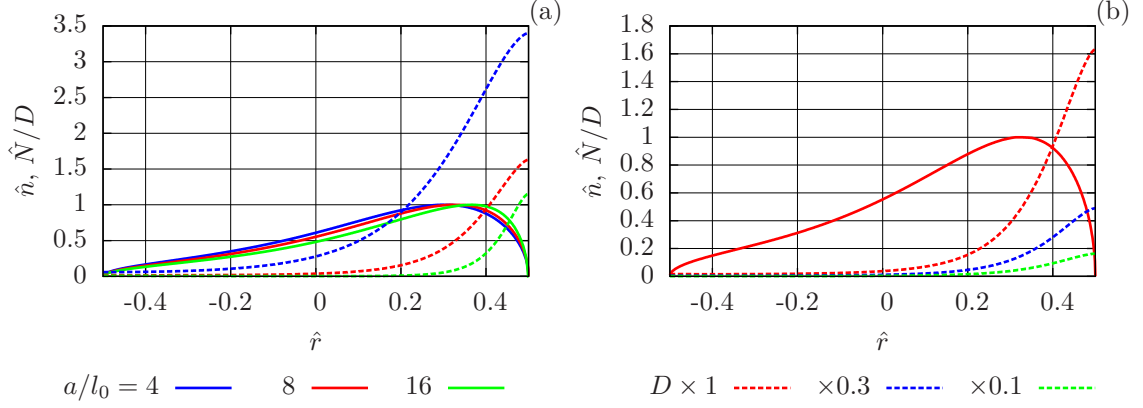


Figure 2.6: Shown are the normalized plasma and neutral density profiles with centrifugal effects for different neutral penetration depths (a) and different D scaling (b).

derived in Appendix A and the final result is as follows.

$$y''' = -\hat{g}y^2 - \hat{g}\hat{g}'y + \hat{g}''y + \frac{3}{2}\hat{g}'y' - \hat{g}^2y' + 2\hat{g}y'' - \frac{1}{2}\hat{g}\frac{(y')^2}{y} + yy' + \frac{1}{2}\frac{y'}{y}y'' \quad (2.18)$$

$$\begin{aligned} \hat{n} &= y^{1/2} \\ \hat{N} &= D\frac{\hat{g}y' + \hat{g}'y - y''}{\sqrt{y}}. \end{aligned} \quad (2.19)$$

The same definitions used for NMG also apply here and familiar quantities are normalized by n_0 and l_0 . The normalized centrifugal term is manifested as \hat{g} , which is the same for both the neutral and plasma fluids. This centrifugal term depends on the plasma rotation velocity, but for simplicity is chosen to be parabolic (see Appendix A). The expression for g is as follows.

$$\hat{g} = \frac{M_s^2}{\hat{r}_0} \left(1 - \frac{4\hat{r}^2}{\hat{a}^2} \right),$$

where $M_s \cong 2$ is the ion sonic mach number, $\hat{r}_0 = r_0/l_0 = 15 \text{ cm}/l_0$ is the normalized “center” of the plasma, and $\hat{a} = a/l_0 \cong 20 \text{ cm}/l_0$ is the nominal plasma width.

Figure 2.6(a) shows how both \hat{n} and \hat{N} profiles change with l_0 and constant centrifugal effects, while holding D fixed. The plot abscissa is scaled to a fixed system size, a , similar to Fig. 2.5 except that the full normalized system is shown because the centrifugal effects break the symmetry. Notice that as the profiles are relatively insensitive to neutral penetration lengths indicating that the centrifugal terms dominantly affect the solution profiles. However, like NMG, the neutral penetration depth affects neutral density relative to the plasma density. \hat{N} scales linearly with D , as before (Fig. 2.6(b)).

2.4.3 H_α Emissivity Profiles

In Secs. 2.4.1 & 2.4.2 we saw normalized plasma and neutral density profiles resulting from the NMG and NMGC models. Together with electron temperature and a radiative-collisional model (discussed in Sec. 2.3), these profiles imply an H_α emissivity profile. We display these emissivity profiles in this section using nominal MCX discharge conditions ($\mathcal{R} = 6$, $n_0 = 7 \times 10^{14} \text{ cm}^{-3}$, $B_{\text{mid}} = 0.21 \text{ T}$, $T_e = 3.3 \text{ eV}$, and $T_i = 15 \text{ eV}$).

Figure 2.7 shows the H_α emissivity profile resulting from the NMG model (a) and the NMGC model (b) under the same nominal discharge conditions. The models do not determine the locations of the inner and outer-most magnetic flux surfaces; these are chosen based on a vacuum magnetic field-line map and they determine the absolute system size. The nominal discharge conditions determine l_0 and D . We wish to point out two features resulting from the NMG model (Fig. 2.7(a)). First is the hollow emissivity profile. This is due to the symmetry of the solution, with the emissivity peaks resulting from the larger neutral density near both the inner and outer-most flux surfaces. Second is that the emissivity drops rapidly in close proximity to these flux surfaces due to the rapid decrease in electron density near the plasma boundary. The emissivity profile resulting from the NMGC model (Fig. 2.7(b)) shares

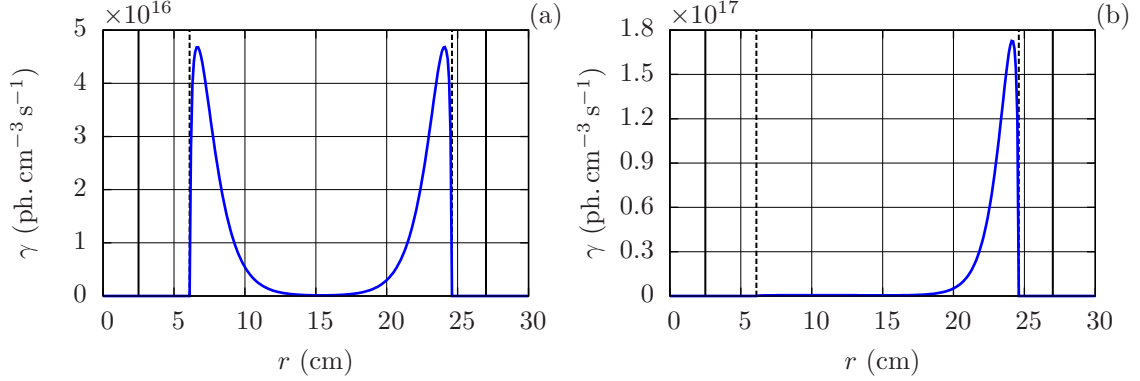


Figure 2.7: Shown are nominal H_α emissivity profiles with (b) and without (a) centrifugal effects. Nominal discharge conditions were applied to the NMG and NMGC models ($\mathcal{R} = 6$, $n_0 = 7 \times 10^{14} \text{ cm}^{-3}$, $B_{\text{mid}} = 0.21 \text{ T}$, $T_e = 3.3 \text{ eV}$, and $T_i = 15 \text{ eV}$). The resulting plasma and neutral density profiles, as well as $T_e = 3.3 \text{ eV}$, were used to determine the emissivity profiles. The vertical dashed lines indicate the locations of the inner-most and outer-most magnetic flux surfaces. The vertical solid lines indicate the locations of the inner cathode and vacuum chamber wall.

this feature at the outer-most flux surface for the same reason. However, this profile is not hollow due to the centrifugal force driving both neutrals and plasma toward the outer-most flux surface.

2.5 Conclusions

In this chapter we have shown the basic principles underlying centrifugal confinement, motivating the need to achieve high plasma rotation speeds. We have also discussed the processes which may impede plasma rotation in the context of neutral drag which motivates the study of neutral particles in MCX discharges.

We have also presented two fluid models representing possible neutral behavior and its effect on both neutral and plasma profiles. It is important to emphasize that these models are at the beginning stages of development. In particular, they assume isothermal conditions and are fairly liberal in the scaling of terms in the full set of MHD equations. Nevertheless, they provide a good starting point by providing predicted profiles and scaling laws. It should also be noted that the boundary

conditions used in these models may not accurately reflect those in MCX discharges. The models assume a hard boundary which provides perfect recycling of plasma to neutrals ($nu = -NU$) rather than the gas blanket possibly surrounding MCX plasma discharges.

Finally, we have illustrated the relationship between atomic hydrogen, electron density, electron temperature, and the resulting Balmer- α emission, allowing us to estimate the atomic hydrogen density.

Chapter 3

The H $_{\alpha}$ Emission Detector

The H $_{\alpha}$ emission detector (HED) was designed and constructed by the author primarily to measure the absolute emission of the Balmer- α line of hydrogen (656.285 nm). The purpose in measuring intensity of a spectral line in the primary neutral species is to be able to calculate its density, i.e. spectral emission line intensity is related to species population. In this chapter we present a detailed description of an individual HED, including all of its optical components. We also describe the time and spectral response of a typical HED. Finally, include a detailed description of the calibration procedure used to establish the absolute emission response.

3.1 H $_{\alpha}$ Emission Detector Characteristics

There are two versions of the HED system, Version-1 and Version-2. HED systems numbered 1–7 employ Version-1 and systems numbered 8–18 employ Version-2. The difference between the two versions is the model of photo-detector and the type of instrument amplifier used to condition the signal for data acquisition. These will be discussed in more detail in this section. The H $_{\alpha}$ emission detector consists of five main components: 1. the collection optics assembly, 2. an optical fiber, 3. a filter assembly, 4. a photo diode detector, and 5. an instrument amplifier. The following paragraphs describe these components, their sub-components, and their purpose in more detail. Figure 3.1 shows a schematic drawing of a typical Version-1 HED system, highlighting the most relevant components. In addition, it also shows a conceptual illustration of the HED viewing volume, which is discussed in detail in Appendix B.

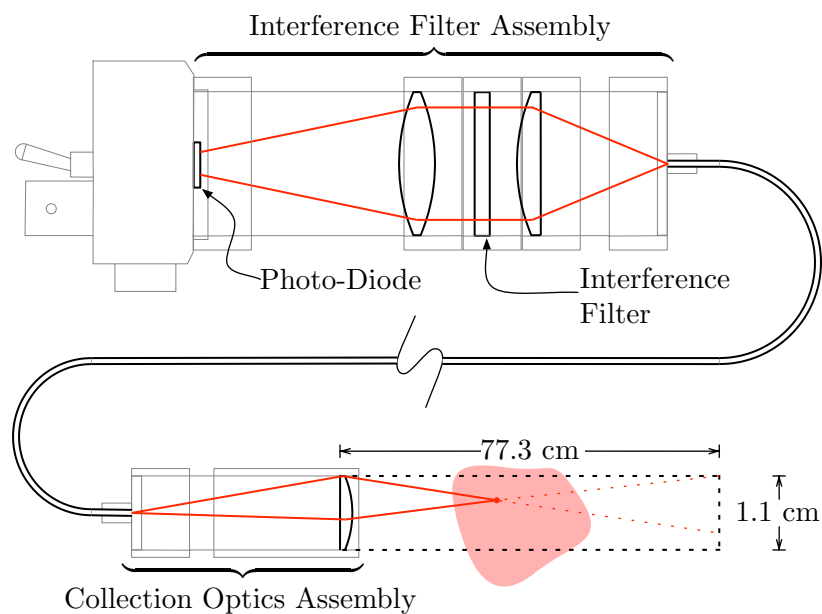


Figure 3.1: Shown is a schematic drawing of the H α emission detector. Depicted is Version-1 which uses the Thorlabs DET110 silicon photo-diode unit. For clarity, 1" optics are illustrated for the filter assembly; however, all HED versions use 1/2" optics. Version-2 is more compact since the Thorlabs PDA36A silicon photo-diode unit contains an integrated instrument amplifier.

The collection optics assembly consists of a Thorlabs standard 1/2"×1" optical lens tube, 1/2"×1" adjustable lens tube, a 1/2" SMA fiber adapter, and a 1/2" plano-convex lens with a 40 mm focal length. The lens tubes serve to position the optical fiber relative to the collection lens and eliminate stray light from entering the fiber optic cable. The fiber is positioned approximately 2 mm outside the focal length of the lens, resulting in an image distance of 77.3 cm and an image size of 1.1 cm (about 18× magnification). The position of the fiber relative to the lens was designed so that the optical image of the fiber tip would be the same size as the clear aperture of the collection optics assembly and that the fiber image would be at a distance larger than the diameter of the MCX vacuum chamber (55.2 cm). This creates a virtual "tube" defining the viewing volume of an HED system. This viewing volume is discussed in Appendix B.

The optical fiber transmits the light collected by the collection optic assembly to the optical filter assembly. The optical fiber has a 600 μm diameter glass core and is 20 m long. By using an optical fiber we are able to position the electronic components of the HED system away from possibly harmful magnetic fields. The core size of the fiber-optic was chosen to maximize the amount of light delivered to the photo-detectors while allowing sufficient collimation of the light for an interference filter in a relatively compact design.

The filter assembly consists of two collimating lenses and an interference filter¹, housed in light-tight lens tubes. The optical filter assembly uses Thorlabs standard 1/2" optics. This compact design was developed in order to reduce the physical size and cost of an individual HED system. The low cost makes it possible to assemble an entire filter assembly for any available optical bandpass filter, thus allowing intensity measurements of other emission lines.

¹CVI Melles-Griot F1.5-656.2-4-0.50

The Version-1 photo-detector is the Thorlabs DET110 and the Version-2 photo-detector is the Thorlabs PDA36A. These two units differ in that the PDA36A contains an integrated amplifier, but the photo-diode and accompanying circuitry are identical. The photo-diode is a 3 mm×3 mm silicon diode with an optical response in the visible spectrum (350 nm–1100 nm). The DET110 and PDA36A have output signal bandwidths as high as a few hundred megahertz, depending on the output impedance (DET110) or chosen gain (PDA36A). The PDA36A supersedes the DET110 in Thorlabs product line and is a welcome improvement due to its integrated instrument amplifier.

The instrument amplifier for HED Version-1 is a transimpedance amplifier with two gain settings and was designed by the author for use with the DET110. It was designed to maximize signal bandwidth ($\gtrsim 500$ kHz) and transimpedance (~ 500 kV/A), thus optimizing signal strength and time response. The PDA36A comes with an integrated transimpedance amplifier with many gain settings. The gains and bandwidths are listed in Table-3.1. The values of the transimpedance gains listed in Table-3.1 are for reference purposes only; their precise values are of little importance since the absolute response of the whole system is consolidated into a single calibration factor, which is the topic of Sec. 3.4.2.

The output signal bandwidths of the various gain settings for Version-1 and Version-2 systems were experimentally verified using a high-speed LED. The led was DC biased and fed a sinusoidal signal from a signal generator. The bandwidths listed in Table-3.1 represent the -3 dB point for the associated gain setting.

3.2 Vacuum Chamber Reflections

The multi-chord HED array is comprised of 16 HEDs, each of which collect chord-integrated emissions. The viewing chord of each terminates on the interior of the MCX vacuum chamber or opposing viewport. The MCX vacuum chamber is made

Table 3.1: Typical HED Gains & Signal Bandwidths

Transimpedance (kV/A)	Bandwidth (kHz)
Version-1	
50	550
500	550
Version-2	
1.51	17×10^3
4.75	12.5×10^3
15	2100
47.5	785
151	320
475	100
1500	37.5
4750	12.5

of brushed stainless steel and has diffusive reflection properties. It is, therefore, very important to characterize the amount of light which can be “scattered” into the sight of a single chord by the interior of the vacuum chamber. To this end, a bench test was performed on a piece of stainless steel similar to that of the vacuum chamber. In addition, an in-situ test was performed using a piece of flock-paper as a type of beam dump. The results of these tests are presented in this section and show that reflections need not be considered under the present surface conditions of the MCX vacuum chamber.

A simple bench test was performed to ascertain the reflectance properties of stainless steel. A piece of 304 stainless steel plate with #4 brush surface finish was acquired by Kurt J. Lesker Co. This is the same material, surface finish, and manufacturer, of the MCX vacuum chamber. An HED collection optic assembly was placed with a view perpendicular to the face of the steel plate and at a distance of 23 cm from the plate. A uniform light source² was placed at a distance of 26 cm from the plate, illuminating the same spot on the plate which is viewed by the HED collection optic.

²Labsphere IHLS-100-075 halogen lamp and 3P-GPS-040-SF integrating sphere.

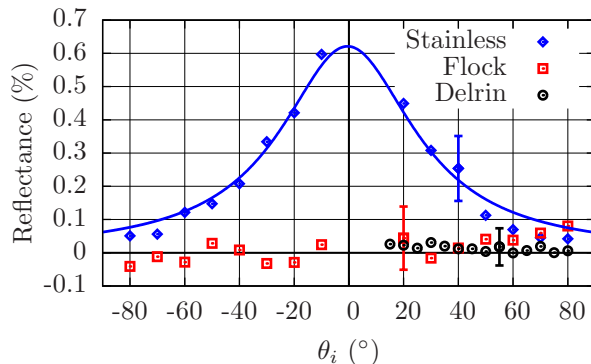


Figure 3.2: Shown are the results for the reflectance tests performed on stainless steel, flock paper, and delrin. The stainless steel was obtained from Kurt J. Lesker Co. and had a #4 brush finish (similar to the interior of the vacuum chamber). The delrin is black in color and its surface had been sand-blasted.

The uniform source was varied in angular position but its distance from the illuminated target spot was kept constant. For each angular position of the source, 10,000 measurements (10 seconds at 1 kHz sampling rate) were made by a data acquisition system. Averages and standard deviations were calculated from the measurements at each angular position. A control measurement was made by placing the HED collection optic assembly at a distance of 49 cm from the uniform source and viewing the source directly. A dark measurement was taken as well in order to subtract ambient light effects and to account for electronic signal offsets.

The results of the stainless steel reflectance tests are shown in Figure 3.2 as the blue data. The blue curve is a Lorentzian fit to the data. The standard deviations of all measurements were similar and are represented by the single error bar. Here the measurement results were normalized by the control measurement (after subtracting dark measurements), indicating about a 0.6% maximum reflectance. This may seem to be a rather insignificant amount; however, the relevant number is not the maximum reflectance but the integration of the reflectance over all angles. This is because an MCX discharge is approximately an extended emission source, so that light from virtually any angle may be scattered into the line of sight of an HED view chord.

The sum of the contribution of reflection from all angles reveals a total contribution that is 50% of the control measurement, which is too large to leave unaddressed.

Other plasma confinement experiments have successfully corrected for optical reflections in the data analysis [33], but it is more desirable to eliminate them altogether. For this purpose we tested the possibility of using flock paper on the vacuum chamber wall and a delrin flange as methods for mitigating reflections. Bench tests were performed for both flock paper and delrin (with sandblasted surface finish) with the identical setup as that used for the stainless steel. The results are shown in Figure 3.2 for flock paper (red squares) and delrin (black circles). The results show that reflections from both flock paper and delrin are indistinguishable from zero.

Flock paper is not ideal for insertion into the vacuum chamber. The possibility of out-gassing aside, the primary concern is that the plasma may damage it, thereby contaminating the plasma; nevertheless, its attractive reflection property warranted an in-situ test. Before any flock paper was attached to the MCX vacuum chamber, an HED was configured with an 11 cm impact parameter view chord. Several discharges were taken at nominal MCX parameters ($V_B = 10$ kV, $B = 2.2$ kG, $P_{\text{fill}} = 5$ mTorr, and $\mathcal{R} = 7$) and the H_α signal from these served as a control. Then the vacuum chamber was opened and a 2" \times 2" piece of flock paper was adhered to the vacuum chamber at the location where the view chord terminated. Several discharges were taken at the same parameters and the H_α signals recorded. Any significant difference between the two sets of signals should indicate the extent to which reflections contribute to a chord integrated H_α signal.

The results of the in-situ flock paper tests are shown in Figure 3.3. Shown are the bank voltages (red) and HED signals (blue) averaged over the time interval $2 \text{ ms} < t < 3 \text{ ms}$. The error bars represent the standard deviation from the mean for that time interval. It is worthy to note that the fluctuations represented by the error bars are not an uncertainty in the measurements (electronic noise) which are of order

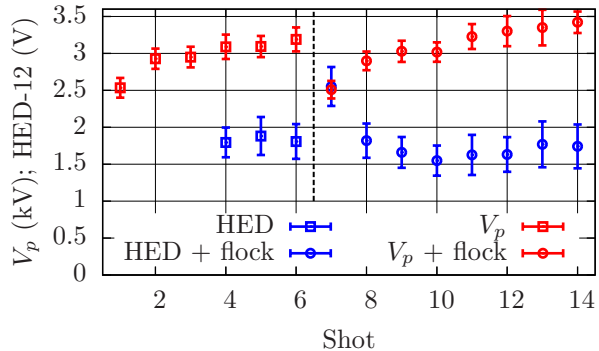


Figure 3.3: Shown are the results of the in-situ flock paper test. Left of the vertical dashed line are the control discharges (no flock paper present). At the dashed line flock paper was inserted and the remaining discharges taken.

0.5 mV, but are real fluctuations in the plasma behavior. To the left of the vertical dashed line are the control discharges (square data points). Notice the initial rise in bank voltage for the first few discharges, due to conditioning effects. To the right of the vertical dashed line are discharges taken with the flock paper present (circle data points). Notice the initial rise in bank voltage, again due to conditioning after recently breaking vacuum. Also notice the elevated H_α signal for the first discharge and a drop in the signal that correlates with the rising bank voltage.

The H_α signal levels after conditioning are comparable (within 10%) between the control discharges and those with the flock paper present and do not indicate a 50% reflection contribution as predicted by the bench tests. The in-situ test seems to indicate that, in fact, reflections are not a problem under the present surface conditions of the vacuum chamber. The inside of the vacuum chamber at the mid-plane leaves no room for more robust reflection mitigation techniques, such as stacked razor blades, hence flock paper may be the only possible mitigation mechanism. In consideration of this, the null result of the in-situ test is fortunate since the flock paper showed significant damage after only 8 discharges. Figure 3.4 shows a photograph of the the flock paper adhered to the vacuum vessel (left) and a comparison between the flock paper removed from the vacuum chamber and a virgin piece cut from the same stock

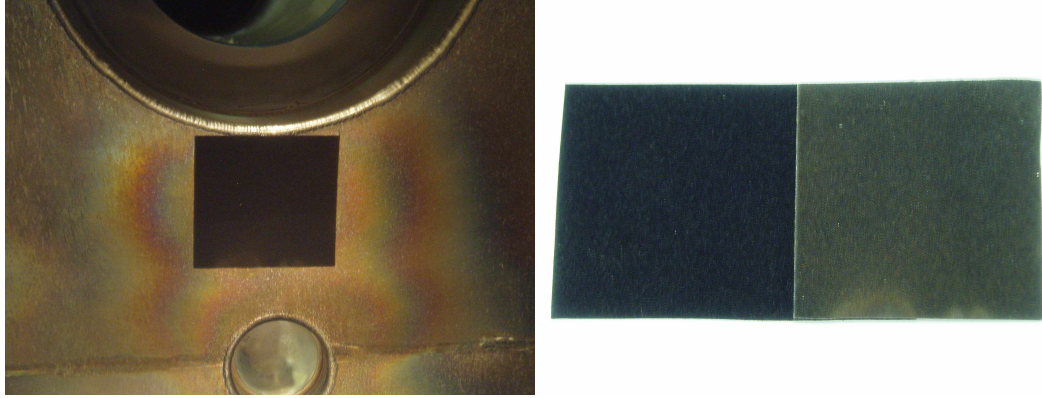


Figure 3.4: Shown is a piece of flock paper adhered to the interior of the vacuum vessel (left) and is located just below an upper-tangential viewport. The discoloring of the vacuum vessel was present before insertion of the flock paper. The same piece of flock paper is compared to an undamaged piece (right).

(right). The indifference to the flock paper may be explained by the condition of the interior of the vacuum chamber. After many years and several thousand discharges, the interior of the vacuum chamber has become discolored and dulled, as can be seen in Fig. 3.4. This is in contrast to the new “shiny” steel plate acquired for the bench tests.

3.3 Viewport Transmission

Ideally, each HED system would be calibrated in-situ, thus incorporating all of the optical elements. However, due to the proximity of the vacuum chamber to the expected plasma location and the wide range of viewing angles required to view the entire plasma cross-section with a multi-chord array (particularly at the outer edge), an in-situ calibration is impractical. Fortunately, the entire optical and electrical system of an HED can be treated as one system during calibration and only the viewport must be treated separately. Each HED unit will be sighting through the viewport at different angles, so it is important to characterize the viewport’s optical transmission as a function of incident angle. We measured the transmittance of the

viewport and present the results in this section, comparing them to basic optical theory.

The transmittance of light through a boundary between two mediums of different refractive index can be found in many standard optics texts [34–36]. The total power transmittance through a single boundary is

$$T(\theta) = t_{\perp}^2 + t_{\parallel}^2 \quad (3.1)$$

where t_{\perp} and t_{\parallel} are the transmittances for the electric field perpendicular and parallel to the plane of incidence, respectively. Their expressions are in terms of the incident angle and the indices of refraction for the incident (n_i) and transmitted (n_t) medium.

$$t_{\perp} = \frac{2n_i \cos \theta_i}{n_i \cos \theta_i + \sqrt{n_t^2 - n_i^2 \sin^2 \theta_i}} \quad (3.2)$$

$$t_{\parallel} = \frac{2n_i n_t \cos \theta_i}{n_t^2 \cos \theta_i + n_i \sqrt{n_t^2 - n_i^2 \sin^2 \theta_i}} \quad (3.3)$$

We are interested in determining the transmission across two boundaries: from vacuum to glass to air. The total transmittance then becomes

$$T(\theta) = t_{\perp,12}^2 t_{\perp,23}^2 + t_{\parallel,12}^2 t_{\parallel,23}^2 \quad (3.4)$$

Here, the numeric subscripts indicate the boundary and direction of transmission, e.g. “12” means transmitting from medium 1 into medium 2.

The viewport through which the HED array views is a Kurt J. Lesker VPZL-800 made of Kovar 7056 crown glass with refractive index $n = 1.487^3$. The viewport was removed from the vacuum chamber in order to measure its transmittance. An HED unit was placed a fixed distance from a uniform light source, directly viewing its output port, and control and dark measurements were taken. The glass viewport was

³www.corning.com

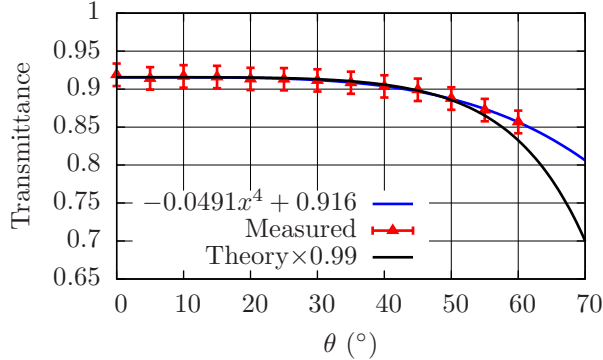


Figure 3.5: Shown are the results of the viewport transmittance test. The black curve is the predicted transmittance [34] (see Eq. (3.4)) with 1% absorption. The blue curve is an empirical fit to the data. The transmittance is virtually constant (92%) for all angles of interest ($< 30^\circ$).

then placed between the light source and the HED collection optic, oriented at various angles relative to the optic axis of the HED collection optic. Measurements taken at each angular orientation were recorded by a data acquisition system and included 10,000 samples (10 s at 1 kHz sample rate). The average and standard deviation was calculated for each orientation.

Shown in Fig. 3.5 are the results of the transmission measurements for the glass viewport. The red data points represent the measured transmission as a fraction of the control measurement (after subtracting dark measurements). The error bars are the standard deviation of each measurement. The black curve is the theoretical prediction expressed by Eq. (3.4) with 1% absorption ($\times 0.99$). The blue curve is a fourth-order polynomial fit to the measurements.

We see in Fig. 3.5 that the measured transmission agrees very well with Eq. (3.4), if a 1% absorption factor is included. Also of note is that the data are in agreement with the specifications of the manufacturer (92% at 589 nm). The measurement uncertainty is due to electronic noise (~ 0.6 mV). It is uncertain why the data does not agree with the theory for $\theta > 50^\circ$, but may be due to multiple reflections within the glass, which are not considered in Eq. (3.4). However, the view chords of the HED

array do not exceed 30° from normal incidence, thus the discrepancy is irrelevant. 92% transmission may be considered constant for the relevant incident angles of the HED array and is included in the overall calibration factor for each HED system.

3.4 H_α Emission Detector Calibration

Since neutral hydrogen density is related to the intensity of radiative transitions from its excited states, it is necessary to calibrate the absolute spectral response of the HED system. An HED system consists of several optical components, each contributing to the overall loss of light intensity reaching the photo-diode detector, ultimately affecting the signal amplitude. Furthermore, the absolute spectral response of the DET110 and PDA36A photo-detectors are not calibrated by the manufacturer.⁴ These effects can vary from one HED system to another, requiring each unit to be independently calibrated. The following sections describe in detail the calibration procedures needed to fully characterize an HED system for interpreting H_α emissions. Section 3.4.1, details the procedure for obtaining the shape of the spectral transmission of the optical components of a single HED system. Section 3.4.2 details the absolute calibration procedure in mathematical language, culminating in an overall calibration factor for an HED system.

3.4.1 H_α Emission Detector Spectral Calibration

Clearly, if we wish to measure the emission intensity of a particular spectral line, an appropriate filter must be chosen both to include the line of interest and to exclude all other possible emission lines. While every optical component of an HED system will have a wavelength dependent transmittance, the variation of these spectral transmittances are considered to be very small over the wavelength range for which

⁴The specification sheet accompanying these detector models describe a spectral response curve which is intended for estimation purposes only and does not represent a bona-fide calibration.

the interference filter's transmittance is significant. Therefore we only need to consider the spectral transmittance of the interference filter. Furthermore, the spectral response of the DET110 and PDA36A are limited to wavelengths between 300 and 1200 nm, therefore the rejection characteristics of filter only need to be demonstrated within this wavelength domain. However, it will be shown in Sec. 3.4.2 that only an accurate knowledge of the *shape* of the spectral transmittance for the interference filter, $F(\lambda)$, is required to complete the calibration, since the absolute response is absorbed into the total response of the system.

The shape of the spectral transmittance of the interference filter is obtained as follows. An HED collection optic directly views the output port of a uniform calibrated light source, transmitting the light through an HED optical fiber and through an HED interference filter assembly. However, the interference filter assembly is detached from the photo-diode unit and coupled to one of the fiber optic cables attached to the spectrometer entrance slit. It is critical that interference filter assemblies are used in order to imitate the HED system configuration as much as possible. A different setup would not appropriately characterize any shift and/or broadening of the filter transmittance due to imperfect collimation within the interference filter assembly. A spare interference filter assembly is prepared with identical optical configuration except that the interference filter is removed. Replacing the assembly containing a filter for one that does not allows us to record the "raw" spectrum of the uniform light source for use as a control signal. The gate time of the spectrometer's CCD camera is adjusted to maximize the control signal without saturating the CCD. Many spectra are recorded with both types of filter assemblies, creating two ensembles. An ensemble average of each pixel is then taken to eliminate pixel noise. We do not smooth the data within an individual spectra since this will affect the apparent optical bandpass of the system. The two resulting spectra are then divided, yielding the precise shape of the optical bandpass of the system. Division by the control spectrum cancels the effects of the

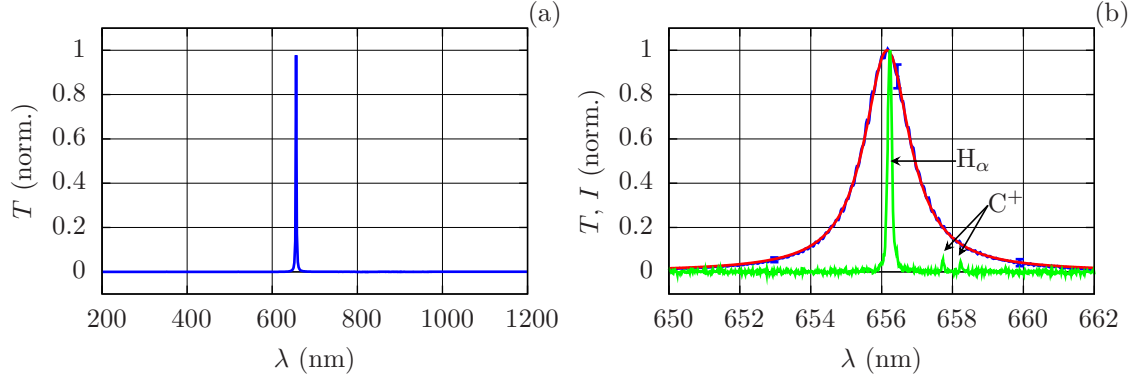


Figure 3.6: Shown is the normalized spectral transmittance of a typical HED interference filter across the visible spectrum (a), and near H_α (b). The broadband transmittance data was provided by the manufacturer. The narrow band data (blue curve with representative error bars) was produced by the author with the use of a broadband light source and spectrometer. The data is fit to a Lorentzian distribution (red curve). A spectral emission from a typical MCX discharge is shown for reference (green). Note the presence of C^+ emission lines.

spectral shape of the source as well as relative response between pixels on the CCD. The resulting spectral bandpass is then normalized to its maximum value.

The normalized spectral transmittance for a typical HED interference filter is shown in Fig. 3.6. Figure 3.6(a) shows the broadband response (supplied by the manufacturer), illustrating that the interference filter rejects appropriate wavelengths away from the H_α emission line. Figure 3.6(b) shows the optical pass-band in more detail, as measured by the author. In the vicinity of H_α there are two distinct C^+ lines (657.987 nm & 658.470 nm) appearing in MCX discharges, the intensity of which varies relative to H_α depending on the discharge parameters, particularly pre-fill pressure. It is desirable, therefore, to suppress the contribution of these lines to the signal produced by an HED system. The interference filter shows a suppression of these wavelengths by about a factor of five.

3.4.2 H_α Emission Detector Absolute Calibration

The absolute calibration of each HED system was carried out using a calibrated light source and integrating sphere (Labsphere IHLS-100-075 lamp and 3P-GPS-040-SF integrating sphere). The light source is a halogen lamp with regulated power supply. The integrating sphere is a spherical shell with a highly diffusive surface on the interior. The purpose of the integrating sphere is to produce a uniform output intensity, both in solid-angle and across the entire area of the output port. The spectral radiance at the output port of the integrating sphere is calibrated by the manufacturer. An HED system is situated to view the output port of the uniform source and the output of the HED system is collected on the same data acquisition system that is used to for standard MCX discharges (National Instruments PXI-6133 DAQ Card).

The final signal produced by an HED unit depends on the light source being viewed, how the source is viewed by the HED unit (design of the collection optic assembly), the various absolute spectral losses and responses, and electronic signal amplification. These items are separated into four functions, that, when multiplied and appropriately integrated, give the final HED signal. The source function is the spectral emissivity of the light source, $I(\lambda, \mathbf{r}, \Omega, t)$; generally this is wavelength, space, solid-angle, and time dependent, and carries units of $\text{ergs s}^{-1} \text{cm}^{-3} \text{nm}^{-1} \text{sr}^{-1}$. This will be defined later for the calibrated light source and the H_α emission line. The way in which an HED unit views the light source is defined by the optical design of the collection optic assembly. This is described by a spatially dependent, function, $g(\mathbf{r})$, which is the solid-angle seen by the collection optic assembly for an infinitesimal source located at \mathbf{r} and has units of steradians. The spectral and electronic responses of the HED system are represented by the spectral transmittance of the interference filter, $F(\lambda)$, discussed in Sec. 3.4.1, and a function $\mathcal{R}(\lambda, \omega)$ with units V s/erg . For reasons described in Sec. 3.4.1, $F(\lambda)$ has a maximum value of 1. $\mathcal{R}(\lambda, \omega)$ includes the absolute

spectral response of the solid-state photo-diode and the electronic amplification, as well as any losses incurred in the system. The ω dependence is due to the signal bandwidth determined by all electronic components involved. The final signal, $S(\omega, t)$ in volts, produced by an HED system from a general emission source is the integration over the products of all these quantities.

$$S(\omega, t) = \int_{\mathcal{V}} \int_{\lambda} g(\mathbf{r}) F(\lambda) \mathcal{R}(\lambda, \omega) I(\lambda, \mathbf{r}, \Omega, t) d\lambda d\mathcal{V} \quad (3.5)$$

Here, cylindrical coordinates (r, ϕ, z) are used with respect to the collection optics, i.e. r is measured from the optic axis, ϕ about the optic axis, and z along the optic axis. The volume integral is carried out over the relevant emission volume, i.e. the volumetric intersection of the collection optics view chord (domain of $g(\mathbf{r})$) and the emission volume (spatial domain of $I(\lambda, \mathbf{r}, \Omega, t)$).

In Eq. (3.5), determination of $F(\lambda)$ is detailed in Sec. 3.4.1 and $g(\mathbf{r})$ is discussed in detail in Appendix B. The wavelength dependence of the light source, I , is known for the calibrated light source, but only its shape is known for H_{α} . This leaves two unknowns: the amplitude of the emission line shape for H_{α} , the determination of which is the purpose of an HED system; and $\mathcal{R}(\lambda, \omega)$, the determination of which is the purpose of the calibration procedure discussed in this section. We make the following simplifications regarding the functions contained in Eq. (3.5).

1. The calibration source and H_{α} emissivity in MCX discharges are assumed to be uniform in solid-angle; therefore, all functions are independent of Ω .
2. We assume that the spectral emissivity of the source, I , does not change significantly across the optic axis (in the r direction), but may change along the optic axis (in the z direction).
3. $\frac{1}{\pi R^2} \int g(r, \phi, z) r dr d\phi = G$, the effective solid-angle, is independent of z . This is proven in Appendix B (see Figs. B.4 & B.5).

4. We assume that the unknown spectral response of the HED, $\mathcal{R}(\lambda, \omega)$, does not vary significantly in the domain of λ where $F(\lambda)$ is significant and does not vary significantly for ω less than the electronic bandwidths listed in Table-3.1, i.e. $\mathcal{R}(\lambda, \omega) = \mathcal{R}(\lambda_0)$ in the domains approximately $655 \text{ nm} < \lambda < 658 \text{ nm}$ ⁵ and $\omega < 2\pi \cdot 100 \text{ kHz}$ ⁶.

With these assumptions, Eq. (3.5) reduces to an integration over the interference filter spectral transmittance and the emission source.

$$\begin{aligned}
S(t) &= \int_{\mathcal{V}} \int_{\lambda} g(\mathbf{r}) F(\lambda) \mathcal{R}(\lambda, \omega) I(\lambda, \mathbf{r}, \Omega, t) d\lambda d\mathcal{V} \\
&= \mathcal{R}(\lambda_0) \int_z \left(\int_0^{2\pi} \int_0^R g(r, \phi, z) r dr d\phi \right) \left(\int_{\lambda} F(\lambda) I(\lambda, z, t) d\lambda \right) dz \\
S(t) &= \pi R^2 G \mathcal{R}(\lambda_0) \int_z \int_{\lambda} F(\lambda) I(\lambda, z, t) d\lambda dz. \tag{3.6}
\end{aligned}$$

The uniform light source is calibrated in spectral radiance at the surface of the output port. This means that the spectral radiance, R_S , is known as a function of λ and the functional dependence on z of the source's spectral emissivity is a Dirac-delta function, $I_L = R_S \delta(z - z_0)$, where R_S has units $\text{ergs s}^{-1} \text{ cm}^{-2} \text{ sr}^{-1} \text{ nm}^{-1}$ and z_0 is the position of the output port relative to the collection optics. Furthermore, the calibrated light source is time independent. Thus the signal produced by an HED viewing the uniform light source is

$$S_L = \pi R^2 G \mathcal{R}(\lambda_0) \int_{\lambda} F(\lambda) R_S(\lambda) d\lambda.$$

⁵Based on data sheets accompanying the PDA36A, the instrument response changes less than 1% over this interval.

⁶The transimpedance gains used for measurements during MCX discharges are 500 V/A (Version-1) and 475 V/A (Version-2).

Solving for $\mathcal{R}(\lambda_0)$ yields an expression comprised entirely of known quantities.

$$\mathcal{R}(\lambda_0) = \frac{S_L}{\pi R^2 G \int_{\lambda} F(\lambda) R_S(\lambda) d\lambda}. \quad (3.7)$$

To complete the calibration, all that remains is to consider the line shape of H_{α} in an MCX discharge. The H_{α} emission line can be approximated as a Gaussian distribution whose width is largely determined by Doppler broadening, as follows.

$$I_{\alpha}(\lambda, z, t) = \frac{hc}{\lambda_0} \frac{\gamma_{\alpha}(z, t)}{(4\pi \text{ sr.}) \sqrt{\pi} w} e^{(\lambda - \lambda_0)^2 / w^2}, \quad (3.8)$$

where $\gamma_{\alpha}(z, t)$ is the emissivity with units of [ph. cm⁻³ s⁻¹], which may be dependent on time and may change along the optic axis. An additional factor of 4π sr. is included in the denominator in order to carry the appropriate units for spectral emissivity. Here, we assume that Doppler shifts due to rotation velocity and any line broadening due to temperature and pressure will not change w enough to affect the integration over λ in any significant way⁷. Now we can present an expression for the signal obtained from an HED which is viewing H_{α} emissions.

$$\begin{aligned} S_{\alpha}(t) &= \pi R^2 G \mathcal{R}(\lambda_0) \int_z \int_{\lambda} F(\lambda) I(\lambda, z, t) d\lambda dz \\ &= \frac{S_L}{\int_{\lambda} F(\lambda) R_S(\lambda) d\lambda} \frac{hc}{\lambda_0} \int_{\lambda} \frac{F(\lambda)}{4\pi \sqrt{\pi} w} e^{(\lambda - \lambda_0)^2 / w^2} d\lambda \int \gamma_{\alpha}(z, t) dz \\ &= \frac{hc}{4\pi^{3/2} w \lambda_0} \frac{\int_{\lambda} F(\lambda) e^{(\lambda - \lambda_0)^2 / w^2} d\lambda}{\int_{\lambda} F(\lambda) R_S(\lambda) d\lambda} S_L \int_z \gamma_{\alpha}(z, t) dz \\ S_{\alpha}(t) &= \mathcal{C}_{\alpha} \int_z \gamma_{\alpha}(z, t) dz, \end{aligned} \quad (3.9)$$

where we define

$$\mathcal{C}_{\alpha} \equiv \frac{hc}{4\pi^{3/2} w \lambda_0} \frac{\int_{\lambda} F(\lambda) e^{(\lambda - \lambda_0)^2 / w^2} d\lambda}{\int_{\lambda} F(\lambda) R_S(\lambda) d\lambda} S_L. \quad (3.10)$$

⁷A rotation velocity of 50 km/s corresponds to a wavelength shift for H_{α} of $\Delta\lambda_{\alpha} = 0.1$ nm, which is much smaller than the FWHM of the interference filter (1.5 nm).

Table 3.2: HED Calibration Factors

HED	λ_0 (nm)	FWHM (nm)	\mathcal{C}_α (10^{-19} V cm ² s)
1	656.19	1.76	3.82
2	656.16	1.73	3.46
3	656.07	1.74	3.23
4	656.10	1.78	3.51
5	656.07	1.78	3.14
6	656.10	1.73	3.31
7	656.12	1.81	3.48
8	656.11	1.75	3.54
9	656.14	1.76	3.52
10	656.07	1.84	3.34
11	656.19	1.72	3.61
12	656.11	1.74	3.57
13	656.07	1.82	3.90
14	656.14	1.83	4.00
15	656.09	1.75	4.30
16	656.15	1.76	4.19
17	656.18	1.61	4.10
18	656.16	1.57	4.46

Note that G falls out of the expression for the calibration factor, \mathcal{C}_α , because it is independent of z . The integral over z in Eq. (3.9) is the subject Abel inversions discussed in Appendix C. Also notice in Eq. (3.10) that the function $F(\lambda)$ appears in both the numerator and denominator, hence an overall constant accompanying the spectral transmittance would cancel out of the expression and only the shape function is needed. The H_α line width, w , is determined from a spectral line emission measured by the spectrometer from a standard MCX discharge. Its value was determined to be about 0.06 nm, so the integration over the emission line shape may be well approximated as a Dirac-delta function. The calibration factor, \mathcal{C}_α , for each HED system is listed in Table-3.2, along with its filter's central wavelength and full-width-half-max.

3.5 Conclusions

The H_α emission detector is a compact, versatile, and inexpensive (\sim \\$1 k/channel) emission diagnostic. The modular, off-the-shelf components allow new systems to be assembled and old systems to be serviced or modified relatively easily. The system can easily be adapted for any visible emission line for which an appropriate interference filter can be obtained. In addition, the compact design of the collection optic assembly affords a large degree of freedom in the application and logistic location of the device; essentially, it can be placed at any viewport location while occupying little space. It is this versatility that motivated incorporating the same collection optic assembly for use with the 1 m spectrometer.

In this chapter, we have demonstrated that the HED is spectrally and temporally suitable for measuring absolute H_α emission from MCX discharges. In addition we have documented the characteristics of all HED systems employed on MCX, particularly the absolute calibration factors.

Chapter 4

Experimental Results & Discussion

In this chapter, we present the results of the experiment which comprise the main findings of this dissertation. We begin with a description of the MCX experiment. Radial emissivity profiles are then presented which show dominant emissions at the vacuum chamber wall. Next we present phenomenological behavior of the discharges as experimental parameters are varied. The scaling of neutral density estimates are compared with the prescription of the models presented in Sec. 2.4, showing moderate agreement in the magnetic field and pressure scans. The scaling of estimated charge-exchange times are compared to measured momentum confinement times. Lastly, we discuss the temporal behavior of radial H_α emissivity profiles.

4.1 Experiment Description

The Maryland Centrifugal eXperiment is a pulsed discharge which is sustained for about 5 ms. The driving mechanism is a set of 30 capacitors which are charged to a desired voltage. The MCX experiment is essentially the discharge of these capacitors from a central cathode to the vacuum chamber, through a volume of hydrogen gas. The capacitors provide the electric field and energy required for initial breakdown of the gas and formation of the plasma. The remaining electric potential on the capacitors then maintain the electric field in the plasma, producing the $\mathbf{E} \times \mathbf{B}$ drift rotation as well as the $\mathbf{j} \times \mathbf{B}$ driving force. The data acquisition system records data using LabVIEW PXI-6133 digitizers at 1 MHz simultaneous sampling rates. The internal clock from a single PXI-6133 DAQ card is used to trigger an external

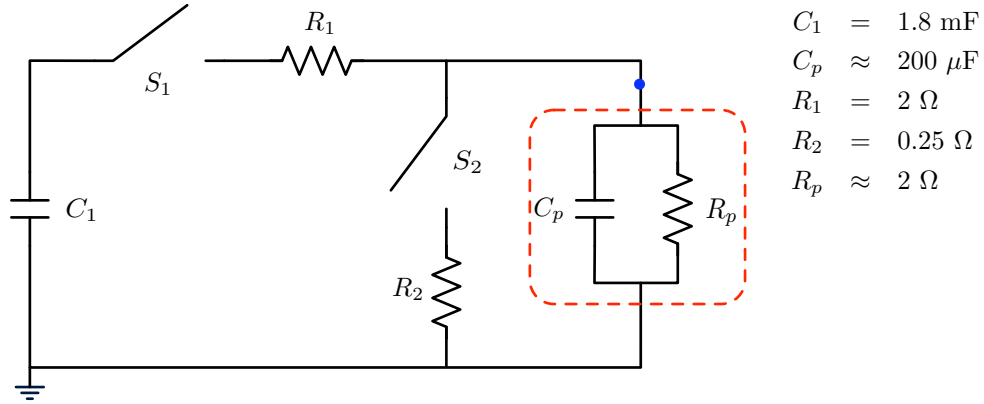


Figure 4.1: An MCX discharge can be modeled as the electric circuit shown here. The plasma voltage, V_p , and plasma current, I_p , are measured at the location indicated by the blue dot. The capacitor C_1 represents the capacitor bank. The resistors R_1 and R_2 are the series and crowbar resistors, respectively. Switches S_1 and S_2 are mercury ignitron switches. The plasma is modeled as a resistor and capacitor in parallel, shown inside the red dashed box.

digital pulse generator which is used as a synchronization device for the start ignitron, crowbar ignitron, and the CCD camera employed by the visible spectrometer.

MCX 0-dimensional discharge behavior can be described by a simple electric circuit model, shown in Fig. 4.1. Illustrated in the figure is the capacitor bank (C_1), the start ignitron switch (S_1), series resistor (R_1), crowbar ignitron switch and resistor (S_2 and R_2), and plasma capacitance and resistance (C_p and R_p , encompassed by the red dashed line). Plasma voltage, V_p , and current, I_p , are measured at the location indicated by the blue dot.

An MCX discharge commences as follows. The data acquisition system begins sampling at $t = 0$; at $t = 0.5 \text{ ms}$ the start ignitron closes (switch S_1 in Fig. 4.1), applying the full capacitor bank voltage between the center cathode and the vacuum chamber (across the pre-fill hydrogen gas). Depending on pre-fill gas pressure, applied bank voltage, and applied magnetic field, a period of voltage hold-off occurs after which the experiment enters a break-down stage in which the gas begins ionizing. Following this breakdown stage is a formation/spin-up stage in which the plasma's

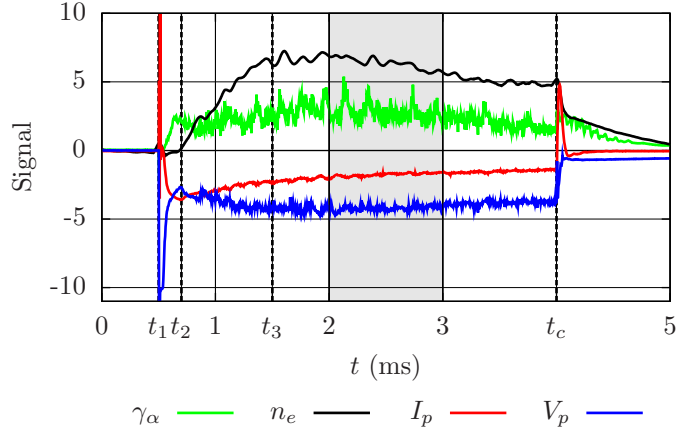


Figure 4.2: Shown are the following signals: plasma voltage (kV), plasma current (kA), plasma density (10^{14} cm^{-3}), and H_α emissivity ($10^{18} \text{ ph. cm}^{-2} \text{ s}^{-1}$). Also indicated is the start time, t_1 , the end of the breakdown phase, t_2 , the end of the formation/spin-up phase, t_3 , the crowbar time, t_c , and a quasi-steady-state period (shaded), $2 \text{ ms} < t < 3 \text{ ms}$. The shaded region is the period over which data is analyzed for this dissertation.

azimuthal momentum and density increases. Next is a near steady-state stage, after which the crowbar ignitron is closed (switch S_2), creating a type of shunt for the remaining charge on the capacitor bank as well as for the stored energy in the plasma. More detailed descriptions of both the discharge stages and the MCX circuit model, particularly in regard to post-crowbar analysis, are given by Sarah Messer [7] and Robert Lunsford [24].

Figure 4.2 shows a typical MCX discharge (MCX080929-41) illustrating the aforementioned stages of the discharge. The shaded region $2 \text{ ms} \leq t \leq 3 \text{ ms}$ is the time period of interest for a majority of the analysis presented in this dissertation. signals for plasma voltage and current, electron density, and H_α emissivity are plotted. Indicated by vertical dashed lines are the following times of interest: t_1 is the closing of the start ignitron (switch S_1 , Fig. 4.1); $t_1 < t < t_2$ is the breakdown stage; $t_2 < t < t_3$ is the formation/spin-up stage; $t_3 < t < t_c$ is a quasi-steady state stage; t_c is the closing of the crowbar ignitron (switch S_2 , Fig. 4.1).

The three main diagnostics of interest to this work are the infrared interferometer, visible spectrometer, and a multi-chord array of H_α emission detectors (HEDs). All are situated at the mid-plane ($z \simeq 0$) of the MCX device. The interferometer is a Mach-Zehnder type using a $3.39 \mu\text{m}$ HeNe laser [37]. It is situated at the lower tangential port with an impact parameter of 16.5 cm. The spectrometer is a 1 meter Czerny-Turner type with a 600 groove/mm grating. The detector used for the spectrometer is an intensified CCD camera with a $528 \text{ px} \times 748 \text{ px}$ CCD chip. The spectrometer achieves a five chord capability by using a five-chord fiber bundle. The fibers are arranged vertically in the bundle and the resulting image on the CCD chip is along the vertical (528 px) dimension. The spectral view of the CCD camera is about 13 nm having an approximate inverse dispersion of $0.17/\text{px}$ and centered at approximately 656.28 nm (H_α). The instrument width of the spectrometer is no larger than 3 px. The spectrometer employs the same type of collection optic assemblies and optical fibers as the HED array.

The multi-chord H_α emission detector array (see Chapter 3) is composed of 16 HED systems arranged at the mid-plane with different impact parameters. In order to fit 21 collection optics (16 HED and 5 spectrometer) at the top tangential port, two vertical rows of 8 collection optics were arranged for the HEDs and a third row of five for the spectrometer. One row is located at $z = 3.5 \text{ cm}$ containing odd numbered HEDs, another row is located at $z = -1.5 \text{ cm}$ containing even numbered HEDs. The z location of each row is listed in Table-4.1 along with each chords impact parameter and angle of incidence with respect to the viewport. The z location of each row and the vertical spacing within each row were arranged in such a way that the outer-most HED and spectrometer chords as well as the inner-most HED chords were not “clipped” by the edges of the 8” viewport ($\approx 150 \text{ mm}$ diameter opening).

There are four primary goals intended to be achieved with H_α profile measurements:

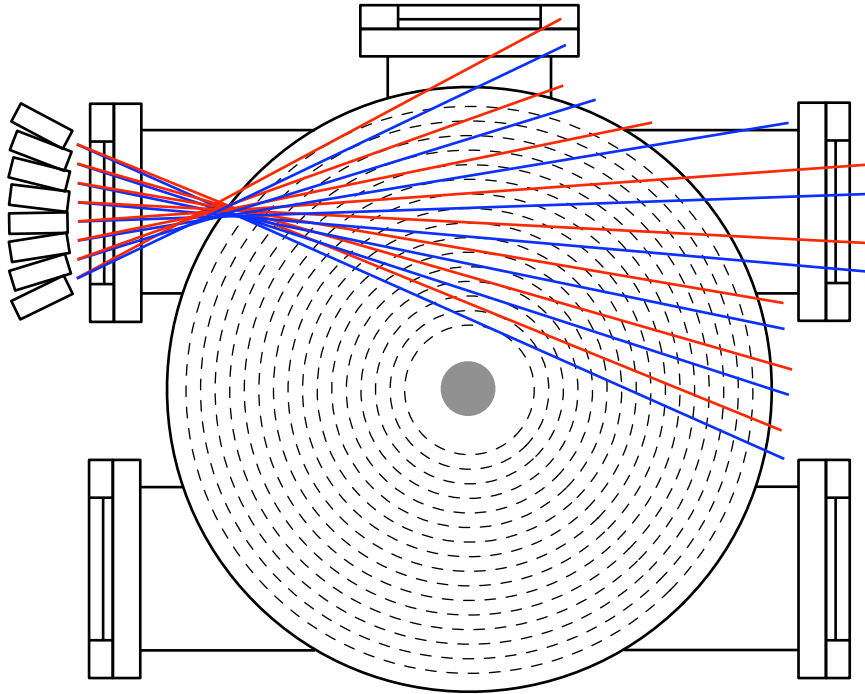


Figure 4.3: Shown is a cross-section of the vacuum vessel at the mid-plane ($z = 0$) depicting the locations of each HED in the multi-chord arrangement. 16 chords are arranged in two vertical columns of 8 chords each. One column contains odd-numbered HEDs (blue) and the other contains even-numbered HEDs (red). The columns are separated by 5 cm and the radial resolution is 1.4 cm. The angle of incidence with respect the viewport for each chord is listed in Table-4.1.

Table 4.1: HED Chord Locations.

#	r (cm)	z (cm)	θ ($^\circ$)	#	r (cm)	z (cm)	θ ($^\circ$)
3	6.0	3.5	22.0	11	16.8	3.5	3.1
4	7.4	-1.5	20.4	12	18.2	-1.5	4.9
5	8.7	3.5	16.2	13	19.5	3.5	10.1
6	10.1	-1.5	14.5	14	20.9	-1.5	12.0
7	11.4	3.5	9.9	15	22.2	3.5	17.4
8	12.8	-1.5	8.2	16	23.6	-1.5	19.5
9	14.1	3.5	3.5	17	24.9	3.5	25.0
10	15.5	-1.5	1.7	18	26.3	-1.5	27.2

1. Obtain confirmation of the plasma width, a , between the inner and outer-most flux surfaces. Figure 2.7(a) suggests that the emissivity may fall to zero outside the locations of the inner and outer-most magnetic flux surfaces, where plasma density may be zero.
2. Compare H_α intensity measurements with those predicted by both the NMG and NMGC models.
3. Compare the scaling of neutral density, estimated from H_α measurements, with that prescribed by the NMG and NMGC models.
4. Compare the scaling of the charge-exchange time, estimated from H_α measurements, with measurements of the momentum confinement time.

To accomplish the goals listed above, an experimental campaign was undertaken in which four input parameters were varied. The varied parameters were the mirror ratio, \mathcal{R} , the mid-plane magnetic field, B_{mid} , the fill pressure, P_{fill} , and the applied capacitor bank voltage, V_{bank} . By varying the mirror ratio we expect to see a change in the plasma width or changes in the location of the inner and outer-most flux surfaces. From Eqs. (2.16) & (2.17), we expect to see variational dependence of the neutral density on magnetic field and plasma density. Fill pressure provides the necessary variation in plasma density. It is less clear what is to be expected by varying the applied bank voltage. Typically, larger capacitor bank voltages do not result in larger voltages across the plasma (or larger rotation velocities), but rather in reduced plasma resistance and larger plasma current. This may indicate increased plasma temperature¹, but we do not currently have reliable diagnostics dedicated to measuring electron and ion temperatures. Nevertheless, variations in applied bank voltage are included in the experiment.

¹Increased plasma current may be inconsistent with increased plasma temperatures, since increased temperatures should improve plasma performance.

Table 4.2: Applied Experimental Conditions.

set	B_{mid} (T)	\mathcal{R}	V_{bank} (kV)	P_{fill} (mTorr)
1	0.15, 0.18, 0.21, 0.24	6	10	5
2	0.21	4, 5, 7	10	5
3	0.21	6	8, 9, 11, 12	5
4	0.21	6	10	1, 9
5	0.3	5.1	10	5

Table-4.2 lists the experimental parameters for the experiment. Each parameter was varied while keeping all other parameters fixed. It is not intended to completely fill the parameter space, but only to observe the scaling of the measurements as a single input is varied. There is one exception which is due to the constraints of the power supplies driving the magnetic field (listed as set 5). It was desirable to extend the magnetic field as high as possible (0.3 Tesla), limited only by the solenoid coils' power supply; however, the mirror coils' power supply limits the mirror ratio to 5.1 for mid-plane field magnitude of 0.3 T.

The data presented in this chapter represents an average over the quasi-steady state period $2 \text{ ms} < t < 3 \text{ ms}$, unless stated otherwise. Analysis procedures specific to particular results are described in detail as the results are presented.

4.2 Radial Profiles in MCX Discharges

The purpose of developing a multi-chord detector system is to obtain radial profile information. Here we present measured H_{α} emissivity profiles and compare them to the two theoretical models described in Sec. 2.4. The profile measurements indicate that emissivity (and neutrals) are dominant near the wall of the vacuum chamber, that there is no indication of inner and outer-most flux surfaces (and hence no information about the plasma width), and that the profile shapes are largely independent of the plasma conditions produced within currently available MCX parameters.

All radial H_α profile information presented in this work has been conditioned using a data smoothing routine in order to reduce the effect of observed systematic error. HED measurements, prior to Abel inversion, indicated spatial fluctuations in H_α emissivity on the scale of the chord separation (1.4 cm) and which appeared to be invariant to parametric variations. This is shown as the green triangles in Fig. 4.4(a). These are raw chord integrated measurements. The reader may observe spatial oscillations particularly for radii between about 10 and 15 cm, as well as between about 19 and 23 cm. Because this pattern is on the scale of the chord separation and persists throughout the parametric scans, it was determined to be systematic. After the main experimental campaign, the multi-chord arrangement was re-situated such that the z locations of both vertical rows were closer together (3 cm separation). This resulted in a smoother profile, further supporting the conclusion that the spatial fluctuations were systematic. The most likely explanation is that reflection properties of the vacuum chamber wall differ significantly enough from one location to another as to produce this effect. Recall that the reflectance test performed on the vacuum vessel wall was only done for one chord location (see Sec. 3.2).

To suppress this systematic error in the chord integrated measurements, a spatial filter was applied to the data as part of the analysis routine. The algorithm used was Matlab's `filtfilt` function, using a three element window, i.e. `<new profile>=filtfilt([1,1,1]/3,1,<old profile>)`. This has the effect of smoothing the profile information but does not affect the value of the endpoints (chords 3 & 18).

Figure 4.4 shows the H_α emissivity profile for standard experimental parameters ($B_{\text{mid}} = 0.21$ T, $\mathcal{R} = 6$, $V_B = 10$ kV, $P_{\text{fill}} = 5$ mTorr). Figure 4.4(a) shows the chord integrated signals (uninverted measurements of the HEDs). The green triangles are the raw measurements, the blue squares are the measurements after applying the spatial filter to suppress systematic error. The solid red curve is a fourth-order poly-

nomial fit constrained to be symmetric about $r = 0$ and terminated at the vacuum chamber wall. Figure 4.4(b) shows the emissivity profile (the Abel inversion of the chord integrated signals). Notice that the smoothing of the chord integrated profile has a large effect on the condition of the inverted data, where it is seen that the systematic spatial variations are exacerbated. Also notice that the emissivity profiles resulting from both the smoothed chord data and the polynomial approximation fall below zero around $r = 12$ cm. This unphysical result is an indication of systematic error most likely due to the persistence of wall reflection effects. In Appendix C.2 we show that the Abel inversion process limits the effect of systematic mis-measurement of a single chord to the nearest inward chord. Thus, it is unlikely that the negative emissivities are due to the systematic mis-measurement of a single chord. Nevertheless, the error is smaller than the emissivity amplitude near the chamber wall and therefore does not significantly affect the qualitative interpretation of the profiles. We will estimate the systematic error to be about 5×10^{16} ph. cm⁻³ s⁻¹ for inverted profiles, which will be reflected in the error bars of profile data presented henceforth.

The first observation to note from Fig. 4.4 is that there is no apparent hollow emissivity profile, unlike that which was predicted by the NMG model. Second, is that the emissivity is dominant near the vacuum chamber wall ($\simeq 27$ cm) and not immediately inside the expected positions of either the inner-most or outer-most magnetic flux surfaces (indicated by vertical dashed lines). This motivates the use of the NMGC model as a comparison, which is shown as the blue curves. These were obtained by using the plasma density (measured by the interferometer, $n_0 = 6.4 \times 10^{14}$ cm⁻³), assuming $T_e = 2.5$ eV and $T_i = 30$ eV, and shifting the inner and outer-most flux surfaces outward by 2.5 cm. Using the standard temperatures of 3.3 eV and 15 eV, respectively, results in a peak emissivity level that is about $3\times$ smaller. Shifting the flux surfaces was done in order that the model results would coincide better with the measurements. It should be mentioned, however, that the

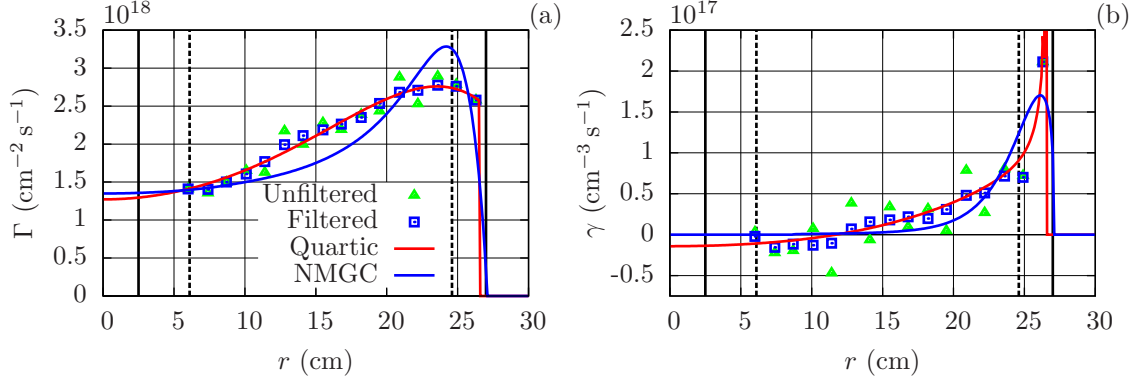


Figure 4.4: Shown are chord integrated signals from the HED multi-chord array for a standard discharge (MCX080929-41) (a), and the Abel inversion of those signals resulting in an emissivity profile (b). The raw data is given as green triangles and smoothed data as blue squares. The red curve represents a fourth-order polynomial fit to the raw data (b) and its Abel inversion (a). The blue curves are the result of the NMGC model using plasma conditions from the discharge and assuming $T_e = 2.5$ eV and $T_i = 30$ eV. Vertical dashed lines indicate the location of the expected inner and outer-most magnetic flux surfaces. Vertical solid lines indicate the location of the cathode and vacuum chamber wall.

conditions applied here to the NMGC model resulted in $N_{\text{wall}} \simeq 1.2 \times 10^{14} \text{ cm}^{-3}$, a maximum ionization fraction of about 99% (which occurs at $r = 15$ cm), and an average ionization fraction of 95% over the assumed plasma width.

We should also mention here that the profiles observed are qualitatively much different than those previously observed by Ghosh [11] in two ways. First, Ghosh observed mildly hollow profiles for neutral hydrogen emissivity. Second, he observed an emissivity level at 6 cm which was about $10\times$ the emissivity at 25 cm. The reason for this change from inboard dominated to outboard dominated emissivity is not known. However, it is possible that changes to end insulators and/or surface conditioning of the vacuum chamber could have affected this change. No hypothesis can be formulated at this time as to how the end insulator may have contributed to the change in emissivity pattern. Many years of MCX discharges without baking or discharge cleaning the vacuum chamber may have contaminated the chamber wall with large amounts of hydrogen, thus it may be sourcing large amounts of neutral particles dur-

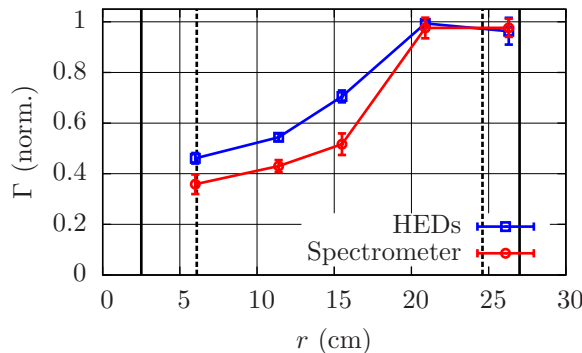


Figure 4.5: Shown are normalized, chord-integrated signals from five HEDs (MCX081006-01...05) and the spectrometer (MCX081006-17...21). The profile obtained from the spectrometer corroborates the results of the HED multi-chord array.

ing discharges. Efforts are currently underway to implement baking and discharge cleaning in order to determine if this is plausible.

For the purpose of checking the qualitative results of the emissivity profile, several discharges were executed in which five HED view chords, distributed between 6 cm and 26 cm, were given to the spectrometer. The spectra taken were then integrated over the interval $655.2 \text{ nm} < \lambda < 657.4 \text{ nm}$ to include the entire H_α emission line. The five point spatial profiles for each discharge are normalized by the maximum intensity chord and then individual chords are averaged over the discharges. Figure 4.5 shows the comparison between the ensemble averaged profile as measured by the HED array (discharges MCX081006-01...05) and that of the spectrometer (discharges MCX081006-17...21). The error bars indicate the standard deviations from the mean. Keep in mind that we do not have a relative calibration between the spectrometer chords so the profiles cannot match exactly. Nevertheless, the qualitative agreement between the two indicates that the profiles measured by the HED array are correct.

Neutral density and charge-exchange time will be discussed in Sec. 4.4, but for reference purposes the emissivity data in Fig. 4.4(b) is converted to neutral density and charge-exchange time estimates as a function of radius and shown in Fig. 4.6.

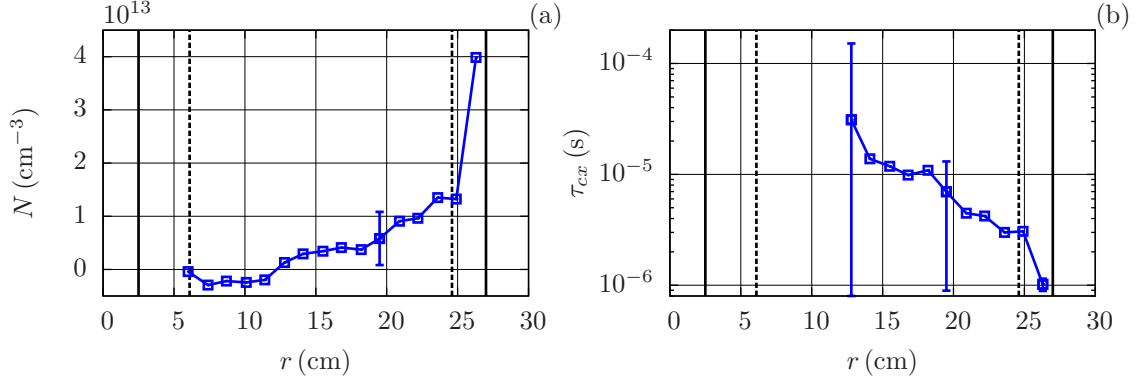


Figure 4.6: Shown is a neutral density profile (a) and charge-exchange time profile (b) as a function of radius under standard discharge conditions. The neutral density is estimated from the emissivity data in Fig. 4.4(b) and τ_{cx} from the neutral density ($1/N\alpha_{cx}$). A few selected error bars are shown for the charge-exchange plot in order to show the increasing uncertainty for decreasing radius due to $N \rightarrow 0$.

Neutral density is estimated using Eq. (2.12) with the assumptions that $n(r) = n$ (uniform plasma density) and $T_e = 3.3 \text{ eV}$. The charge-exchange time is calculated as $\tau_{cx} = 1/N\alpha_{cx}$ with $T_i = 15 \text{ eV}$ assumed. The selected error bars in the charge-exchange plot indicate increasing uncertainty for smaller radii owing to $N \rightarrow 0$. In addition, τ_{cx} for $r < 12 \text{ cm}$ is omitted since the data is less than zero. Nevertheless, if the emissivity data is to be interpreted as neutral density approaching zero, then the charge-exchange time may become much larger for radii less than 12 cm.

Since the neutral density profile in Fig. 4.6(a) is determined with the assumption of a flat electron temperature profile, it is appropriate to mention the possible effect that a temperature gradient near the chamber wall will have on estimated neutral density near the wall. From Fig. 2.4 we saw that the interpretation of neutral density from H_α emissivity is very sensitive to electron temperature. For example, for fixed electron density, the neutral density is about 1 order of magnitude larger at $T_e = 2 \text{ eV}$ than at $T_e = 3.3 \text{ eV}$, for a given emissivity. Similarly, the neutral density is about 3 orders of magnitude larger for $T_e = 1 \text{ eV}$. Thus, several of the outer-most data points in Fig. 4.6(a) could be an order of magnitude larger. However, it is unlikely that

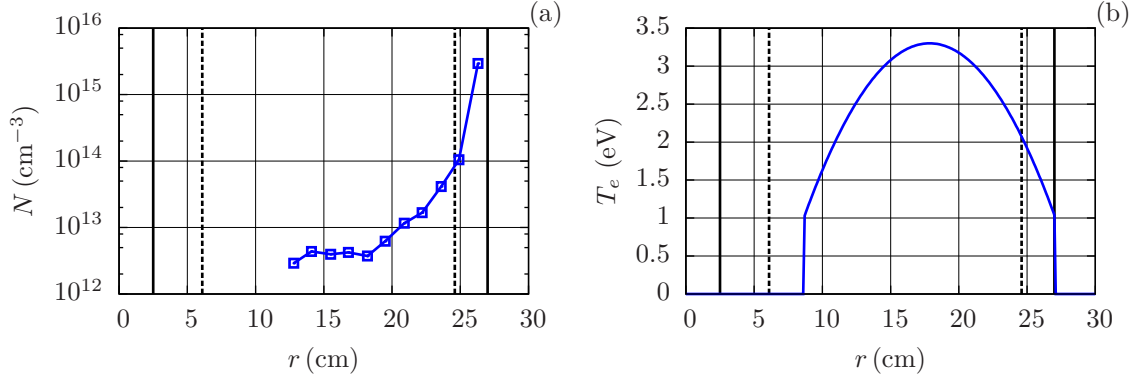


Figure 4.7: Shown is a neutral density profile (a) resulting from the assumed parabolic electron temperature profile (b) and the H_α emissivity data in Fig. 4.4(b). The vertical black lines indicate the inner cathode and vacuum chamber wall. The vertical dashed lines indicate the location of the expected inner and outer-most flux surfaces.

neutral density at the chamber wall (outer-most data point) could be larger than the pre-fill atomic density of about $3 \times 10^{14} \text{ cm}^{-3}$.

Figure 4.7 shows a resulting neutral density profile if a parabolic temperature profile is assumed. Here the maximum electron temperature is 3.3 eV and the temperature reduces to 1 eV at the plasma boundaries. The plasma boundaries are shifted outward by about 2 cm from their expected positions.

It was found that varied experimental parameters had little effect on the relative emissivity profile, except at the outer-most chord. The *absolute* amplitude of the emissivity profiles do change considerably with experimental parameters, which will be discussed in Sec. 4.4. The relative emissivity profiles are shown in Fig. 4.8. These were obtained using the same procedure described earlier, except that here the profiles are normalized by the emissivity value at $r = 21 \text{ cm}$. As before, the vertical dashed lines indicate the expected inner and outer-most flux surfaces.

4.3 MCX Discharge Phenomenology

In this section we report the results of absolute H_α emissivity and neutral density estimates with variations in experimental parameters. There are four figures in this

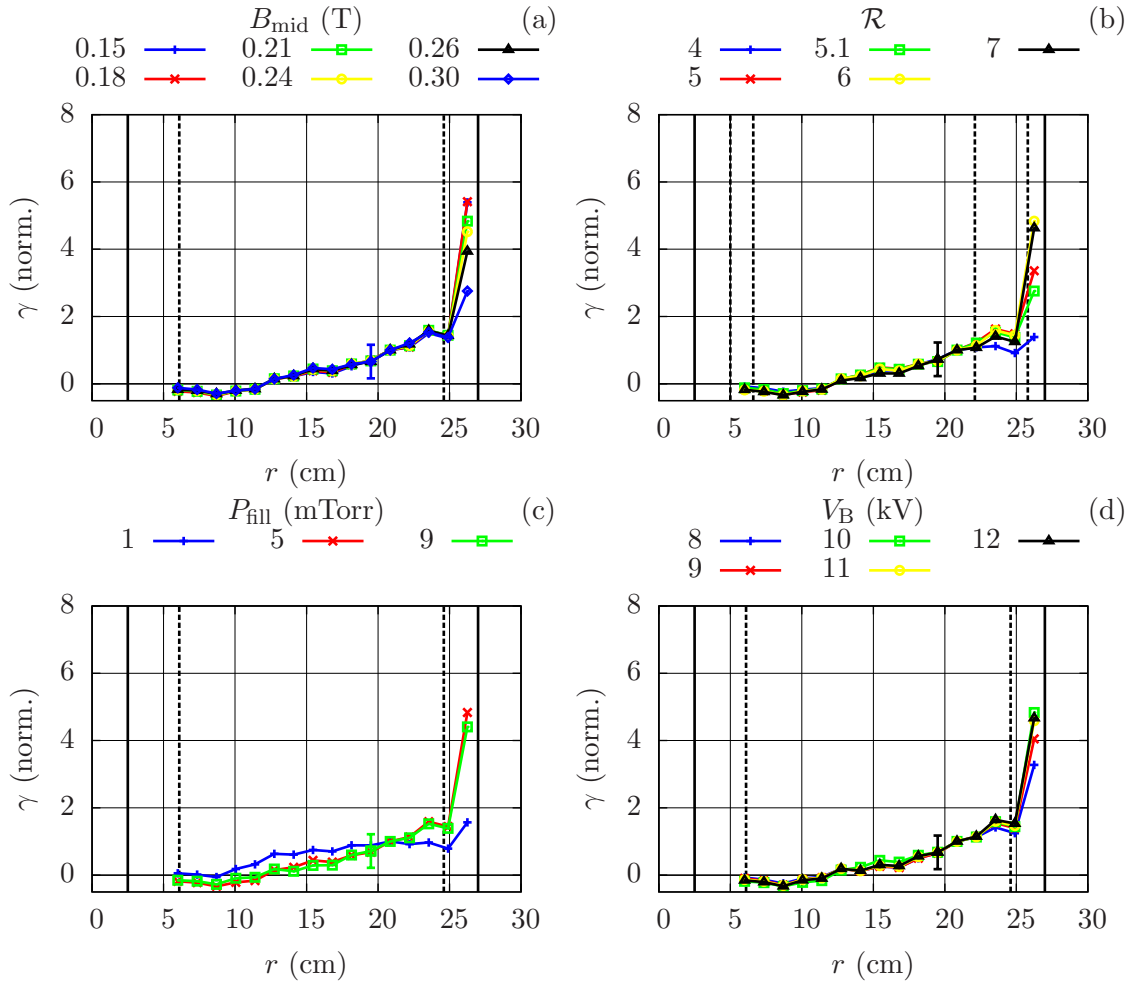


Figure 4.8: Shown are relative emissivity profiles for different applied magnetic field (a), mirror ratio (b), fill pressure (c), and capacitor bank voltage (d). Each profile is an average of about 10 discharges under the same experimental parameters. Each ensemble averaged profile is normalized by its emissivity value at $r = 20.9$ cm.

section, each presenting the results from the variation of a single experimental parameter (magnetic field, fill pressure, mirror ratio, or capacitor bank voltage). Each figure contains six plots: (a) H_α emissivity, γ , “inside” the plasma and at the vacuum chamber wall; (b) neutral density estimates at these same locations; (c) Alfvén Mach number; (d) electron density; (e) average plasma rotation velocity, $\langle u_\phi \rangle$; (f) momentum confinement time. Each datum presented forthwith represents an average value over the time interval $2 \text{ ms} < t < 3 \text{ ms}$ for a single discharge. Following each figure are discussions of phenomenological behavior contained therein.

The neutral densities were calculated using Eqs. (2.12), assuming $T_e = 3.3 \text{ eV}$ [11], and assuming a flat plasma density profile, i.e. $n(r) = n_e$ where n_e is determined by the interferometer. The Alfvén Mach number, M_A , was included in the analysis because a perturbed outer-most flux surface may help explain the large emissivity activity at the vacuum chamber wall (see Sec. (4.2)). M_A is calculated as $\langle u_\phi \rangle / v_A$ where $\langle u_\phi \rangle \cong V_p / a B_{\text{mid}}$ and $v_A = B_{\text{mid}} / \sqrt{4\pi n_e m_i}$. The plasma width, a , is taken to be the distance between the unperturbed inner and outer-most flux surfaces, as calculated by a magnetic field line map, and is only a function of mirror ratio, \mathcal{R} . The momentum confinement time is calculated as the RC time of the plasma [37] given by

$$\tau_M = \frac{1}{2} \frac{L}{\ln(r_2/r_1)} \frac{V_p}{I_p} \left(1 + 4\pi m_i c^2 \frac{n_e}{B_{\text{mid}}^2} \right). \quad (4.1)$$

Here, r_1 and r_2 are the presumed radii of the inner and outer-most flux surfaces, respectively, and $L = 130 \text{ cm}$ is the approximate plasma scale size in the z (axial) direction.

Figure 4.9 shows the results for a magnetic field variation $0.15 \text{ T} \leq B_{\text{mid}} \leq 0.30 \text{ T}$. The applied capacitor bank voltage was 10 kV , fill pressure was 5 mTorr , and mirror ratio was 6 for all discharges with the exception that the mirror ratio was 5.1 for discharges at which $B_{\text{mid}} = 0.30 \text{ T}$ (see Table 4.2). We make the following observations.

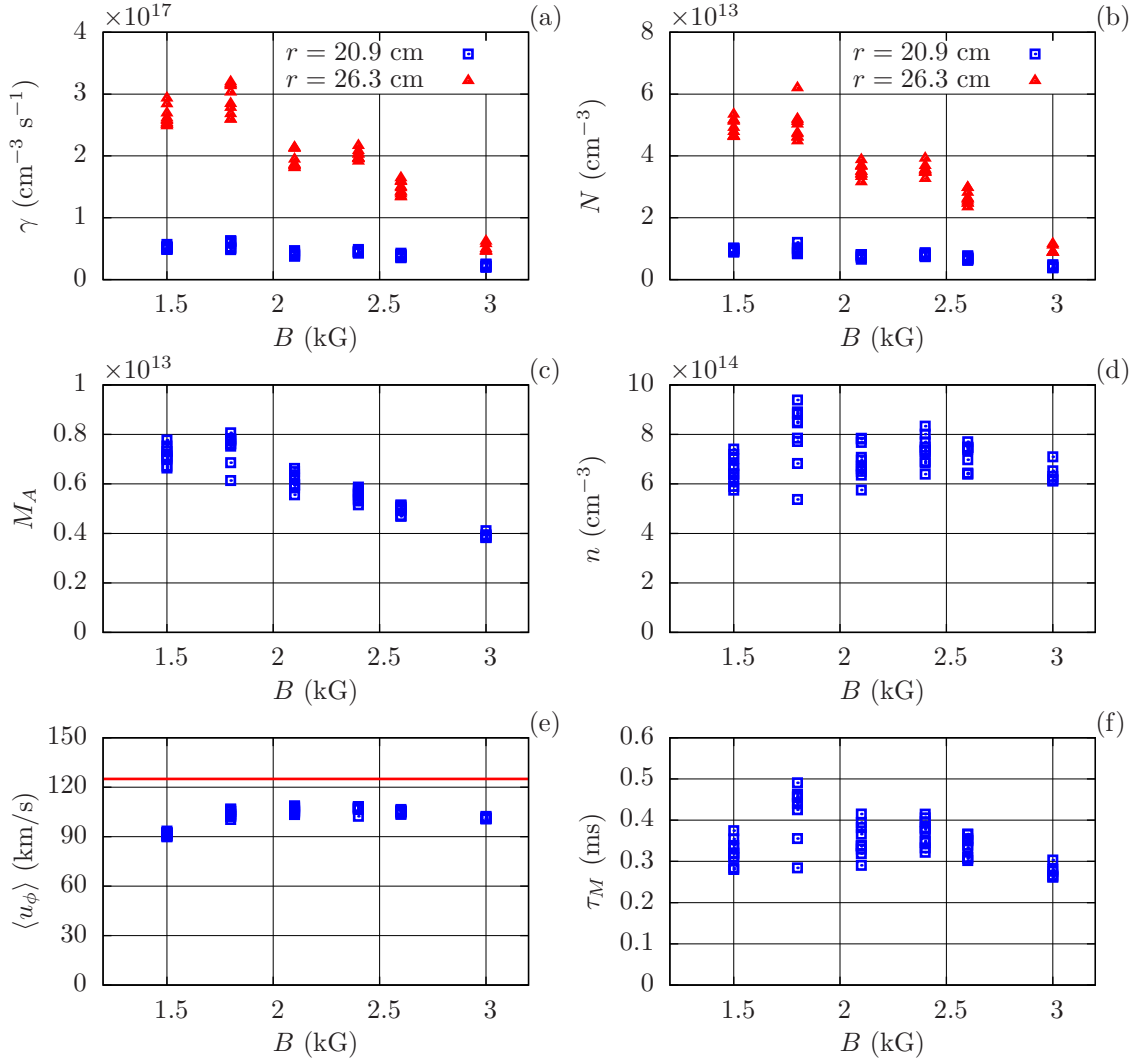


Figure 4.9: Shown versus mid-plane applied magnetic field is the H α emissivity at the wall and inside the outer-most flux surface (a), the neutral density at those same locations (b), the Alfvén Mach number (c), electron density (d), average plasma rotation velocity with CIV reference curve (e), and momentum confinement time (f). The Critical Ionization Velocity is shown for reference (red curve) (e). (Discharges MCX080929-11...61, MCX080930-44...50.)

- Both the emissivity at the wall and emissivity from within the plasma decrease with increasing magnetic field. The emissivity at the wall drops more rapidly than does the emissivity interior to the plasma.
- The neutral density estimates at the wall and interior to the plasma appear to decrease with increasing magnetic field. This is discussed in more detail in Sec. (4.4).
- M_A is near 1 for low values of B_{mid} and decreases nearly linearly between 0.18 T and 3 T.
- The plasma density remains fairly constant.
- $\langle u_\phi \rangle$ increases slightly for $0.15 \text{ T} < B_{\text{mid}} < 0.18 \text{ T}$, but remains constant for $B_{\text{mid}} > 0.18 \text{ T}$.

One would expect cross-field transport to decrease with increasing magnetic field, thus the decreasing emissivity (and neutral density) is qualitatively consistent with an expected enhanced particle confinement. However, the apparent reduction in neutral density does not accompany an increase in plasma density. Since the plasma density calculation assumes a uniform density profile, it is possible that the decreasing emissivity at the wall is primarily the result of decreasing plasma density and temperature at the wall only, while leaving the average phase shift of the interferometer largely unaffected. This may imply, however, that the drop in neutral density at the wall is inaccurate. For example, if the plasma density at the wall is $3 \times 10^{14} \text{ cm}^{-3}$, less than about half the nominal value, and the electron temperature drops to 2.5 eV, the emissivity at the wall would drop to its observed value at 0.3 T while the neutral density at the wall would remain unchanged at about $4 \times 10^{13} \text{ cm}^{-3}$. This would be consistent with a slight recession of the plasma away from the vacuum chamber wall due to improved particle confinement, while the interior density profile remains largely unaffected.

The high Alfvén mach number may explain the existence of high emissivity at the wall. Since $M_A \sim 1$, we can have no expectation that the inner and outer-most flux surfaces are unchanged for these discharges. It is unclear what role high Alfvén Mach number may play in the intrinsic confinement quality of the plasma. However, for large M_A magnetic field lines will be perturbed from their vacuum positions (the centrifugal pressure is comparable to the magnetic pressure), so it is plausible that centrifugal forces push magnetic field lines (along with the plasma) into the vacuum chamber wall, enhancing the emissivity at the wall. Then, as M_A decreases, the field lines recede from the wall leading to a decrease in plasma density at the wall. The effect of large M_A is currently being investigated by members of the MCX team through the analysis of diamagnetic loops and a detailed theoretical treatment of the discharge magnetics.

Figure 4.10 shows the results of variation in fill pressure between 1 and 9 mTorr. While only three fill pressure settings were intended (1, 5, and 9), conditioning discharges were taken at the beginning of each day before the fill pressure stabilized to 5 mTorr, resulting in a broad range of fill pressures near 5 mTorr. Variations in fill pressure have a near one-to-one correspondence to variations in plasma density, so fill pressure provides good control over the plasma density. All data in Fig. (4.10) are plotted against plasma density (except Fig. (4.10)(d)), as this is more physically relevant than the fill pressure. We make the following observations.

- H_α emissivity at the wall and interior to the plasma appear to have a cubic relation to plasma density.
- Neutral density at the wall and interior to the plasma appear to have a quadratic relation to plasma density. This is discussed in more detail in Sec. (4.4).
- $M_A \sim 0.6$ for standard conditions and increases for larger fill pressures, in accordance with its \sqrt{n} dependence.

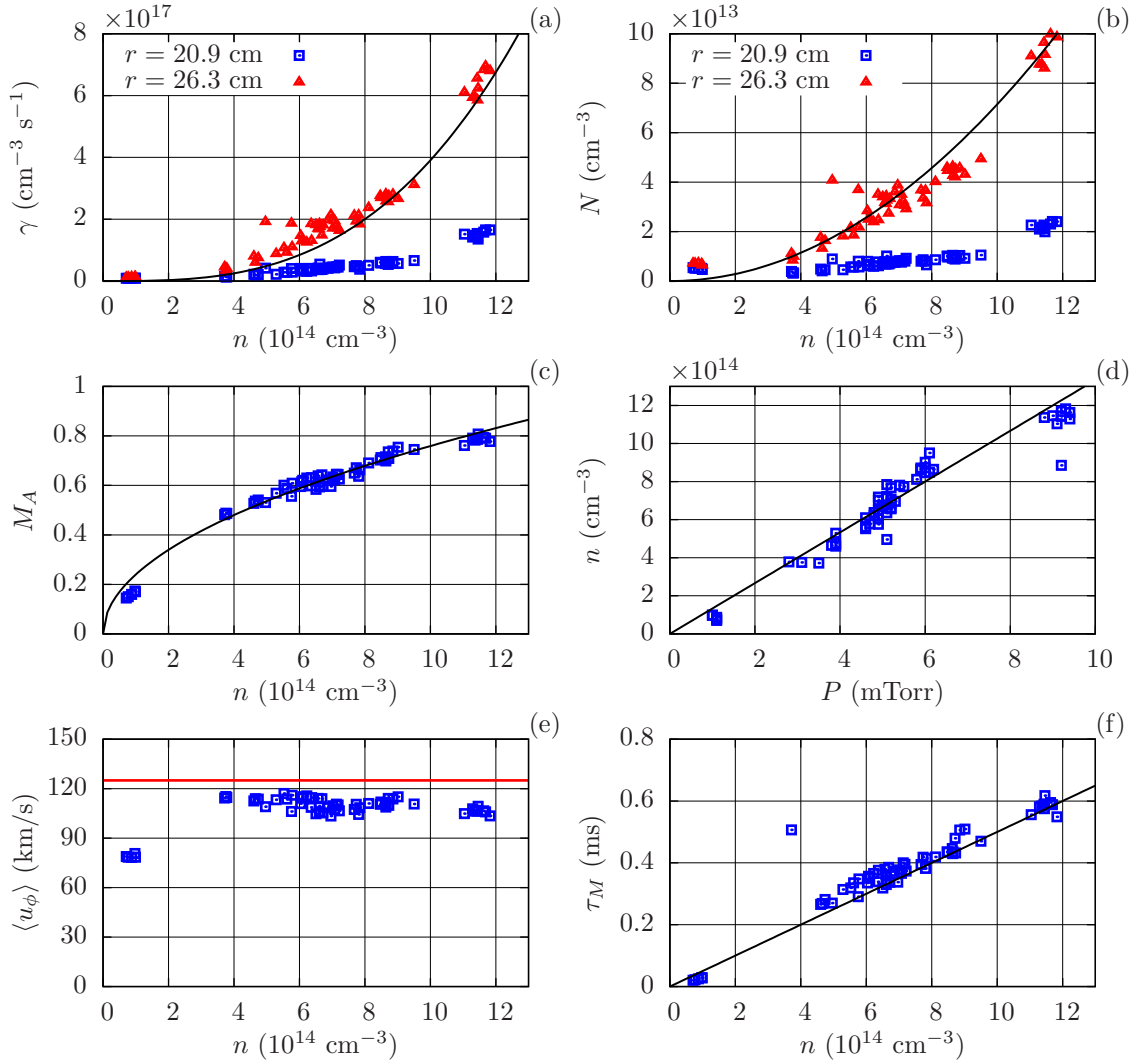


Figure 4.10: Shown versus electron density is the H_α emissivity at the wall and inside the outer-most flux surface with suggestive $\sim n^3$ curve (a), the neutral density at those same locations with a suggestive $\sim n^2$ curve (b), the Alfvén Mach number with $\sim \sqrt{n}$ curve (c), average plasma rotation velocity with CIV reference curve (e), and momentum confinement time with $\sim n$ curve (f). The electron density is plotted versus fill pressure (d) indicating a near linear relationship (black line). (Discharges MCX080929-3...10, 32...41, MCX081002-01...05, MCX081003-01...05, MCX081006-01...05, MCX081007-01...25, MCX081008-46...55.)

- $\langle u_\phi \rangle$ increases over $10^{14} \text{ cm}^{-3} < n < 4 \times 10^{14} \text{ cm}^{-3}$, but remains constant for $n > 4 \times 10^{14} \text{ cm}^{-3}$.
- The momentum confinement time increases linearly in accordance with its n dependence.

Figure 4.11 shows the results from varying the mirror ratio. Recall that the primary result from changing the mirror ratio ought to give some information about the outer-most flux surface, and possibly also the inner-most flux surface. In Fig. 4.8(b) we see no clear indication of the inner-most flux surface, and information about the outer-most flux surface is not evident except possibly that it is coincident with the vacuum chamber wall. We make the following observations.

- The plasma rotation velocity, $\langle u_\phi \rangle$, increases only slightly from $\mathcal{R} = 4$ to $\mathcal{R} = 5$, after which it appears to remain constant.
- M_A , n_e , and τ_M increase between $\mathcal{R} = 4$ and $\mathcal{R} = 6$, then decrease for $\mathcal{R} = 7$.
- H_α (and neutral density) at the wall increases only slightly from $\mathcal{R} = 4$ to $\mathcal{R} = 5$, then increases more rapidly for $\mathcal{R} > 5$.
- H_α emissivity (and neutral density) interior to the plasma does *not* increase from $\mathcal{R} = 4$ to $\mathcal{R} = 5$, in contrast to emissivity near the wall, but increases only for $\mathcal{R} > 5$.

The data here suggests a possible velocity limit which is unrelated to CIV and Alfvén velocity limits. Furthermore, the H_α emissivity information also suggests that something changes between $\mathcal{R} = 5$ and $\mathcal{R} = 6$. While it may be possible that the plasma rotation velocity is CIV limited at the insulator for $\mathcal{R} \leq 5$, this cannot explain the observed limit for higher mirror ratios. In addition, $\langle u_\phi \rangle$ is limited for $\mathcal{R} \geq 5$, while M_A is less than 1 and continues to increase until $\mathcal{R} = 6$; this suggests that the rotation velocity cannot be hitting an Alfvén velocity limit either.

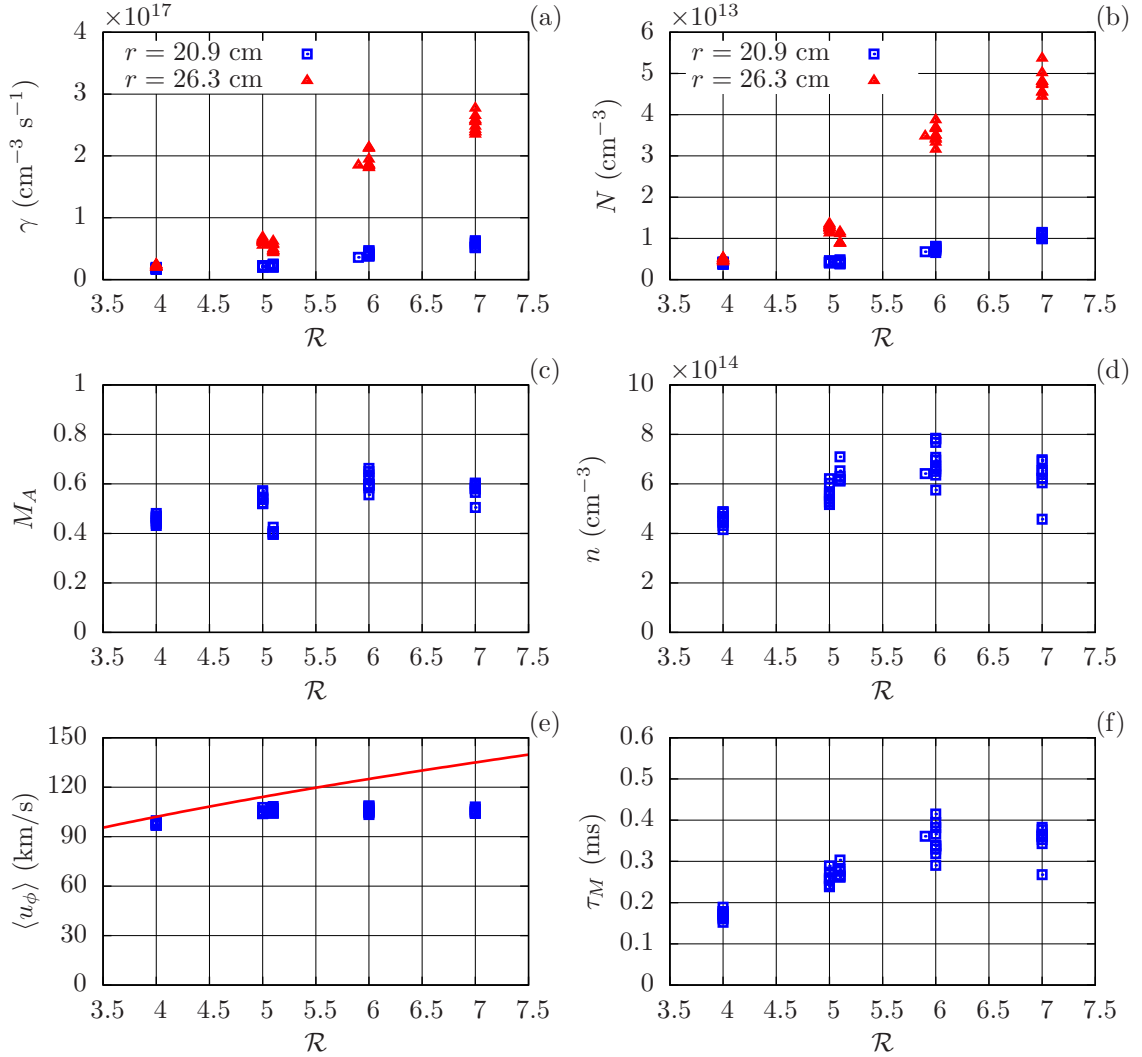


Figure 4.11: Shown versus mirror ratio is the H_α emissivity at the wall and $r = 20.9$ cm (a), the neutral density at those same locations (b), the Alfvén Mach number (c), electron density (d), average plasma rotation velocity with CIV reference curve ($\sim \sqrt{\mathcal{R}}$) (e), and momentum confinement time (f). Note that N does not increase with \mathcal{R} interior to the plasma except for $\mathcal{R} > 5$. (Discharges MCX080929-32...41, MCX080930-11...50.)

It may be that the outer-most flux surface is contacting the vacuum chamber wall for higher mirror ratios due its perturbation by the moderate Alfvén mach numbers, causing elevated emissivity as well as enhanced drag on the plasma rotation. For example, the unperturbed location of the outer-most flux surface is $\{22, 23.4, 24.6, 25.8\}$ cm for $\mathcal{R} = \{4, 5, 6, 7\}$, but an $M_A \cong 0.6$ may cause the flux surface to be displaced by ~ 2 cm,² which means that the flux surface could be coincident with the chamber wall for $\mathcal{R} \geq 6$. The magnetics of MCX discharges are currently being investigated, particularly in the context of moderate Alfvén mach numbers.

The effect of a perturbed outer-most flux surface may be enhanced by the presence of a scrape-off layer, as well. A scrape-off layer width can be calculated as $\lambda_{\text{SOL}} = \sqrt{D_{\perp} L / v_{\text{th}}}$ where D_{\perp} is the cross-field diffusion coefficient, $L = 65$ cm is a scale length to the nearest limiter, and v_{th} is the ion thermal velocity [5]. So, for example, if Bohm diffusion and $T_i = 15$ eV are used, $\lambda_{\text{SOL}} \approx 1$ cm, thus plasma may begin contacting the vacuum chamber wall at the mid-plane for mirror ratios as low as 5.

Figure 4.12 shows the results of the voltage scan. Here, quantities are plotted versus plasma current, I_p , since this is more physically relevant than applied bank voltage; also, variation in applied bank voltage more strongly affects plasma current rather than plasma voltage. We make the following observations.

- The average plasma rotation velocity, $\langle u_{\phi} \rangle$, remains nearly constant, possibly CIV limited.
- Electron density increases nearly linearly, but possibly is limited for $I_p \geq 2.5$ kA.
- The momentum confinement time remains relatively constant, but drops slightly for $I_p \geq 2.5$ kV, or possibly it is weakly linear with I_p .
- H_{α} emissivity at the wall and interior to the plasma increase with I_p but possibly is limited for $I_p \geq 2$ kA.

²Conversations with W. Young.

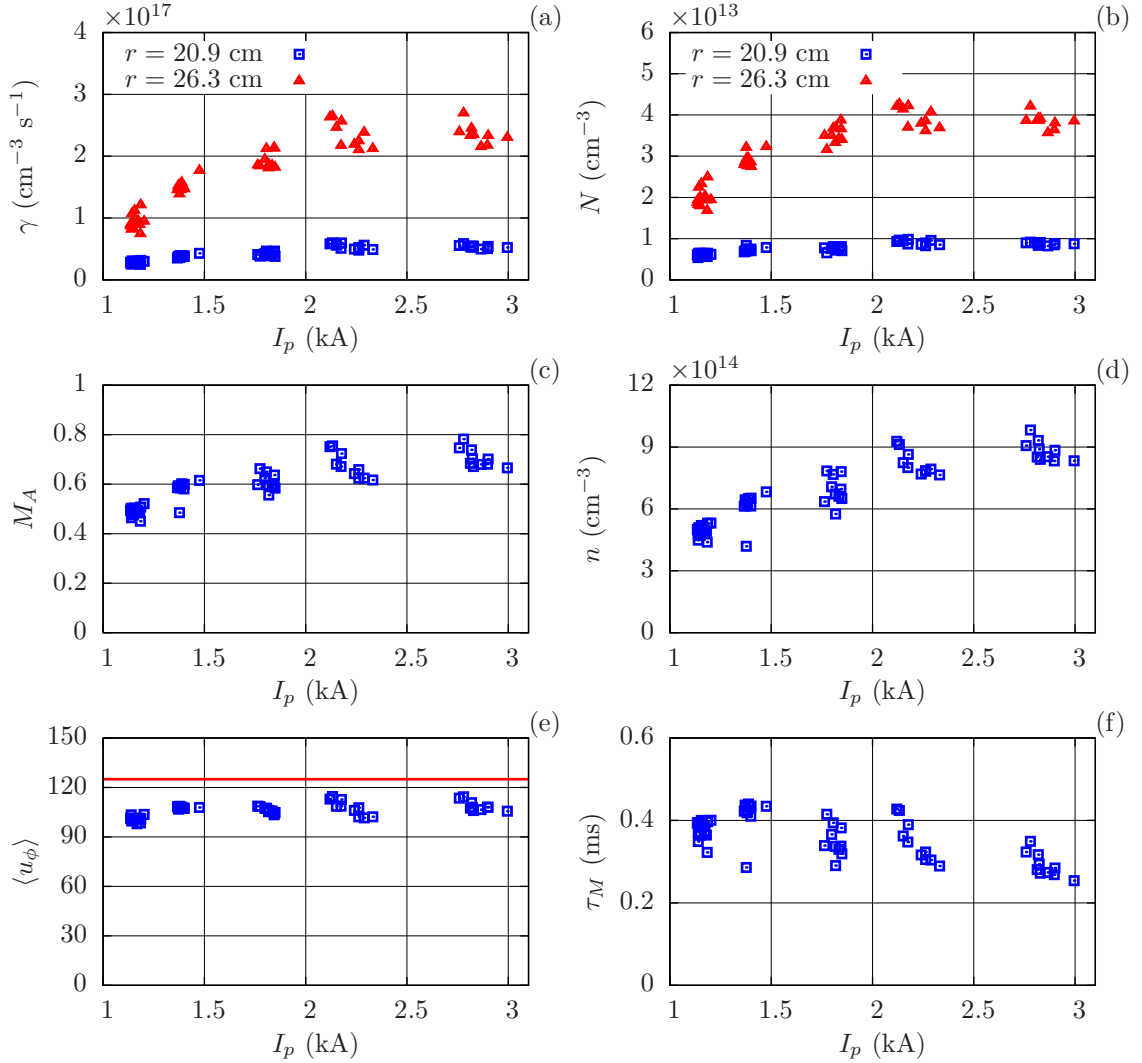


Figure 4.12: Shown versus plasma current is the H_α emissivity at the wall and $r = 20.9$ cm (a), the neutral density at those same locations (b), the Alfvén Mach number (c), electron density (d), average plasma rotation velocity with CIV reference curve (e), and momentum confinement time (f). (Discharges MCX080929-32...41, MCX081003-06...40, MCX081006-06...15.)

The possible limiting of plasma density may be a result of the finite number of particles available in the entire vacuum chamber during the discharge. Unlike the pressure scan, here the particle inventory (ions + neutrals) remains essentially fixed, thus an increase in plasma density must come at the expense of neutral density somewhere within the vacuum chamber. The expected plasma volume is approximately 1/3 that of the entire vacuum chamber, thus a plasma density of about $3\times$ the atomic density of the fill gas ($\sim 3 \times 10^{14} \text{ cm}^{-3}$ for hydrogen at 5 mTorr) may suggest a significant depletion of the ambient neutral particles. Indeed, Fig. 4.12(d) shows n_e possibly limiting near $3\times$ the atomic fill gas density. Thus it is possible that as the density increases, the neutral “blanket” density is depleted, until the neutral density at the plasma boundary is no longer determined by the ambient neutral density but dominated by wall recycling. This could explain the apparent saturation of H_α emissivity as well.

However, the above postulation is in contrast to the *increasing* estimates of neutral density shown in Fig. 4.12(b). The neutral density, though, is estimated under the assumption of fixed $T_e = 3.3 \text{ eV}$. Since the plasma voltage remains constant ($\langle u_\phi \rangle$) and the plasma current is increasing, the power into the plasma, $P_p = V_p I_p$, also increases. This increased power must be balanced by an increased power loss through all possible channels, i.e. $P_p = \sum_i \chi_i E_i / \tau_i$, where E_i is the energy contained in a channel and τ_i is the characteristic confinement time for the channel. By virtue of how the average rotation velocity ($\sim V_p$) and the momentum confinement time ($\sim nV_p/I_p$, Eq. (4.1)) are calculated, one can see that the power into the plasma rotation channel is proportional to the input power.

$$P_M = \frac{E_\phi}{\tau_M} \propto \frac{nV_p^2}{nV_p/I_p} = V_p I_p = P_p.$$

However, this does not preclude power entering other channels, such as ion and electron temperature. So, if $P_p \propto P_T \sim nT/\tau_E$ as well, it is possible that temperature is

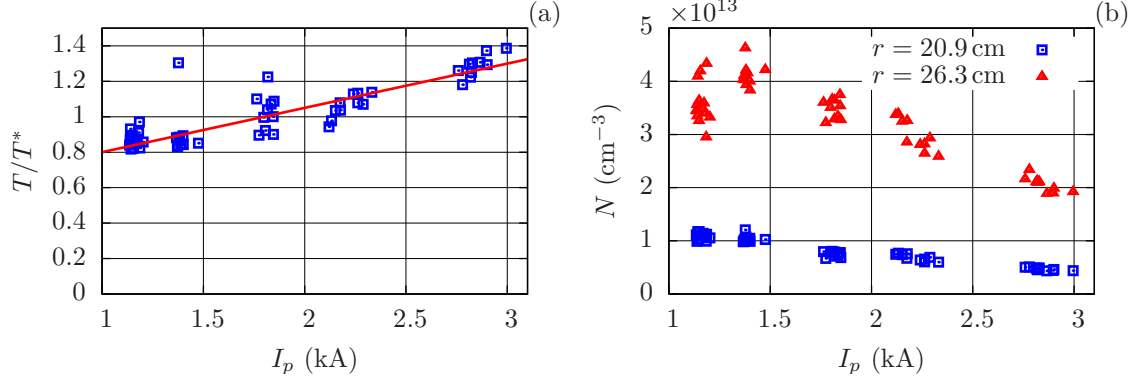


Figure 4.13: Shown is the relative change in plasma temperature (a), and the resulting estimate of neutral density at the vacuum chamber wall (b). Both are plotted versus plasma current. The change in plasma temperature is estimated from power balance and assumes that τ_E remains constant. T^* is a nominal temperature ($T_e^* = 3.3$ eV) assumed under standard discharge conditions ($I_p \simeq 1.8$ kA).

also changing with plasma current. For example, if the energy confinement time remains constant ($\simeq 50 \mu\text{s}$, assuming $T_i = 15$ eV under nominal discharge conditions), then plasma temperature may change linearly with plasma current (Fig. 4.13(a)). Using this same linear relationship for electron temperature to estimate the neutral density from the H_α emissivity shows a decreasing neutral density at the wall for increasing plasma current (Fig. 4.13(b)). This may be consistent with diminishing neutral density surrounding the plasma due to increasing plasma density.

4.4 Neutral Density & Charge-Exchange Time Scaling

In Sec. 4.2 we compared emissivity profiles with those prescribed by the models presented in Sec. 2.4. However, it still remains to be seen whether the neutral density scales appropriately with certain experimental parameters. In addition, independent of the profile form factor (determined by a specific model), the overall scaling of the estimated neutral density and the estimated charge-exchange time can still give insight as to whether neutrals are playing a major role in the behavior of MCX discharges.

In this section we present the scaling of both neutral density and the charge-exchange time.

According to the models presented earlier (2.4), the neutral density is expected to scale as

$$N \sim \frac{n_0^3}{B^2} \eta \alpha_{\text{cx}}. \quad (4.2)$$

This expression shows neutral density scaling with the cube of the plasma density, inversely with the square of the magnetic field, linear with resistivity ($\sim T_e^{-3/2}$), and linear with the charge-exchange rate coefficient ($\sim T_i^{1/3}$).

As in Sec. 4.3, the neutral density is calculated from Eq. (2.12), using $T_e = 3.3 \text{ eV}$ and $n_e(r) = n_e$. For the purpose of calculating α_{cx} we use an estimated ion temperature of 15 eV [11], thus $\alpha_{\text{cx}} \simeq 2.5 \times 10^{-8} \text{ cm}^3 \text{ s}^{-1}$ (adapted from Hutchinson, see Fig. (2.2)). We do not have any recent measurements of ion temperature or electron temperature, let alone their scaling with experimental parameters, and therefore assume that they remain constant as plasma density and magnetic field are varied. The results of neutral density scaling with plasma density and magnetic field are shown in Figs. 4.14(a) and 4.14(b), respectively.

In Fig. 4.14(a) is shown the results of neutral density scaling with plasma density. This data was obtained from the pressure scan and is the same as that shown in Fig. 4.10(b). We have plotted both the neutral density calculated at $r = 20.9 \text{ cm}$ and $r = 26.3 \text{ cm}$ (vacuum chamber wall). In order to properly show the *scaling* of neutral density, independent of absolute magnitude, the neutral density estimates determined from the emissivities are normalized to their values under nominal discharge conditions, $N^* = N(n_e = 7 \times 10^{14} \text{ cm}^{-3})$. The figure shows that neutral density scales more closely with n_0^2 than with n_0^3 , for both $r = 20.9 \text{ cm}$ and $r = 26.3 \text{ cm}$ locations. At low plasma density there is a slight relative increase in neutral density. This may be due to out-gassing from the vacuum chamber which may dominate at low fill pressures, thus providing a neutral source other than recycling (not considered by the models).

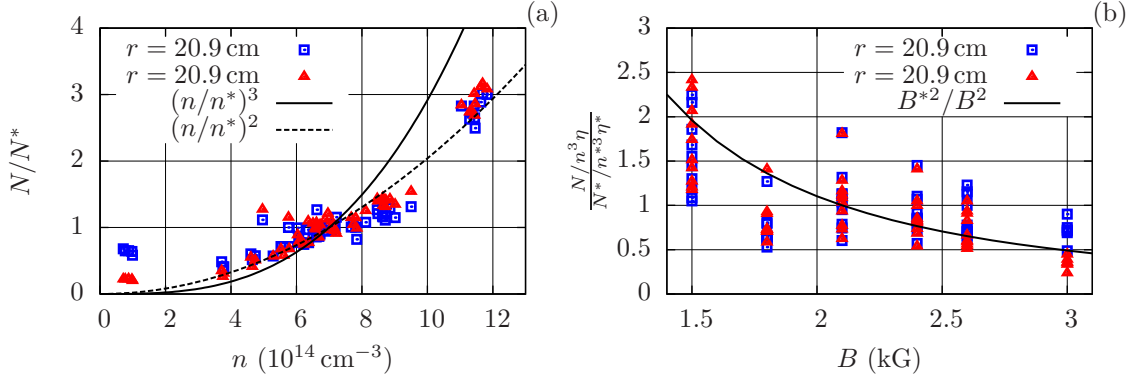


Figure 4.14: Shown is neutral density scaling with electron density (a) and with magnetic field (b). Both plots have data from $r = 20.9$ cm (blue square) and from near the vacuum chamber wall ($r = 26.3$ cm, red triangle). Overlaid are n^3 and n^2 trends (black solid and dashed curves, respectively). For plot (b), the plasma density dependence is removed ($N/n^3\eta$) in order to isolate magnetic field dependence. Overlaid is a B^{-2} trend (black curve). All datum are normalized by the value under nominal discharge conditions ($n = 7 \times 10^{14} \text{ cm}^{-3}$, $B = 2.1 \text{ kG}$).

Figure 4.14(b) shows the neutral density scaling with magnetic field. This data was obtained from the magnetic field scan (see Fig. 4.9(b)). Since the plasma density is not fixed for variation in B (see Fig. 4.9(d)) we have divided out the plasma density dependence (including η) from the neutral density, i.e. $N/n_0^3\eta$. The resulting values were then normalized by their nominal values occurring under standard discharge conditions. The figure indicates that neutral density scales consistently with B^{-2} for both radial locations. The spread in reproducibility appears large in the magnetic field scaling, nevertheless the agreement is good.

One caveat in regard to these scalings is that the scaling of electron temperature is unknown and the dependence of neutral density estimates on electron temperature is strong (see Sec. 2.3, Fig. 2.4). For the density scan, the plasma current remains relatively constant, except at the lowest densities, and changes throughout the magnetic field scan. As mentioned previously, we do not know how T_i or T_e scale with experimental parameters, but it may be reasonable to expect them to vary with plasma current. Thus, information regarding plasma temperature scaling will affect the plots shown in Fig. 4.14.

For the confinement time scaling we have plotted the charge-exchange time divided by the momentum confinement time, $\tau_{\text{cx}}/\tau_{\text{M}}$ in order to show both the relative magnitude and relative scaling with experiment parameters. The charge-exchange time is calculated for both the $r = 20.9$ cm and $r = 26.3$ cm (vacuum chamber wall) locations as $\tau_{\text{cx}} = 1/N\alpha_{\text{cx}}$ ($T_i = 15$ eV is assumed). The momentum confinement time is calculated from the plasma density, applied magnetic field, and expected radii of the inner and outer-most flux surfaces (Eq. (4.1)) and is the same data shown in Figs. 4.9–4.12(f). We make the following observations from Fig. 4.15.

1. Magnetic Field (Fig. 4.15(a))

- $\tau_{\text{cx}} \ll \tau_{\text{M}}$, by nearly a factor of 100
- τ_{cx} scales closely with τ_{M} for $B < 3$ kG

2. Mirror Ratio (Fig. 4.15(b))

- $\tau_{\text{cx}} \ll \tau_{\text{M}}$, by about a factor of 10 or more
- τ_{cx} does not scale with τ_{M} and relatively decreases with increasing \mathcal{R}

3. Plasma Density (Fig. 4.15(c))

- $\tau_{\text{cx}} \simeq \tau_{\text{M}}/3$ for low densities
- τ_{cx} does not scale with τ_{M} but decreases rapidly for increasing plasma density

4. Plasma Current (Fig. 4.15(d))

- $\tau_{\text{cx}} \ll \tau_{\text{M}}$ by at least a factor 50
- τ_{cx} scales well with τ_{M}

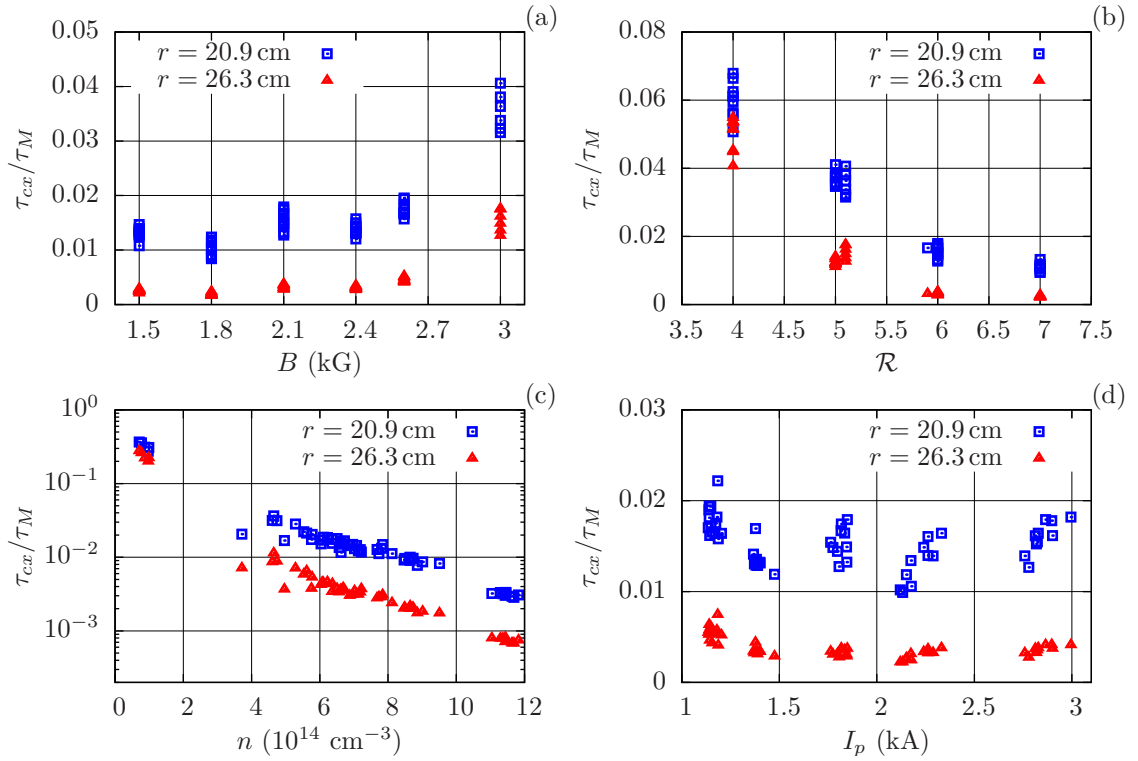


Figure 4.15: Shown is the charge-exchange times divided by the momentum confinement times for variations in applied mid-plane magnetic field (a), mirror ratio (b), electron density (c), and plasma current (d). The charge-exchange times are calculated as $\tau_{cx} = 1/N\alpha_{cx}$ using $T_i = 15$ eV.

Recall that neutral densities are estimated from H_α emissivity under the assumption of uniform plasma density and electron temperature. This is most likely not the case, particularly near the plasma edge or near the wall, where plasma density and electron temperature surely drop below their average or peak values. Since the H_α emission rate is an increasing function of electron temperature and density, the neutral density near the wall is most likely underestimated. This means that the charge-exchange times near the wall are most likely overestimated. The charge-exchange times are already too small by at least a factor of 10, so it seems that τ_{cx} near the wall cannot significantly contribute to the momentum confinement time. The charge-exchange rate coefficient, α_{cx} , is an increasing function with plasma temperature, thus decreasing plasma temperatures near the wall or plasma edge may decrease α_{cx} and increase our estimates of τ_{cx} . However, α_{cx} is a weak function of temperature ($\sim T_i^{1/3}$ [26]) while the neutral density determined from H_α emissivity is a strong function of electron temperature and density, thus it is unlikely that the plasma temperature would drop rapidly enough relative to electron temperature and density to allow the overestimate of α_{cx} to overcome the underestimate of N . Therefore, estimates of τ_{cx} near the plasma edge or vacuum chamber wall are not likely to increase, even if decreasing plasma and electron temperatures and decreasing electron density in this region are considered.

It may be more appropriate to use estimates of τ_{cx} near the plasma core in determining the relevance of neutrals to the overall momentum confinement time. Here, due to the higher plasma and electron temperatures and electron densities, the state of underestimate of N and overestimate of α_{cx} are not so profound. Here, τ_{cx} may easily achieve values greater than or equal to τ_M due to the uncertainty in H_α emissivity and its proximity to zero.

More important than the absolute magnitude of the charge-exchange time is that it does not scale the same as the momentum confinement time for changes in mirror

ratio or plasma density. This suggests that charge-exchange has little impact on the momentum confinement time. However, again we point out that the scaling of electron temperature with experimental parameters is unknown and can have a profound effect on neutral density estimates, and hence the charge-exchange time.

4.5 H_α Emissivity Temporal Analysis

The primary focus of this work was to characterize H_α profiles under nominally equilibrium conditions. However, one of the advantages of the HED system is that it is time resolved to about $10 \mu\text{s}$. In this section we present initial, non-extensive, temporal analysis. We illustrate the time history of a typical H_α profile, commenting on the formation and extinguishing of the plasma.

Figure 4.16 shows the time history of an H_α emissivity profile for a typical MCX discharge (MCX080929-41). Here, an Abel inverted profile is produced for every point in time ($1 \mu\text{s}$), but each profile is smoothed prior to inversion, as discussed in Sec. 4.2. The profiles are re-sampled using a cubic-spline interpolation and then combined into a two-dimensional array ($r \times t$), giving the surface plot shown.

The first general observation to note is the large amplitude of the profile at the outer-most chord ($r = 26.3 \text{ cm}$), as seen in the previous sections. Next, is the clear indication of breakdown (between the first two dashed lines) and extinguishing stages ($4 \text{ ms} < t < 6 \text{ ms}$) in Fig. 4.16(a). An expanded view of the time period between the first two dashed lines is shown in Fig. 4.16(b), highlighting the breakdown phase observed at the mid-plane. There are two main observations to note regarding the breakdown stage.

- The discharge appears to start at lower radii and moves outward at about 4 km/s .

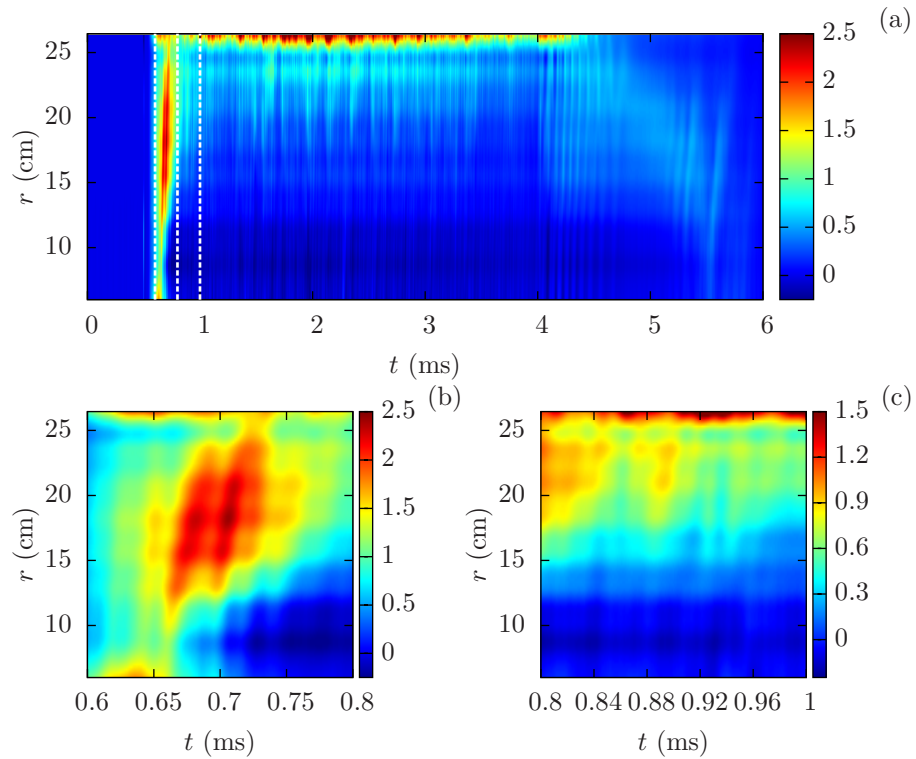


Figure 4.16: Shown is a full time history of a normalized emissivity profile for standard conditions (a). Plots (b) and (c) show expanded views for $0.6 \text{ ms} < t < 0.8 \text{ ms}$ and $0.8 \text{ ms} < t < 1.0 \text{ ms}$, respectively. The color-bars indicate the emissivity in units of $10^{17} \text{ ph. cm}^{-3} \text{ s}^{-1}$. Plot (c) has a reduced color scale in order to reveal the amplitude variation for that time period. (Discharge MCX080929-41.)

- The discharge at the mid-plane seems to have two peaks, separated in time by about $40 \mu\text{s}$, the second of which coincides with the plasma voltage minimum at $700 \mu\text{s}$ (see Fig. 4.2, t_2).

In Fig. 4.2, the initial hold-off stage lasts only $50 \mu\text{s}$ before current begins to flow and “breakdown” commences ($t = 550 \mu\text{s}$). However, Fig. 4.16(b) shows no evidence of breakdown until about $100 \mu\text{s}$ after the breakdown stage begins ($t = 650 \mu\text{s}$). It is possible that the discharge originates somewhere other than at the mid-plane. Nevertheless, the end of the breakdown stage does coincide well with the second H_α peak at $700 \mu\text{s}$. Thus, it is possible that the discharge originates away from the mid-plane but only comes into view at the mid-plane $100 \mu\text{s}$ later. For example, with a temperature of 1 eV , the ion thermal velocity is about 10 km/s . This means the discharge may have originated about 1 m from the mid-plane which is near the insulator region.

The two separate structures in Fig. 4.16(b) suggests either a “double” discharge or possibly a single discharge “blob” which is rotating. If it is a single blob rotating, the time separation between renditions ($40 \mu\text{s}$) suggests a rotation velocity of about 27 km/s , which is not implausible. Furthermore, the apparent radial velocity may be due to the angular and radial separation of the chords, i.e. rotating at fixed radial location the blob would be viewed first by the inner-most radial chord and later viewed by outer chords. However, the inner-most chord ought to view the blob last as it passes around on the side nearest the collection optics, resulting in a type of zig-zag pattern. This is not seen in Fig. 4.16(b)., and therefore the most likely explanation is the existence of two separate breakdown structures. This does not preclude some angular motion of the structures; if the motion is entirely azimuthal then an angular separation of about 60° between the inner and outer-most chords would suggest a rotation velocity no larger than about 3.5 km/s .

The observation regarding the extinguishing of the plasma ($4 \text{ ms} < t < 6 \text{ ms}$) is that it appears to extinguish inward, i.e. from larger radii to smaller radii.

4.6 Conclusions

There are several major conclusions which we have arrived at based on the results of this experiment.

- The location of the inner and outer-most flux surfaces cannot be confirmed under the present experimental conditions, except possibly that the outer-most flux surface coincides with the chamber wall.
- The variation of controllable parameters suggests that plasma interaction with the vacuum chamber wall may be dictating the emissivity profile since relative emissivity profiles remain unchanged except for the outer-most chord.
- The profile shape predicted by the NMGC model does not accurately predict the H_α emissivity profile. However, the moderate agreement between the predicted scaling of the NMGC model and the scaling of the estimated neutral density from emissivity measurements is compelling.
- The disagreement in magnitude between charge-exchange times and momentum confinement times and the disagreement in scaling in the mirror ratio and plasma density scan, suggests that charge-exchange may not significantly contribute to the momentum confinement time.

Determination of the inner and outer-most flux surfaces (r_1 and r_2 , respectively) has real implications for at least two MCX measurements: the rotation velocity, $\langle u_\phi \rangle = V_p/aB_{\text{mid}}$, where $a = r_2 - r_1$; and the plasma density. Both the inner and outer-most flux surfaces have been assumed to be the same as their vacuum location. This may be inaccurate in the presence of plasma, particularly when considering the moderate Alfvén Mach numbers observed. The presumed plasma width for a mirror

ratio of 6 is about 18.4 cm and is unlikely to be smaller than this since the outermost flux surface should have a propensity to move outward due to the centrifugal force of the plasma. Thus a may be slightly underestimated and the rotation velocity may be overestimated. The plasma density calculation is based on a single chord interferometer with impact parameter 16.5 cm, and thus is inversely dependent on the path length through the plasma, $n \sim \Delta\phi/l$, where $\Delta\phi$ is the phase shift of the interferometer and $l = 2\sqrt{r_2^2 - 16.5^2}$. Thus the plasma density calculation may be slightly overestimated since an increase in r_2 increases the path length through the plasma, reducing the required density needed to produce a given interferometric phase shift. An overestimate on rotation velocity and plasma density both imply an overestimate on M_A .

The main shortcoming of the HED array in measuring neutral density is that it does not have complementary multi-chord density and temperature diagnostics. In principle, with these capabilities, a neutral density measurement would be nearly direct, requiring only the use of an atomic model to link electron density & temperature and H_α emissivity to neutral density. Without these, however, estimating neutral density requires an assumption (crude model) of these quantities. This is precisely what has been done in this chapter. Unfortunately, since the H_α emissivity profiles predicted by both the NMG and NMGC models seem to be contradicted by the observations, an even cruder assumption had to be made, i.e. uniform electron density and temperature profiles. While the inclusion of centrifugal terms in the model (NMGC) may help explain why the emissivity profile is not hollow and dominates near the outboard side of the plasma, the relative profile of the NMGC model remains dissimilar to the observations in curvature and inflection. In addition, to achieve similar emissivity values by the NMGC model, it was required to assume ion and electron temperatures of 30 eV and 2.5 eV, respectively. These are not implausible, and may be consistent with the possible temperature gradients near the edge of the plasma.

However, as mentioned earlier, in this electron temperature range, small changes in T_e have large effects on the ionization rate coefficient and emission rate for H_α , thus it is relatively easy to adjust emissivity magnitudes for a model with only modest temperature adjustments.

The small charge-exchange times relative to the momentum confinement times suggests a more complicated relationship between the two. The presumption that charge-exchange is directly related to momentum confinement assumes that the charge-exchange mean-free-path for a neutral particle is larger than the system size, i.e. if an ion in the core of the plasma becomes a neutral through charge-exchange, this resulting fast neutral will most likely escape the plasma without experiencing another charge-exchange (back to an ion). Under this situation, the ion charge-exchange time should determine the momentum confinement time. However, if the charge-exchange mean-free-path for a neutral is much smaller than the system size, then an ion which becomes a fast neutral will charge-exchange back to an ion before it (and its momentum) can escape. Indeed, $\lambda_{cx} = v_T/n\alpha_{cx} \cong 2 \text{ mm}$ for a 15 eV neutral near the core of the plasma ($n \cong 7 \times 10^{14} \text{ cm}^{-3}$). This means that it is possible that very small ion charge-exchange times could be related to larger momentum confinement times since many charge-exchange events are required before an ion's momentum escapes the system.

Chapter 5

Future Developments

In this chapter we discuss the possibilities for enhancing or augmenting our understanding of the role that neutral particles play in the behavior of MCX discharges. These are primarily motivated by the shortcomings in the theory and diagnostics discussed previously in this work. Future experiments are also recommended.

5.1 Neutral Modeling Improvement

One of the primary concerns with the neutral and plasma modeling presented in this dissertation is the lack of comprehensive treatment of the fluid equations. In Sec. 2.4 we presented two diffusion models. We were able to compare general scaling of these models to the experimental results but there remains an uncertainty in the applicability of both models due to discrepancies in the profiles. In particular, the isothermal assumption may be inaccurate and may change the density profiles significantly due to the temperature dependence of the ionization, recombination, and charge-exchange rate coefficients, as well as the H_α emission rate, ν_α .

Ng made significant progress in modeling neutral behavior for an MCX type discharge [32]. He also began work on adapting his neutral model to more accurately reflect MCX magnetic field geometry. Unfortunately, neither of his 2D models include centrifugal treatment in the radial direction and he made isothermal assumptions. According to Simpson [38], centrifugal forces in the radial direction are important for neutrals as well. Thus it is necessary to have a more comprehensive model for neutrals. Indeed, the NMGC model presented in Sec. 2.4 is compelling in this regard. While it does not agree with the emissivity observations entirely, it correctly predicts

outboard dominated emissivity and the nominal magnitude can be made to agree with only moderate adjustments to the assumed temperatures. Thus it may be worthwhile to include centrifugal terms in Ng’s 2D model. In addition, it may be useful to explore neutral blanket boundary conditions rather than hard wall boundary conditions.

Huang developed a full 3D MHD code with MCX field geometry which included temperature dependence as well as viscosity and thermal conductivity, however it does not consider neutrals [39]. Ideally, we could consider modifying Huang’s full 3D MHD code to include a full 3D treatment of neutrals. However, this may be too ambitious as a next step since this would involve adding one scalar (continuity) and two vector (momentum & pressure) equations to the existing code, as well as adding coupling terms (ionization, recombination, and charge-exchange). Another approach would be to use Huang’s existing MHD simulation and add neutral particle treatment in a Monte-Carlo fashion, similar to DEGAS [40]. Here, the plasma behavior is determined independent of neutrals and the neutral behavior is dictated by a “fixed” plasma background. This has the advantage that Huang’s code need not be modified. However, this has the disadvantage that neutral particles would be treated as a perturbation, which may not be appropriate.

5.2 H_α Emission Detector Improvement

There are three possible improvements which can be made to the H_α emission detector. However, due to the current intended use of the HED array, the author does not recommend making any improvements. In order of importance, the possible improvements are:

1. Reduce systematic error in emissivity measurements through the use of appropriate beam dumps.

2. Update the Thorlabs DET110 photo-detectors on HEDs numbered 1–7 to the Thorlabs PDA36A.
3. Improve spatial resolution, temporal resolution, and detection sensitivity.

The most pressing improvement needed in regard to H_α measurements is to reduce the systematic error. While we demonstrated in Sec. 3.2 that reflections from the vacuum chamber wall should be negligible, this investigation did not include all possible view chord locations. Furthermore, in Sec. 4.2 we determined that there still remained systematic error most likely attributed to reflections. The most appropriate way to mitigate reflections is to use a beam dump, such as stacked razor blades. Unfortunately, the existing vacuum chamber does not afford the space required to implement this type of beam dump. The use of non-reflective material (such as flock paper), which occupies negligible space, seems to be the only method available; however, this is also infeasible considering that plasma is undoubtedly “scraping” the chamber wall at the mid-plane, thus any material applied to the chamber wall will not only be damaged and contaminate the discharge, but may become an emission source itself. Ideally, the vacuum chamber would be modified (or a new one designed) to include the necessary recesses in which beam dumps could be placed. Nevertheless, the systematic error, while the most important, is not significant enough to warrant such expensive endeavors and useful information can continue to be gleaned from the HED array.

Updating the seven DET110s to PDA36As will improve the signal to noise ratio for those HEDs due to the superior amplifier in the PDA36A. This is certainly simple to implement and would only cost about \$2k.

Lastly, it would be rather simple to improve the spatial resolution of the HED array by making the collection optics more compact and adding more HED systems to the array. It is possible to use 1/4” standard optics for the collection optics assembly, making it more compact and allowing more detectors to use a single viewport. This

will, of course, decrease the signal strength of an HED by about a factor of 4 from its current configuration, so it may be desirable to improve the sensitivity of the system as well. Improved sensitivity could be accomplished with the use of photo-multiplier units in place of photo-diode units. This has the additional advantage of greatly improving the time response. However, this would likely increase the cost of a single HED considerably. Improved spatial and temporal resolution, however, are not priorities at present, nor would they necessarily be priorities in the future.

5.3 Future Experiments

The importance of electron temperature has been emphasized throughout this dissertation and we recommend implementing Langmuir probes for addressing this issue. The use of such a probe at the mid-plane could provide valuable information about electron density and temperature near the plasma edge. Minor efforts have been made in the past to implement Langmuir probes, however, serious attention has not been given to the the technical requirements of such an endeavour. This should be given a high priority in the near future.

In this work, we have not made any consideration for impurity ions or impurity neutrals, nor have we considered molecular hydrogen and its dissociation process. We have only considered a purely hydrogenic plasma with neutral atomic hydrogen. However, these may be important factors in plasma confinement devices. In particular, radiation from carbon ions may be a significant energy loss mechanism. Indeed, plasma interaction with impurities is currently of significant interest in research regarding radiative and collisional processes, particularly in the context of Tokamak divertor regions, where temperatures are much lower than that of the core plasma [29]. Plasma temperatures for MCX discharges are comparable to those of Tokamak divertor regions, thus impurity species may play a significant role.

There has not been any work done in the past to investigate the impurity level in MCX discharges. However, there are efforts currently under way to reduce impurity levels through baking and glow-discharge cleaning. These efforts may also provide insight into whether or not the vacuum chamber is a significant source of neutral particles during discharges. Collisional-radiative codes [30] are capable of treating impurities, particularly carbon, so an estimate of impurity concentrations should be possible by measuring the absolute emission of one or more emission lines. This, too, would require better understanding of electron temperature and density. An impurity emission detector (IED) could be made by replacing the interference filter in an H_α emission detector with one appropriate for an impurity emission line.

A topic of behavior related to neutrals which has not been addressed significantly in this work is the Critical Ionization Velocity effect (CIV) [23]. Nevertheless, studying this phenomenon is crucial to understanding MCX discharge behavior. Work has been done to study evidence of the existence of this effect in MCX discharges and the source of this effect is believed to originate at the end insulators [25]. By determining neutral density and profiles near the insulator, we may be able to confirm whether the CIV effect is determined near the insulator or at other locations. This would require an independent measurement of plasma density in the region near the insulator, and thus may not be practical. Another impediment is the lack of optical access to the insulator region, i.e. there are not any viewports which adequately view the insulator region. This is because the insulator face lies in the middle of the solenoid magnets, thus barring any direct view of the insulator faces. However, it may be beneficial to conduct similar experiments in the transition region ($z \sim 80$ cm) of the plasma discharge, where optical access is available and a second interferometer is currently being installed.

Appendix A

Neutral Model Derivations

Neutral modeling has been initiated in the context of centrifugally confined plasmas by Sheung-Wah Ng [32]. In his doctoral dissertation, Ng presented a 1D two-fluid diffusion model in magnetic field with slab geometry, similar to the work of Goldston & Rutherford [31]. The modification made from Goldston's treatment was to allow for density dependence in the diffusion coefficients and to allow for a moderate system size. This model will be derived in this appendix and is termed the Numerical Modified Goldston-Rutherford (NMG) model. A second model is also derived which is identical to NMG except that centrifugal terms are not discarded. The latter model is the work of the author and termed the Numerical Modified Goldston-Rutherford Centrifugal (NMGC) model.

The models in the following sections focus on a 1D cross-field treatment at the mid-plane of MCX discharges. We will begin the derivation from Eqs. (2.1)–(2.4) and progress to a common point among both models, after which the remainder of each derivation will be completed in turn. For convenience we duplicate Eqs. (2.1)–(2.4) here.

$$\frac{\partial n}{\partial t} + \nabla \cdot (n\mathbf{u}) = -n^2\alpha_r + nN\alpha_i \quad (\text{A.1})$$

$$m\frac{\partial n\mathbf{u}}{\partial t} + m\nabla \cdot (n\mathbf{u}\mathbf{u}) + \nabla p = \frac{1}{c}\mathbf{j} \times \mathbf{B} - mn^2\alpha_r\mathbf{u} + mnN\alpha_i\mathbf{U} - mnN\alpha_{cx}(\mathbf{u} - \mathbf{U}) \quad (\text{A.2})$$

$$\frac{\partial N}{\partial t} + \nabla \cdot (N\mathbf{U}) = n^2\alpha_r - nN\alpha_i \quad (\text{A.3})$$

$$m\frac{\partial N\mathbf{U}}{\partial t} + m\nabla \cdot (N\mathbf{U}\mathbf{U}) + \nabla P = mn^2\alpha_r\mathbf{u} - mnN\alpha_i\mathbf{U} + mnN\alpha_{cx}(\mathbf{u} - \mathbf{U}) . \quad (\text{A.4})$$

Here, all terms have their usual meanings, uppercase indicates neutral quantities, lowercase indicates plasma quantities, α_i is the ionization rate coefficient, α_r is the recombination rate coefficient, and α_{cx} is the charge-exchange rate coefficient.

By expanding the divergence terms in Eqs. (A.2) & (A.4), using Eqs. (A.1) & (A.3), and considering dynamic equilibrium, we obtain the following.

$$\nabla \cdot (n\mathbf{u}) = -n^2\alpha_r + nN\alpha_i \quad (\text{A.5})$$

$$mn\mathbf{u} \cdot \nabla\mathbf{u} + \nabla p = \frac{1}{c}\mathbf{j} \times \mathbf{B} - mnN(\alpha_{cx} + \alpha_i)(\mathbf{u} - \mathbf{U}) \quad (\text{A.6})$$

$$\nabla \cdot (N\mathbf{U}) = n^2\alpha_r - nN\alpha_i \quad (\text{A.7})$$

$$mN\mathbf{U} \cdot \nabla\mathbf{U} + \nabla P = mn(N\alpha_{cx} + n\alpha_r)(\mathbf{u} - \mathbf{U}) . \quad (\text{A.8})$$

Since we are considering only the mid-plane location and azimuthal symmetry, we can make the following assumptions.

- Scalar quantities are independent of ϕ due to azimuthal symmetry.
- All quantities are independent of z at the mid-plane due to reflective symmetry, except possibly quantities in the \hat{z} direction.
- We assume isothermal conditions.

These allow the convective terms in the momentum equations to have the form

$$\mathbf{u} \cdot \nabla \mathbf{u} = \left(u_r \partial_r u_r - \frac{1}{r} u_\phi^2 \right) \hat{\mathbf{r}} + \left(u_r \partial_r u_\phi + \frac{1}{r} u_r u_\phi \right) \hat{\phi} + (u_r \partial_r u_z + u_z) \hat{\mathbf{z}}. \quad (\text{A.9})$$

We will now address the $\mathbf{j} \times \mathbf{B}$ term and use resistive Ohm's law to express it in terms of \mathbf{u} .

$$\mathbf{E} + \frac{1}{c} \mathbf{u} \times \mathbf{B} = \eta \mathbf{j} \quad (\text{A.10})$$

$$\begin{aligned} \mathbf{E} \times \mathbf{B} + \frac{1}{c} (\mathbf{u} \times \mathbf{B}) \times \mathbf{B} &= \eta \mathbf{j} \times \mathbf{B} \\ -\frac{B^2}{\eta c} \left[\mathbf{u} - (\mathbf{u} \cdot \hat{\mathbf{b}}) \hat{\mathbf{b}} \right] + \frac{1}{\eta} \mathbf{E} \times \mathbf{B} &= \mathbf{j} \times \mathbf{B}. \end{aligned} \quad (\text{A.11})$$

Using Eq. (A.11), the assumptions mentioned above, Eq. (A.9), and only considering a 1D system in the radial direction (taking scalar product of vector equations with $\hat{\mathbf{r}}$), we have the following.

$$\partial_r n u_r + \frac{1}{r} n u_r + n \partial_z u_z = -n^2 \alpha_r + n N \alpha_i \quad (\text{A.12})$$

$$m n (u_r \partial_r u_r - g) + 2T \partial_r n = -\frac{B^2}{\eta c^2} u_r - m n N (\alpha_{cx} + \alpha_i) (u_r - U_r) \quad (\text{A.13})$$

$$\partial_r N U_r + \frac{1}{r} N U_r + N \partial_z U_z = n^2 \alpha_r - n N \alpha_i \quad (\text{A.14})$$

$$m N (U_r \partial_r U_r - G) + T \partial_r N = m n (N \alpha_{cx} + n \alpha_r) (u_r - U_r), \quad (\text{A.15})$$

where $g \equiv u_\phi^2/r$ and $G \equiv U_\phi^2/r$ are the centrifugal terms for the plasma and neutral fluids, respectively. Note that $\mathbf{E} \times \mathbf{B}$ does not have a radial component since $\mathbf{B} = B_z \hat{\mathbf{z}}$ and we assume time independence ($\partial_t \mathbf{B} = c \nabla \times \mathbf{E} = 0$). Furthermore, we assume

$\alpha_r \ll \alpha_i, \alpha_{cx}$ and $u_r \ll U_r \ll \sqrt{T/m}$. This leaves

$$(nu)' = nN\nu_i \quad (\text{A.16})$$

$$-mng + 2Tn' = -\frac{B^2}{\eta c^2}u \quad (\text{A.17})$$

$$(NU)' = -nN\alpha_i \quad (\text{A.18})$$

$$-mNG + TN' = -mnN\alpha_{cx}U, \quad (\text{A.19})$$

where prime denotes ∂_r .

We now normalize the equations as follows: densities by n_0 , the maximum plasma density, velocities by $\sqrt{T/m}$, and lengths by $l_0 = \sqrt{\lambda_{cx}\lambda_i} = \sqrt{T/mn_0^2\alpha_{cx}\alpha_i}$, the geometric mean of the charge-exchange and ionization mean-free-path for a neutral atom at the location of maximum plasma density. The normalized equations are as follows.

$$(\hat{n}\hat{u})' = a\hat{n}\hat{N} \quad (\text{A.20})$$

$$\hat{n}' = \frac{1}{2}(\hat{n}\hat{g} - b\hat{u}) \quad (\text{A.21})$$

$$(\hat{N}\hat{U})' = -a\hat{n}\hat{N} \quad (\text{A.22})$$

$$\hat{N}' = \hat{N}\hat{G} - \frac{1}{a}\hat{n}\hat{N}\hat{U}, \quad (\text{A.23})$$

where we have defined

$$a \equiv \sqrt{\frac{\alpha_i}{\alpha_{cx}}} \quad (\text{A.24})$$

$$b \equiv \frac{B^2}{\eta mc^2 n_0^2 \sqrt{\alpha_i \alpha_{cx}}}. \quad (\text{A.25})$$

Adding Eq. (A.20) to Eq. (A.22) and integrating, using perfect recycling at the boundary, gives

$$\hat{n}\hat{u} + \hat{N}\hat{U} = 0. \quad (\text{A.26})$$

Solving Eq. (A.23) for $\hat{N}\hat{U} = \left(\hat{N}\hat{U} - \hat{N}'\right) a/\hat{n}$ and Eq. (A.21) for $\hat{u} = (\hat{n}\hat{g} - 2\hat{n}')/b$, and inserting these into Eq. (A.26) gives

$$(\hat{n}^2\hat{g} - 2\hat{n}\hat{n}') \frac{1}{b} + \left(\hat{N}\hat{G} - \hat{N}'\right) \frac{a}{\hat{n}} = 0. \quad (\text{A.27})$$

Solving Eq.(A.20) for \hat{N} , inserting \hat{u} , and taking its derivative gives

$$\hat{N} = \frac{(\hat{n}\hat{u})'}{a\hat{n}} = \frac{(\hat{n}^2\hat{g} - 2\hat{n}\hat{n}')'}{ab\hat{n}} \quad (\text{A.28})$$

$$\hat{N}' = \left[\frac{(\hat{n}^2\hat{g} - 2\hat{n}\hat{n}')'}{ab\hat{n}} \right]'. \quad (\text{A.29})$$

Inserting these into Eq. (A.27) gives a differential equation for the normalized plasma density.

$$\begin{aligned} \hat{n}^3\hat{g} - 2\hat{n}^2\hat{n}' + \frac{1}{\hat{n}} (\hat{n}^2\hat{g} - 2\hat{n}\hat{n}')' \hat{G} - \left[\frac{1}{\hat{n}} (\hat{n}^2\hat{g} - 2\hat{n}\hat{n}')' \right]' &= 0 \\ \hat{n}^3\hat{g} + \frac{1}{\hat{n}} (\hat{n}^2\hat{g} - 2\hat{n}\hat{n}')' \hat{G} - \left[\frac{1}{\hat{n}} (\hat{n}^2\hat{g})' \right]' - 2\hat{n}^2\hat{n}' + \left[\frac{2}{\hat{n}} (\hat{n}\hat{n}')' \right]' &= 0. \end{aligned} \quad (\text{A.30})$$

This can be simplified by making the substitution $y = n^2$, with the following result.

$$\begin{aligned} \hat{g}y^2 + \hat{G} \left(\hat{g}y - \frac{1}{2}y' \right)' - (\hat{g}y)'' + \frac{1}{2} \frac{y'}{y} (\hat{g}y)' \\ - \frac{1}{3}y^{1/2} (y^{3/2})' + \frac{1}{2}y^{1/2} [y^{-1/2}y'']' &= 0. \end{aligned} \quad (\text{A.31})$$

The two models diverge beyond this point. If we neglect the centrifugal terms ($g = G = 0$), then we recover the solution by Ng [32].

$$-\frac{2}{3}(y^{3/2})' + [y^{-1/2}y'']' = 0$$

$$y'' = \frac{2}{3}(y^2 - cy^{1/2}) \quad (\text{A.32})$$

$$\hat{n} = y^{1/2} \quad (\text{A.33})$$

$$\hat{N} = \frac{1}{3}D(c - y^{3/2}), \quad (\text{A.34})$$

where we have used Eqs. (A.24), (A.25), (A.28), and (A.32), as well as defined $D \equiv \eta mc^2 \alpha_{cx} n_0^2 / B^2$ to obtain the expression for N .

The second model is obtained by retaining the centrifugal terms but simplifying by setting $g = G$. This is justified since we expect that, through charge-exchange, the neutral particles will be dragged along with the azimuthal plasma flow. After some algebra, the result is

$$y''' = -\hat{g}y^2 - \hat{g}\hat{g}'y + \hat{g}''y + \frac{3}{2}\hat{g}'y' - \hat{g}^2y' + 2\hat{g}y'' - \frac{1}{2}\hat{g}\frac{(y')^2}{y} + yy' + \frac{1}{2}\frac{y'}{y}y'' \quad (\text{A.35})$$

$$\hat{n} = y^{1/2}$$

$$\hat{N} = D \frac{\hat{g}y' + \hat{g}'y - y''}{\sqrt{y}}. \quad (\text{A.36})$$

For simplicity, \hat{g} is assumed parabolic, having a maximum at the nominal center of the plasma ($r = 15$ cm) and equal to zero at the plasma boundary. It is expressed as

$$\hat{g} = \frac{M_s^2}{\hat{r}_0} \left(1 - \frac{4\hat{r}^2}{\hat{a}^2} \right),$$

where $M_s \cong 2$ is the ion sonic mach number, $\hat{r}_0 = r_0/l_0 = 15$ cm/ l_0 is the normalized ‘‘center’’ of the plasma, and $\hat{a} = a/l_0 \cong 20$ cm/ l_0 is the nominal plasma width.

Equations (A.32) & (A.35) are solved with the use of Matlab’s `ode45` solver and `lsqnonlin` non-linear least-square optimizer in a “shooting” scheme. Initial left boundary conditions are chosen ($y(0) = 0$ and sufficiently more derivatives), then the least-square optimizer optimizes over the left boundary conditions (except $y(0) = 0$) until `ode45` produces a solution satisfying the constraints $y(r_{\max}) = 0$ and $y_{\max} = 1$.

Appendix B

Optical Geometry of the HED View Chord

The collection optics assembly performs the job of collecting optical emissions from MCX discharges in such a way as to provide reasonable spatial resolution. When considering a multi-chord system, it is inherently necessary to consider the “volume” from which emissions are sampled in each chord. It is thus necessary to understand the optical geometry of the viewing chord of the collection optics. In the following analysis of the chord viewing volume, we show that the configuration of the collection optics gives a uniform effective solid-angle along the optic axis, making line-integrated chord measurements much easier to interpret and unfold in Abel inversions. This is an extension to the work done by Alan DeSilva [41].

The measured value of the emissivity, γ_α , depends on the geometry of the collection optics. The detector measures optical power which is proportional to the rate that photons strike the detector. If we consider a loss-less optical system, the rate that photons strike the detector is equal to the rate at which photons enter the system, \mathcal{N}_α . Since each HED system collects photons along a line-of-sight, the total rate of photon collection is the integration over the chordal viewing volume of the spatially dependent plasma emissivity, γ_α , and the solid-angle (in steradians) of the collection optics as seen by a source point, $g(\mathbf{r})$. This is summarized in the following expression (c.f. Eq. (3.5)).

$$\mathcal{N}_\alpha = \int_{\mathcal{V}} \frac{\gamma_\alpha(\mathbf{r})}{4\pi \text{ sr.}} g(\mathbf{r}) d\mathcal{V} . \quad (\text{B.1})$$

A factor of 4π sr. is included since γ_α is uniform in solid-angle. The solid-angle of a source point is purely a function of the configuration of the collection optics and will be determined forthwith. Our collection optics assembly consists of a 1/2-inch plano-convex lens, an optical fiber, and standard 1/2-inch lens tube pieces. The optical fiber tip is placed relative to the lens such that its optical image is the same diameter as the lens' clear aperture (11 mm) and its image distance (77.3 cm) is larger than the diameter of the MCX vacuum chamber (~ 60 cm). This ensures that the viewing volume of the optical system is limited to the cylindrical “tube” described by the lens and the image of the fiber tip.

The defined viewing volume can be understood in the following way. The path of a light ray passing through the lens and through the optical fiber tip can be extended backward to a point on the fiber image. This is just a restatement of first-order geometric optics. Now consider a light ray originating from any location between the lens and the fiber image. Clearly, if this light ray is to be “collected” by the fiber, its ray must pass through the lens. However, it is also required that this light ray's backward trajectory also pass through the fiber image, otherwise it will be mapped to a location outside the fiber tip and will not be collected. Thus, for locations between the lens and fiber image, the viewing volume is restricted to points lying inside the “tube” defined by the lens and the fiber image, since this is the only region in which a straight line can pass through both the lens and fiber image.

Now that we have defined our viewing volume, we can turn our attention to the solid-angle of a point source, $g(\mathbf{r})$. Expanding the integral in Eq. (B.1) and incorporating the limits of the viewing volume, we have

$$\mathcal{N}_\alpha = \int_0^L \frac{\gamma_\alpha(z)}{4\pi \text{ sr.}} \int_0^{2\pi} d\phi \int_0^R g(r, z) r dr dz, \quad (\text{B.2})$$

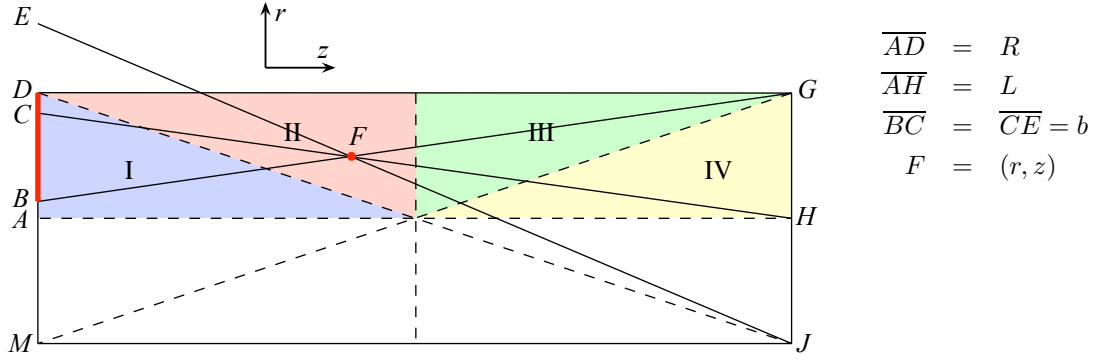


Figure B.1: Shown is a longitudinal cross-section of the optical geometry for an HED collection optics assembly. Segment \overline{DM} represents the lens and segment \overline{GJ} represents the image of the optical fiber tip. There is rotational symmetry about the optic axis, segment \overline{AH} . The colored regions labeled I, II, III, and IV each have different expressions for the solid-angle of light collected by the optical fiber from a point source with coordinates (r, z) located within that region (see Eqs. (B.3) & (B.4)).

where we have used cylindrical coordinates with the origin at the center of the lens, the z axis extends along the optic axis, and r is measured from the optic axis. Also, L is the fiber image distance and R is the radius of both the lens and fiber image. We have also assumed that the cylindrical viewing volume is narrow enough that γ_α does not vary across its diameter, i.e. $\gamma_\alpha(\mathbf{r}) \cong \gamma_\alpha(z)$. In Fig. B.1 we illustrate the viewing volume geometry. Segment \overline{DM} represents the lens, segment \overline{GJ} represents the fiber image, and point F is an emission source located at (r, z) . Symmetry about the optic axis (\overline{AH}) is assumed.

We refer to Figs. B.1 & B.2 in order to determine $g(r, z)$. The definition for $g(r, z)$ is simply the solid-angle of the source point which overlaps the lens as well as the fiber image. This is represented by the segment \overline{BD} . We calculate this solid-angle from the overlapping area of the circles defined by the lens diameter \overline{DM} and the segment \overline{BE} . This overlapping area is shown in Fig. B.2 as the red-shaded region.

The collection region shown in Fig. B.1 is divided into four regions, each representing a different constraint on the light rays capable of passing into the fiber. For a source point lying in region I, light rays are constrained by the points G and J ; for

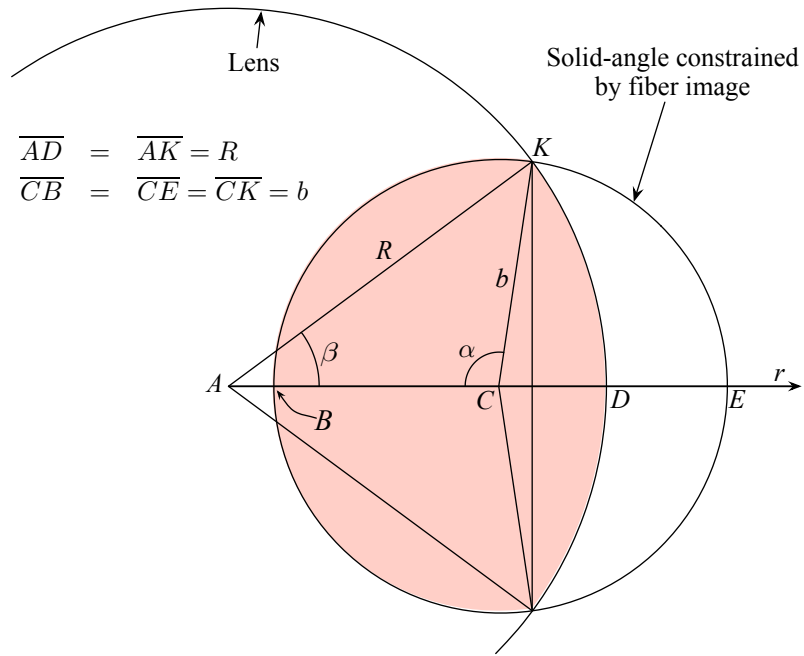


Figure B.2: The light collected by the optical fiber tip from a source point, (z, r) (see Fig. B.1), subtends a solid-angle represented by the red shaded region. The circle with radius R represents the lens (Fig. B.1, segment \overline{AD}) and the circle with radius b represents the solid-angle of the source point constrained by the fiber image (Fig. B.1, segment \overline{GJ}). The segment labels are the same as those in B.1. The z -axis (optic axis) is pointing out of the page.

region IV, it will be the points D and M . For region II and III, the constraint will be from the points D and G . Figures B.1 & B.2 are correlated, i.e. points with the same label in both figures represent the same physical point.

We proceed by describing the area of the red shaded region in Fig. B.2 as a function of the source position, (r, z) . The expression for this area, A , is different depending on whether the source point is located in region I, II, III, or IV. The procedure for obtaining the relevant expressions is tedious but straight-forward. Using normalized coordinates, $\hat{z} = z/L$, $\hat{r} = r/R$, and $\hat{A} = A/\pi R^2$ (see Figs. B.1 and B.2), these expressions are

$$\hat{A}(\hat{r}, \hat{z}) = \begin{cases} \frac{\hat{z}^2}{(1 - \hat{z})^2} \cos \theta & , \text{ Region I} \\ \frac{\cos \theta}{\pi} \left[\cos^{-1} \left(\frac{\hat{r}^2 + 1 - 2\hat{z}}{2\hat{r}(1 - \hat{z})} \right) + \frac{\hat{z}^2}{(1 - \hat{z})^2} \cos^{-1} \left(\frac{\hat{r}^2 - 1 + 2\hat{z}}{2\hat{r}\hat{z}} \right) - \frac{\hat{r}}{1 - \hat{z}} \sqrt{1 - \left(\frac{\hat{r}^2 + 1 - 2\hat{z}}{2\hat{r}(1 - \hat{z})} \right)^2} \right] & , \text{ Region II, III} \\ \cos \theta & , \text{ Region IV,} \end{cases} \quad (\text{B.3})$$

$$g(\hat{r}, \hat{z}) = \frac{A(r, z)}{z^2} = \frac{\pi R^2}{L^2} \frac{\hat{A}(\hat{r}, \hat{z})}{\hat{z}^2}. \quad (\text{B.4})$$

Figure B.3 is a plot of Eq. (B.4) as a function of normalized distance from the optic axis, \hat{r} , for various normalized positions along the optic axis, \hat{z} . For $\hat{z} = 0.5$, half way between the lens and the image of the fiber tip, the area of the light cone intersected by the lens exactly coincides with the area of the lens. As the point moves from the optic axis, the light cone no longer coincides perfectly and less of the light is collected by the fiber. For positions $\hat{z} < 0.5$, the intersection of the light cone and the lens is completely subsumed by the lens, thus movement away from the optic axis

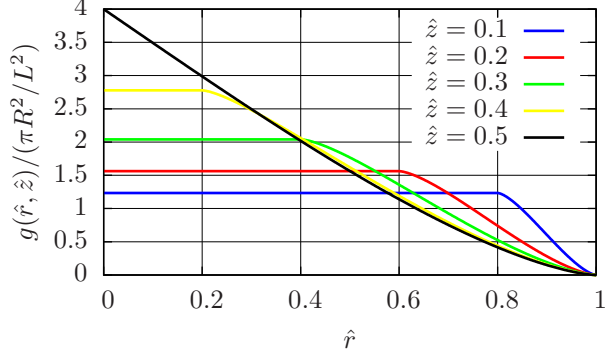


Figure B.3: Shown is the normalized solid-angle of light collected from a source point as a function of the source point's normalized location, (\hat{r}, \hat{z}) . \hat{r} is the radial coordinate measured from the optic axis and normalized to the lens radius; \hat{z} is the longitudinal coordinate (along the optic axis) normalized to the image distance.

does not change the amount of light collected by the fiber until the light cone reaches the lens boundary, beyond which the coincident area diminishes.

The integration over z in Eq. (B.2) is the subject of the Abel transform, which is discussed in Appendix C. Here we want to determine the effective solid-angle as a function of z , thus we are concerned only with the ϕ and r integrations of Eq. (B.2). The effective solid-angle is expressed as follows.

$$\begin{aligned}
G(z) &= \frac{1}{\pi R^2} \int_0^{2\pi} \int_0^R g(r, z) r \, dr \, d\phi \\
&= \frac{1}{\pi R^2} \int_0^{2\pi} \int_0^R \frac{\pi R^2 \hat{A}(\hat{r}, \hat{z})}{L^2 \hat{z}^2} r \, dr \, d\phi \\
&= 2 \frac{\pi R^2}{L^2} \left[\int_0^{1-2\hat{z}} \frac{\hat{A}_I}{\hat{z}^2} \hat{r} \, d\hat{r} + \int_{1-2\hat{z}}^1 \frac{\hat{A}_{II}}{\hat{z}^2} \hat{r} \, d\hat{r} \right. \\
&\quad \left. + \int_0^{2\hat{z}-1} \frac{\hat{A}_{IV}}{\hat{z}^2} \hat{r} \, d\hat{r} + \int_{2\hat{z}-1}^1 \frac{\hat{A}_{III}}{\hat{z}^2} \hat{r} \, d\hat{r} \right]. \tag{B.5}
\end{aligned}$$

We note here that the integrals over $\hat{A}_I \hat{r} / \hat{z}^2$ and $\hat{A}_{IV} \hat{r} / \hat{z}^2$ are identical under the coordinate transformation $\hat{z} \rightarrow 1 - \hat{z}$ (reflection symmetry about $\hat{z} = 0.5$); this is also true for the integrals over $\hat{A}_{II} \hat{r} / \hat{z}^2$ and $\hat{A}_{III} \hat{r} / \hat{z}^2$. This means that we only have

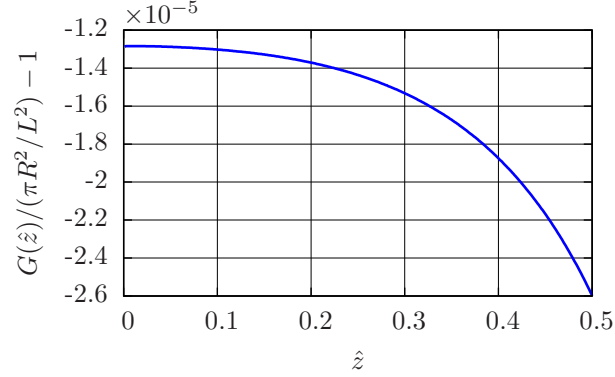


Figure B.4: Shown is the deviation of the effective solid-angle, G , as a function of distance along the optic axis. \hat{z} is the distance along the optic axis, normalized by L , the image distance. The value of G is very nearly constant between the lens and the optical fiber image. In addition, it is nearly equivalent to the solid-angle subtended by the lens at a distance equal to the image distance, i.e. $\pi R^2/L^2$.

to carry out the integrations for regions I & II, then perform appropriate coordinate transformations to obtain the results for regions III & IV. The result is shown in Fig. B.4 for $0 \leq \hat{z} \leq 0.5$; the result for $0.5 \leq \hat{z} \leq 1$ is identical, but reflected about $\hat{z} = 0.5$. We see that the effective solid-angle deviates very little from $\pi R^2/L^2$ between the lens and the fiber tip image, meaning that it is effectively independent of z . This is what we endeavored to show, and makes chord-integrated signals from an HED much easier to interpret, as emissions anywhere along the optic axis are weighted virtually the same.

In addition to this theoretical treatment, measurements were performed in order to confirm that light sources at different locations along the optic axis are indeed weighted the same in the output signal of an HED. This was done using a uniform light source (integrating sphere), whose output port completely subsumes the cross-section of the optical viewing volume of the collection optics for positions $0 \leq z \leq 77.3$ cm. Measurements were taken with the collection optics viewing the output port at various distances along the optic axis. Since the uniform light source output is constant, any change in the output signal from an HED could be interpreted as a change in the effective solid-angle, i.e. $\delta G(z)$. The result of the measurements is shown in Fig. B.5.

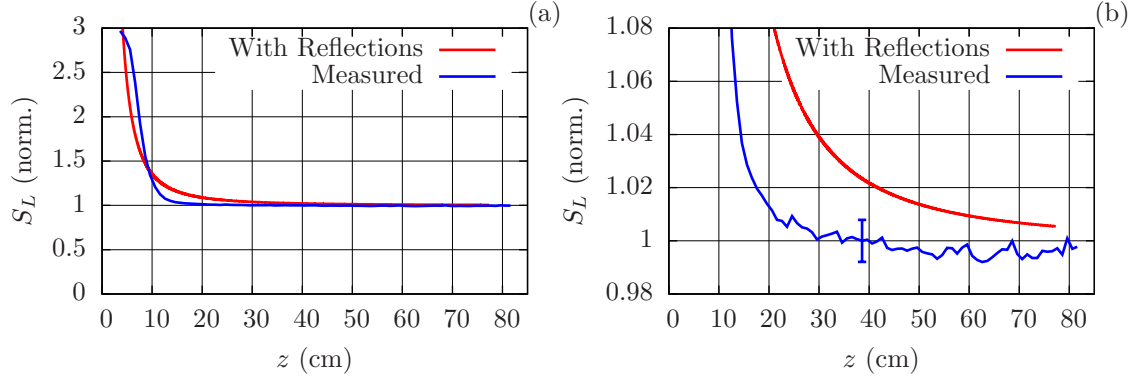


Figure B.5: Shown, as a function of distance along the optic axis, is a normalized signal from an HED viewing a uniform light source (a) and an expanded view (b). Both plots show the possible effect of 0.05% internal reflections contributing to the total signal. The normalized signal is within 1% of unity for $z \gtrsim 20$ cm. Each HED collection optic is further than 15 cm from the interior of the vacuum chamber, as measured along its optic axis.

The data is normalized to the measured signal at $z = 39$ cm. Figure B.5(a) shows that the solid-angle is virtually constant, as predicted, at least for $z \gtrsim 20$ cm. Figure B.5(b) shows the same data over a smaller range in order to show the detail and characteristic error bar.

The increase in the relative signal for $z \lesssim 20$ cm may be explained by reflections inside the collection optic assembly. Recall that not all light passing through the collection lens enters the optical fiber, but only those rays whose backward trajectory also intercepts the fiber tip image. A considerable amount of light passes through the lens into the collection optic assembly that does not directly enter the optical fiber. The red curve in Fig. B.5(a) shows the effect of an estimated 0.05% internal reflection, that is, if 0.05% of all the light entering the collection optics (less the light directly entering the fiber) is eventually reflected into the fiber. A detailed ray tracing and characterization of the reflection properties of the anodized aluminum components would be needed to quantify this effect more precisely. However, the estimate here serves to illustrate that the increased signal at close ranges is consistent with even a small fraction of internal reflection. Nevertheless, collection optic assemblies will be

located no closer than 15 cm to the vacuum chamber, so this effect will be limited to $\leq 3\%$.

Appendix C

Abel Transform

The multi-chord array of H_α emission detectors was conceived to provide profile information for H_α emissivity and hence neutral particle density. The HED is a passive device and therefore relies on information about the interior of the plasma to be carried outside the plasma and to the collection optics of the HED. Necessarily, this introduces a contamination of the emissivity information from the interior of the plasma by emissivity information from larger radii. This means that the photons reaching an HED device may originate from anywhere within its field of view. Hence, an HED signal represents a sum of all the emissions within its field of view, or chord integrated signal. This was laid out in detail in Appendix B. Here, we describe the Abel inversion, a method for extracting local information from an integrated chord measurement in cylindrically symmetric geometries.

Many methods and algorithms have been established for calculating Abel Transforms and their inverses [42–46]. These paradigms have a few things in common: an attempt to decrease computation time and a method to decrease errors associated with an inversion process. Essentially, each method decreases computational expense by separating the geometrically dependent part from the field function part of the Abel transform and its inverse transform. The geometric part is independent of the data to be treated, allowing it to be stored and used for multiple data sets, hence reducing computation time. To address potential errors directly attributable to inversion techniques, most methods employ some type of data interpolation, thereby increasing the data resolution to be inverted and reducing errors which are enhanced by numerical derivatives.

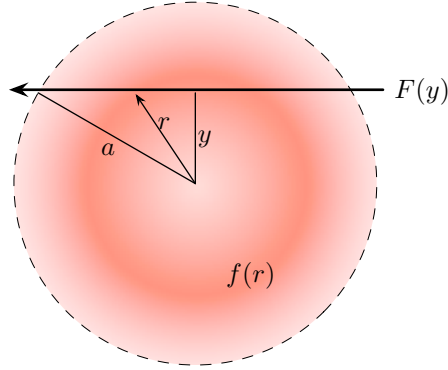


Figure C.1: Shown here is an illustration of a field function, $f(r)$, with chord integrated value, $F(y)$. The differing shades of color are intended to represent different values of the scalar field function $f(r)$.

We begin this appendix by first detailing both the continuous and discrete Abel transforms, drawing attention to the possible errors involved in the inversion process. This is followed by an investigation of the error incurred in applying the discrete Abel inverse transform in the context of the work presented in this dissertation.

C.1 The Continuous & Discrete Abel Transform

The Abel Transform is an integral transform similar to any other integral transform, such as Fourier or Laplace transforms. The Abel transform takes a function in one coordinate space and transforms it into another coordinate space. Like other transforms, the two coordinate spaces have different physical interpretations. For example, the Fourier transform converts a function from the time domain (t) to the frequency domain (ω), and the inverse Fourier transform converts back to the time domain. The Abel transform converts a scalar field function, $f(r)$, from the radial domain to the y domain, interpreted as the impact parameter of an integrated chord measurement.

Consider a known scalar field function, $f(r)$, and its integrated value along a straight line, $F(y)$, shown in Fig. C.1. The value of $F(y)$ can be expressed as

$$F(y) = 2 \int_y^\infty \frac{r}{\sqrt{r^2 - y^2}} f(r) dr, \quad (\text{C.1})$$

where r is the radial coordinate and y is the minimum value of r for the particular chord location, i.e. the impact parameter. The inverse transform is given by [26]

$$f(r) = -\frac{1}{\pi} \int_r^\infty \frac{1}{\sqrt{y^2 - r^2}} \frac{dF}{dy} dy. \quad (\text{C.2})$$

It is straight forward to show that Eqs. (C.1) & (C.2) are inverses of one another by substituting one into the other and evaluating. Notice that the upper limit in both equations is ∞ . In general, knowledge of $f(\infty)$ is required in order to perform the transform, or $F(\infty)$ to perform the inverse transform. If the function $f(r)$ is finite for $r \leq a$ and $f(r) = 0$ for $r > a$, i.e. f is restricted to a finite region in space ($f(\infty) = 0$), then the upper limit in both Eqs. (C.1) & (C.2) can be replaced with a . In practice, this only requires that a multi-chord configuration contain at least one chord located at $y \geq a$. In any case, the outermost chord (located at y_{\max}) will define the upper limit to the inverse transform, however, unless the outermost chord yields no signal, information about $f(r)$ between y_{\max} and a cannot be determined and the inverse transform cannot be performed without making assumptions about a and $f(r)$.

It is a rare situation that either $f(r)$ or $F(y)$ are of such a form that either Eq. (C.1) or Eq. (C.2) can be evaluated analytically. Thus it is requisite to discuss discrete methods for evaluating these two equations. The Abel transform and its inverse can be evaluated using standard numerical integration techniques, however this is computationally expensive. This is clear upon inspection of the transform. To obtain a single Abel Transform value, $F_i = F(y_i)$, for example, the corresponding

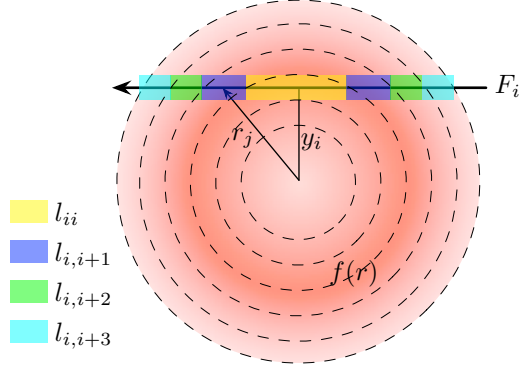


Figure C.2: This illustrates a discrete perspective of the Abel Transform. This is similar to Fig. C.1 except that discrete concentric regions are shown, segregated by dashed circles. Each region that intersects with the viewing chord has a different color rectangle indicating the approximate intersection. The length of these rectangles is the weighting factor applied to f_j and comprises the Abel matrix, l .

integral expression must be evaluated as

$$F_i = \sum_{j=i}^N \frac{r_j}{\sqrt{r_j^2 - y_i^2}} f_j = \sum_{j=i}^N l_{ij} f_j. \quad (\text{C.3})$$

This direct discrete formulation has two main issues. First, it is clearly computationally expensive. Second, algebraic manipulation of the expression is required in order to avoid the singularities in the integrand whenever $r_j = y_j$.

One method used to mitigate the computational expense is to use the matrix form of Eq. (C.3). This expression can be converted directly into a matrix expression, offering a trade-off between computation speed and memory. This is realized by investing the time necessary to create the Abel matrix, l , and storing it in memory for later use. This is particularly useful for Abel matrices where $N \gg 10$. However, this does not address the issue of singular integrands. To resolve this issue, we must reformulate the discrete Abel transform rather than simply evaluate the continuous expression in a discrete manner.

To reformulate the discrete Abel Transform, first consider the physical interpretation in the expression of the continuous form in Eq. (C.1): we are “summing” the

contributions of $f(r)$ along a straight line with impact parameter y . If we divide the field into concentric circular regions, the center of each coinciding with a different chord's impact parameter, we can then sum the values of f corresponding to each region weighted by the length of the chord in the region. This is illustrated in Fig. C.2 and results in the following expression for the Abel matrix.

$$l_{ij} = \begin{cases} \sqrt{(r_i + \Delta r/2)^2 - r_i^2} & i = j \\ \sqrt{(r_j + \Delta r/2)^2 - r_i^2} - \sqrt{(r_j - \Delta r/2)^2 - r_i^2} & i < j \\ 0 & i > j \end{cases} \quad (\text{C.4})$$

This form of the Abel matrix is similar to that formulated by Bell [47] and identical to the ‘‘Onion Peeling’’ method described by Dasch [44]. Note that l_{ij} in Eq. (C.4) has upper triangle form, has an inverse, and hence avoids the singularity problem apparent in Eq. (C.3). The two expressions can be viewed loosely analogous to the Midpoint vs. Left Riemann integral approximation methods.

Dasch describes another method for obtaining Abel inverted data, which he calls a 3-Point Abel Deconvolution [44]. This method uses a second order polynomial fit for dF/dy , in Eq. (C.2), near the measurement impact parameters, y_i . The matrix expression for the 3-Point Abel Deconvolution method is given by

$$L_{ij} = \begin{cases} 0 & j < i - 1 \\ \mathbf{I}_{i,j+1}(0) - \mathbf{I}_{i,j+1}(1) & j = i - 1 \\ \mathbf{I}_{i,j+1}(0) - \mathbf{I}_{i,j+1}(1) + 2\mathbf{I}_{ij}(1) & j = i \\ \mathbf{I}_{i,j+1}(0) - \mathbf{I}_{i,j+1}(1) + 2\mathbf{I}_{ij}(1) - \mathbf{I}_{i,j-1}(0) - \mathbf{I}_{i,j-1}(1) & j \geq i + 1 \\ \mathbf{I}_{i,j+1}(0) - \mathbf{I}_{i,j+1}(1) + 2\mathbf{I}_{ij}(1) - 2\mathbf{I}_{i,j-1}(1) & i = 0, j = 1 \end{cases} \quad (\text{C.5})$$

where

$$\mathbf{I}_{ij}(0) = \begin{cases} 0 & j = i = 0 \text{ or } j < i \\ \frac{1}{2\pi} \ln \left\{ \frac{\sqrt{(2j+1)^2 - 4i^2} + 2j + 1}{2j} \right\} & j = i \neq 0 \\ \frac{1}{2\pi} \ln \left\{ \frac{\sqrt{(2j+1)^2 - 4i^2} + 2j + 1}{\sqrt{(2j-1)^2 - 4i^2} + 2j - 1} \right\} & j > i \end{cases} \quad (\text{C.6})$$

and

$$\mathbf{I}_{ij}(1) = \begin{cases} 0 & j < i \\ \frac{1}{2\pi} \sqrt{(2j+1)^2 - 4i^2} - 2j\mathbf{I}_{ij}(0) & j = i \\ \frac{1}{2\pi} \left\{ \sqrt{(2j+1)^2 - 4i^2} - \sqrt{(2j-1)^2 - 4i^2} \right\} - 2j\mathbf{I}_{ij}(0) & j > i \end{cases} \quad (\text{C.7})$$

This method provides a factor of two less noise in the inversion compared to the Onion Peeling method. However, this method relies on equally spaced projection measurements located at impact parameters which are integer multiples of the measurement spacing, i.e. $y_i = i\Delta r$. Because this restriction is sometimes impractical and the noise reduction is not significant to our application, we use the Onion Peeling method of Abel transform and inverse transform.

C.2 Inversion Validation & Error Estimates

As mentioned earlier, many methods have been employed to reduce errors directly associated with computing Abel transforms and their inverses [42–46]. While all methods differ in particulars, all essentially use data interpolation to reduce errors. The data interpolation paradigms use types of spline fits to measured data [42, 45], orthogonal function expansions of measured data [43, 46], or second order polynomial fits [44]. The Onion Peeling method applied to the data presented in this dissertation does not interpolate between data points and therefore offers no error reduction mechanism. As such, it is critical that we present some estimate on the error pro-

duced by the Abel inversion process and establish confidence in our application of the algorithm.

To begin an estimation on the error produced by an Abel inversion, we begin with a simulated emissivity projection, shown in Fig. C.3(a). This emissivity projection was created from a simulated emissivity profile shown in Fig. C.3(b). The emissivity profile is normalized and its shape, while somewhat arbitrary, was chosen to resemble the measured profiles of MCX discharges presented in Sec. 4.3. If we had an arbitrarily large number of chords, the blue curve in Fig. C.3(a) is what they would measure. However, we only have a limited number of chords, and the measurements seen by these are shown in Fig. C.3(a) as red triangles.

Now let us consider an Abel inversion, as discussed in the previous section. Applying an Onion Peeling method directly to the discrete chord data in Fig. C.3(a) results in the corresponding red triangles in Fig. C.3(b). The deviation of the “measured” values from the true values in Fig. C.3(b) gives an indication of the error introduced by the Abel inversion. This can be highly dependent on the type of profile being measured and the fortuitous positions of the view chords relative to features in the projected profile. In order to quantify the error involved, we investigate two types of error: error due to independent, random noise in the measurements of each chord; and error due to the systematic mis-measurement of a chord.

For a quantitative analysis we can compare statistical results with error estimates put forth by Dasch [44], namely

$$\delta f_i = \mathcal{N} \left(\sum_{j=1}^N L_{ij}^2 \right)^{1/2}, \quad (\text{C.8})$$

where \mathcal{N} is the amplitude of the noise in the measurement signal, and $L_{ij} = l_{ij}^{-1}$ is the inverse Abel matrix. This estimate is valid if the measurement error in each chord is independent. This excludes irregularities in the field being measured, and limits

us to instrumental noise. To compare effects of noise on our particular profile with Eq. (C.8), we did the following. First, we begin with the projection signals, Γ , and apply random Gaussian noise with amplitude $\mathcal{N} = 0.05$ to each projection signal, denoted Γ^* . We then deconvolve the noisy data directly with the matrix operation $\gamma^* = L\Gamma^*$. This is repeated 100 times and the standard deviation is calculated for each chord independently and is represented by the error-bars in Figs. C.3(a) & (b). Explicitly, $\delta\Gamma^* = \sqrt{\sum (\Gamma^* - \langle\Gamma^*\rangle)^2/N} \cong 0.05$ and $\delta\gamma^* = \sqrt{\sum (\gamma^* - \langle\gamma^*\rangle)^2/N}$. The magnitude of $\delta\gamma^*$ is plotted along with Eq. (C.8) in Fig. C.3(c). This shows that the expected error from Abel inversion due to random noise matches very well with that estimated by Dasch. Also shown in Fig. C.3(c) is the absolute deviation of the average deconvolved signal, $|\langle\gamma^*\rangle - \gamma|$, which indicates the contribution of systematic error due to the lack of chord resolution as well as the imperfectly centered noise distributions. As an additional test, the procedure was also performed with $\mathcal{N} = 0.0003$, which more appropriately resembles the instrumental noise of an HED. This variance is much smaller than the plotted symbol size, and therefore not included in Figs. C.3(a) & (b), but the error magnitude results are shown in Fig. C.3(d). This indicates that systematic error will dominate the interpretation of chord measurements in MCX discharges.

It is seen in Fig. C.3(d) that the systematic error is most significant ($\sim 10\%$) for the first chord and diminishes for further inward chords. This is due to the first chord's proximity to the large profile gradient at $r = 0.9$ and the lack of resolved measurements in this region. From Fig. C.3(c) we see that the random noise has the largest impact on systematic error for chords 1–12, while chords 13–16 remain virtually unaffected compared to Fig. C.3(d), even though the noise amplitude differs by 2 orders of magnitude. This is due to the imperfectly centered noise distributions.

To further investigate systematic errors due to mis-measurement of an HED, we again start with the same profiles as before. However, instead of applying random

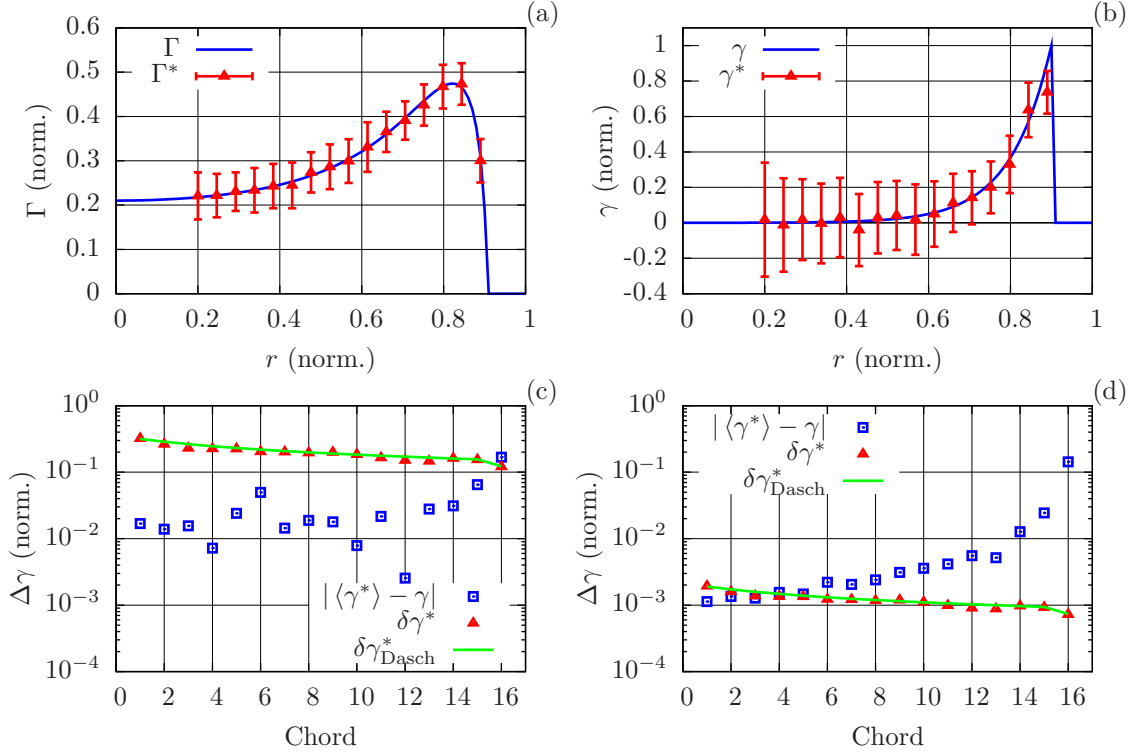


Figure C.3: Shown are the results of Abel inversion error due to random error in chord measurements. (a) A projection profile (blue) shown with 16 chord measurements (red triangles), each with $\mathcal{N} = 0.05$ random Gaussian error. (b) The actual profile (blue) shown with the inverted measurements and their resulting error (red triangles). (c) The absolute deviation of the average inverted signal (blue squares), amplitude of statistical error (red triangles), and the statistical error prescribed by Dasch, Eq. (C.8) [44]. (d) Similar to (c) except that $\mathcal{N} = 0.0003$ was used for the noise amplitude.

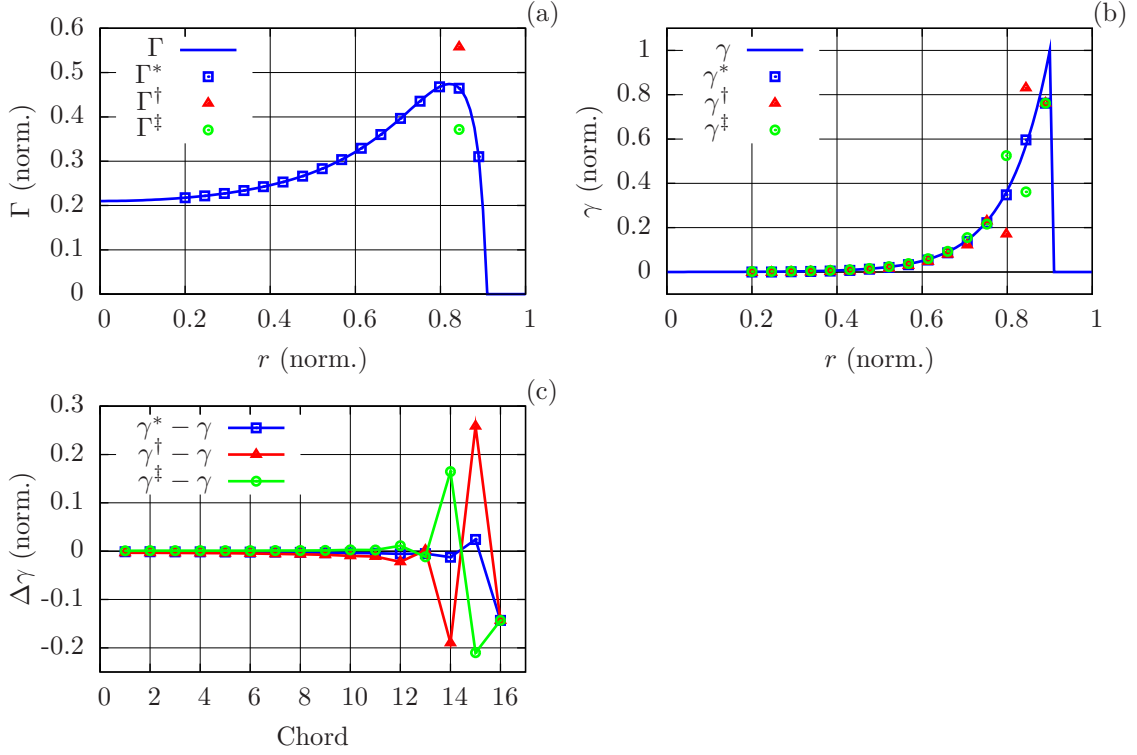


Figure C.4: Shown is a chord integrated profile (blue) with a single chord mis-measured (a), the resulting inverted profiles (b), and the difference between the inverted profiles and the actual profile (c). The red triangles correspond to profiles associated with the overestimated measurement and the green circles correspond to the underestimated measurement. The blue squares represent perfect measurements.

noise we simply modify one of the chord measurements and then observe how that “error” propagates to the remaining inverted measurements. Figure C.4 shows such an experiment. Here we have taken the projection profile (Γ) and 16 perfect projection measurements (Γ^*), and multiplied only chord 15 ($r \simeq 0.85$) by a factor of 1.2 (Γ^\dagger) and 0.8 (Γ^\ddagger). The three resulting inverted profiles are shown in Fig. C.4(b). The difference from the actual profile, γ , is shown in Fig. C.4(c).

We can see from these results that the effect of a systematic error of a single chord is to alter the neighboring inside shell in the opposite way, i.e. if a chord measurement is overestimated then the neighboring inside shell will be underestimated after inversion. We also see that the error does not propagate significantly beyond the nearest inside chord. This is because the onion peeling method determines the

local field value by subtracting off contributions from exterior shells. A systematic overestimate(underestimate) of one chord will then present too much(little) subtraction from the next inward chord measurement, resulting in a systematic underestimate(overestimate) of the emissivity of the next inward shell. However, since the next inward shell is affected in the opposite way, their combined effect is virtually cancelled and subsequent inward shells are largely insulated from the error. We can also see the systematic error due to insufficiently resolved measurements of the projected profile near $r = 0.9$.

Appendix D

Nominal MCX Parameters

For reference purposes we include a table of nominal MCX discharge parameters and a table of nominal time scales. These parameters are not intended to represent the best values achieved or to indicate the full range (or limitations) of these parameters. They are intended for “back-of-the-envelope” calculations, or to make approximate scaling arguments.

Table D.1: Nominal MCX Discharge Parameters

Parameter	Value	Parameter	Value
V_p	4 kV	B_0	2100 G
I_p	2 kA	\mathcal{R}	6
p_{fill}	5 mTorr	N_{fill}	$3.2 \times 10^{14} \text{ cm}^{-3}$
a	18.4 cm	L_{\parallel}	130 cm
n_0	$7 \times 10^{14} \text{ cm}^{-3}$	η_{\perp}	$1.5 \times 10^{-14} \text{ s}$
$\langle u_{\phi} \rangle$	100 km/s	c_s	50 km/s
M_s	2.7	M_A	0.6
T_e	3.3 eV	T_i	15 eV
$\ln \Lambda$	7.7	v_{Ai}	170 km/s
ω_e	$1.3 \times 10^{12} \text{ s}^{-1}$	ω_i	$29 \times 10^9 \text{ s}^{-1}$
Ω_e	$3.7 \times 10^{10} \text{ s}^{-1}$	Ω_i	$2.0 \times 10^7 \text{ s}^{-1}$
ρ_e	21 μm	ρ_i	1.9 mm
Γ_e	3.9×10^{-3}	Γ_i	8.5×10^{-4}
λ	1 μm		

Table D.2: Nominal MCX Discharge Time Scales

Time	Expression	Value (μs)
Radial Alfvén	$\frac{a}{v_A}$	1
Axial Alfvén	$\frac{L}{v_A}$	7.5
Rotation Period	$\frac{\pi(r_2+r_1)}{\langle u_{\phi} \rangle}$	9.7
Interchange Growth	$\frac{\sqrt{aL}}{v_T}$	13
Axial Sonic	$\frac{L}{c_s}$	27
Mirror Loss (electron)	$\frac{\sqrt{\pi RL}}{v_T} e^{e\Phi/T}$	49
Ambipolar Diffusion	$\frac{a^2 \tau_i}{8\rho_i^2}$	210
Resistive	$\frac{4\pi a^2}{c^2 \eta}$	300
Momentum Confinement		400
Mirror Loss (ion)	$\frac{\sqrt{\pi RL}}{v_T} e^{e\Phi/T}$	1000
Viscous Damping	$\tau_i \frac{a^2}{\rho_i^2}$	1700
Axial Ion Heat	$\tau_i \frac{L^2}{\lambda_i^2}$	1700
Bohm Diffusion	$\frac{4a^2 eB}{cT}$	1900
Axial Electron Heat	$\tau_e \frac{L^2}{\lambda_e^2}$	1900

Bibliography

- [1] R. F. Ellis, A. B. Hassam, S. Messer, and B. R. Osborn. An experiment to test centrifugal confinement for fusion. *Physics of Plasmas*, 8(5):2057–2065, 2001.
- [2] A. B. Hassam. Nonlinear stabilization of the rayleigh-taylor instability by external velocity shear. *Physics of Fluids B: Plasma Physics*, 4(3):485–487, 1992.
- [3] A. B. Hassam. Velocity shear stabilization of interchange modes in elongated plasma configurations. *Physics of Plasmas*, 6(10):3772–3777, 1999.
- [4] Yi-Min Huang and A. B. Hassam. Velocity shear stabilization of centrifugally confined plasma. *Physical Review Letters*, 87(23):235002, December 2001.
- [5] Peter C. Stangeby. *The Plasma Boundary of Magnetic Fusion Devices*. Institute of Physics Publishing, Bristol, UK, 2000.
- [6] R. L. Boivin, J. A. Goetz, A. E. Hubbard, J. W. Hughes, I. H. Hutchinson, J. H. Irby, B. LaBombard, E. S. Marmor, D. Mossessian, C. S. Pitcher, J. L. Terry, B. A. Carreras, and L. W. Owen. Effects of neutral particles on edge dynamics in alcator c-mod plasmas. *Physics of Plasmas*, 7(5):1919–1926, 2000.
- [7] Sarah Messer. *Supersonic Rotation in the Maryland Centrifugal Experiment*. PhD thesis, University of Maryland-College Park, 2003.
- [8] S. Messer, R. Ellis, A. Case, D. Gupta, A. Hassam, R. Lunsford, and C. Teodorescu. Observation of momentum confinement time scalings in a rotating plasma. *Physics of Plasmas*, 12(6):062509, 2005.
- [9] J. Ghosh, R. C. Elton, H. R. Griem, A. Case, R. Ellis, A. B. Hassam, S. Messer, and C. Teodorescu. Spectroscopic measurements of plasma rotation and ion and neutral atom temperatures in the maryland centrifugal experiment. *Physics of Plasmas*, 11(8):3813–3818, 2004.
- [10] J. Ghosh, R. Elton, H. Griem, C. Teodorescu, A. Case, and R. Ellis. Vacuum ultraviolet measurements on hydrogen resonance lines in the maryland centrifugal experiment. *Physics of Plasmas*, 12(3):034501, 2005.
- [11] J. Ghosh, R. C. Elton, H. R. Griem, A. Case, A. W. DeSilva, R. F. Ellis, A. Hassam, R. Lunsford, and C. Teodorescu. Radially resolved measurements of plasma rotation and flow-velocity shear in the maryland centrifugal experiment. *Physics of Plasmas*, 13(2):022503, 2006.
- [12] B. Lehnert. Screening of a high-density plasma from neutral gas penetration. *Nuclear Fusion*, 8:173–181, 1968.
- [13] B. Lehnert, J. Bergström, S. Holmberg, and B. Wilner. On the interaction between a fully ionized plasma and a neutral gas blanket. *Physica Scripta*, 1(1):39–45, 1970.

- [14] B. Lehnert. Stability of plasmas penetrated by neutral gas. *Nuclear Fusion*, 13:781–790, 1973.
- [15] R.J. Colchin, N.H. Brooks, L.W. Owen, R. Maingi, R.C. Isler, T.N. Carlstrom, and R.J. Groebner. Measurement of neutral densities at the outer midplane in diiii-d. volume 24B, pages 760–763. EPS, June 2000.
- [16] R.J. Colchin, R. Maingi, M.E. Fenstermacher, T.N. Carlstrom, R.C. Isler, L.W. Owen, and R.J. Groebner. Measurement of neutral density near the x point in the diiii-d tokamak. *Nuclear Fusion*, 40(2):175–180, 2000.
- [17] R. L. Boivin, J. W. Hughes, B. LaBombard, D. Mossessian, and J. L. Terry. High resolution measurements of neutral density and ionization rate in the alcator c-mod tokamak. *Review of Scientific Instruments*, 72(1):961–964, January 2001.
- [18] N. E. Lanier, D. Craig, J. K. Anderson, T. M. Biewer, B. E. Chapman, D. J. Den Hartog, C. B. Forest, , and S. C. Prager. Measurement of electron transport in the madison symmetric torus reversed-field pinch (invited). *Review of Scientific Instruments*, 72(1):1039–1045, January 2001.
- [19] H. S. McLean, A. Ahmed, D. Buchenauer, D. Den Hartog, C. W. Domier, D. N. Hill, C. Holcomb, E. B. Hooper, E. C. Morse, M. Nagata, Y. Roh, B. Stallard, R. D. Wood, S. Woodruff, G. Wurden, Z. Wang, and SSPX Team. Plasma diagnostics for the sustained spheromak physics experiment. *Review of Scientific Instruments*, 72(1):556–561, 2001.
- [20] Zhehui Wang, G. A. Wurden, Cris W. Barnes, C. J. Buchenauer, H. S. McLean, D. N. Hill, E. B. Hooper, R. D. Wood, and S. Woodruff. Density and h_α diagnostics and results for the sustained spheromak physics experiment. *Review of Scientific Instruments*, 72(1):1059–1062, January 2001.
- [21] R. J. Colchin, D. L. Hillis, R. Maingi, C. C. Klepper, and N. H. Brooks. The filterscope. *Review of Scientific Instruments*, 74(3):2068–2070, March 2003.
- [22] S. P. Gerhardt, J. M. Canik, D. T. Anderson, and L. Owen. H_α detector system for the helically symmetric experiment. *Review of Scientific Instruments*, 75(9):2981–2984, September 2004.
- [23] N. Brenning. Review of the civ phenomenon. *Space Science Reviews*, 59:209–314, February 1992.
- [24] Robert Lunsford. *Parametric Limitations on Discharge Performance in the Maryland Centrifugal eXperiment*. PhD thesis, University of Maryland-College Park, College Park, 2006.
- [25] C. Teodorescu, R. Clary, R. F. Ellis, A. B. Hassam, R. Lunsford, I. Uzun-Kaymak, and W. C. Young. Experimental study on the velocity limits of magnetized rotating plasmas. *Physics of Plasmas*, 15(4):042504, 2008.

- [26] I. H. Hutchinson. *Principles of Plasma Diagnostics*. Cambridge University Press, Cambridge, 1987.
- [27] L. C. Johnson and E. Hinnov. Ionization, recombination, and population of excited levels in hydrogen plasmas. *Journal of Quantitative Spectroscopy and Radiative Transfer*, 13:333–358, 1973.
- [28] H. R. Griem. *Plasma Spectroscopy*. McGraw Hill Book Company, 1964.
- [29] R. Janev. Atomic and molecular physics issues in current thermonuclear fusion research. *Contemporary Physics*, 46:121–140, March 2005.
- [30] C. Bowen, A. Decoster, C.J. Fontes, K.B. Fournier, O. Peyrusse, and Yu.V. Ralchenko. Review of the nlte emissivities code comparison virtual workshop. *Journal of Quantitative Spectroscopy and Radiative Transfer*, 81:71–84, 2003.
- [31] R. J. Goldston and P. H. Rutherford. *Introduction to Plasma Physics*. Institute of Physics Publishing, Briston, UK, 1995.
- [32] Sheung-Wah Ng. *Plasma-Neutral Equilibrium in Centrifugally Confined Plasma*. PhD thesis, University of Maryland-College Park, College Park, 2007.
- [33] C. F. F. Karney, D. P. Stotler, C. H. Skinner, J. L. Terry, and D. A. Pappas. Effect of reflection on h_α emissions in alcator c-mod. *Review of Scientific Instruments*, 70(1):344–346, 1999.
- [34] J. D. Jackson. *Classical Electrodynamics*. John Wiley & Sons, Inc., New York, third edition, 1999.
- [35] Eugene Hecht. *Optics*. Addison Wesley, 4th edition, 2002.
- [36] Grant R. Fowles. *Introduction to Modern Optics*. Courier Dover Publications, 2nd edition, 1989.
- [37] C. Teodorescu, R. F. Ellis, A. Case, C. Cothran, A. Hassam, R. Lunsford, and S. Messer. Experimental verification of the dielectric constant of a magnetized rotating plasma. *Physics of Plasmas*, 12(6):062106, 2005.
- [38] S. W. Simpson. A steady-state fluid model of a rotating plasma. *Physics of Fluids*, 24(3):418–429, 1981.
- [39] Yi-Min Huang. *Magnetohydrodynamic Equilibrium and Stability of Centrifugally Confined Plasma*. PhD thesis, University of Maryland-College Park, 2004.
- [40] Daren Stotler, Charles Karney, Randall Kanzleiter, and S. Jaishankar. *User’s Guide for DEGAS 2*. Princeton Plasma Physics Laboratory, cvs revision: 1.4 edition, June 2007.
- [41] Alan DeSilva. *Plasma Diagnostics*. University of Maryland-College Park, College Park, 1996.

- [42] J. Glasser, J. Chapelle, and J. C. Boettner. Abel inversion applied to plasma spectroscopy - a new interactive method. *Applied Optics*, 17:3750–3754, December 1978.
- [43] M. Kalal and K. A. Nugent. Abel inversion using fast fourier transforms. *Applied Optics*, 27:1956–1959, May 1988.
- [44] C. J. Dasch. One-dimensional tomography - a comparison of abel, onion-peeling, and filtered backprojection methods. *Applied Optics*, 31:1146–1152, March 1992.
- [45] Shay Gueron and Moshe Deutsch. A fast abel inversion algorithm. *Journal of Applied Physics*, 75(9):4313–4318, 1994.
- [46] P. Tomassini and A. Giulietti. A generalization of abel inversion to non-axisymmetric density distribution. *Optics Communications*, 199:143–148, November 2001.
- [47] Ronald E. Bell. Inversion technique to obtain an emissivity profile from tangential line-integrated hard x-ray measurements. *Review of Scientific Instruments*, 66(1):558–560, January 1995.